Annual Report 2000

AG Magnetismus
Universität Kaiserslautern

Address: Prof. Dr. Burkard Hillebrands
Fachbereich Physik
Universität Kaiserslautern
Erwin-Schrödinger-Straße 56
67663 Kaiserslautern, Germany
Tel.: +49 (0) 631 – 205–4228
Fax: +49 (0) 631 – 205–4095

Postal address: Postfach 3049
67653 Kaiserslautern, Germany

Internet: http://www.physik.uni-kl.de/w_hilleb/w_hilleb.html
E-Mail: hilleb@physik.uni-kl.de

AG Magnetismus
Universität Kaiserslautern

Our Group

From left to right:

Marc Rickart, Prof. Dr. Burkard Hillebrands, Dr. Kurt Jung, Dr. Sergey Demokritov, Heike Schuster, Martin Lesmeister, Stefan Poppe, Tim Mewes, Jörg Jorzick, Mathias Mautner, Sybille Müller, Andreas Beck, Bernd Pfaff, Björn Roos, Hans Nembach, Radek Lopusnik, Dr. Jürgen Fassbender.

Contents

Chapter 1: Introduction

Dear colleagues and friends,

by now it has become a tradition to report our work in the Annual Report. This fourth issue covers the period November 1999 to October 2000.

Much of our research is in the field of magneto-electronics, where we address problems of fast magnetic switching, the exchange bias effect and tunneling magnetoresistance. These studies are supported by programs in materials fabrication and advanced characterization tools. The details and results are summarized in the following Chapters.

Highlights of our work in the last year are: i) the manipulation of the exchange bias field by ion irradiation, both in strength and direction, ii) the time resolved analysis of the magnetization dynamics, pushing the experimental technique forward to a time resolution of 17 ps by electronic delay, iii) improved understanding of the dynamic eigen-excitations in magnetic dots and the discovery of magnetic edge modes, and iv) the fabrication of magnetic tunnel junctions by an oxygen embedding process and an improved understanding of the oxidation mechanism.

Our second area of interest, the field of hard and wear resistant films and coatings, is the subject of our Institut für Dünnschichttechnologie – Transferstelle der Universität Kaiserslautern (Institute for Thin Film Technology – Center for Technology Transfer of the University of Kaiserslautern) located in Rheinbreitbach at the northern boarder or Rheinland-Pfalz. We have extended our interest to applications of carbon films for medical applications.

As the biggest academic event in our group, Sergey Demokritov successfully completed his habilitation in early summer.

In the last year we had two long-term guests in our group. Prof. Dr. Carl E. Patton from Colorado State University has spend a sabbatical year funded by the Alexander von Humboldt foundation. Dr. Alexandra Mougin from the University of Nancy, France worked in our group with funding by the European Community. She worked mostly in the area of exchange bias systems. She left end of September taking the position of a permanent research staff member at the CNRS in Orsay.

Several members left our group. Dr. Claudius Osthöver, who worked in the Institut für Dünnschichttechnologie in Rheinbreitbach, has left for a better paid job in industry. Oliver Büttner, who has pushed forward the time resolved Brillouin light scattering experiments on spin wave packets like solitons and bullets, has completed his dissertation.

Several new members arrived. Hans Nembach and Lisa Kleinen started their Ph.D. projects. Heike Schuster started work as a secretary of the Schwerpunkt Materialwissenschaften and works jointly for all groups of the Schwerpunkt located in Building 56.

It is a pleasure to greet all other former members of our group via this report. May this annual report help us to stay in touch with each other.

Four awards have been obtained by members of the group, among them the Sonderpreis der Ernst-Kalkhoff-Stiftung in the competition "Pioniergeist 2000" of the government of the State of Rheinland-Pfalz for Heinz Busch and Udo Grabowy for their concept of their start up company to develop and produce high-tech films for medical applications.

Our work within magneto-electronics and related areas is part of four international and national networks: the TMR-Dynaspin network funded by the European Union, the network "Nanomagnetism and growth processes on vicinal surfaces" funded by the European Science Foundation, the "Leitprojekt Magnetoelektronik" funded by the Bundesministerium für Bildung und Forschung (BMBF) and industry, and the Center of Competence "Nanoclub Lateral", also funded by the BMBF and industry.

Our work would not have been possible without valuable collaborations with people all over the world. We would like to thank, in alphabetical order, Bernard Bartenlian, Harry Bernas, Klaus Bewilogua, John Chapman, Claude Chappert, John Cochran, Horst Dötsch, Ursula Ebels, Giancarlo Faini, Claude Fermon, Jacques Ferré, Zdenek Frait, Uwe Hartmann, Boris Kalinikos, Kathleen Kirk, Mikhail Kostylev, Achim Lunk, Wolfram Maaß, Roland Mattheis, Ulrich Memmert, Jacques Miltat, Fabrizio Nizzoli, Kamel Ounadjela, Carl Patton, Yuri Rapoport, Theo Rasing, Frank Richter, Francoise Rousseaux, John R. Sandercock, Andrei Slavin, Elin Søndergard, Bob Stamps, Evgueni Tsymbal, Stefan Visnovsky and Joachim Wecker for their interactions with us and their strong input on our work. Collaborations within the Fachbereich Physik at the University of Kaiserslautern (Martin Aeschlimann (who has just arrived), Hans Schmoranzer, Herbert Urbassek, Richard Wallenstein and Christiane Ziegler and their groups) and the Institut für Oberflächen- und Schichtanalytik (Hans Oechsner and his group) have been very stimulating. I would also like to thank all sponsors, which are the Deutsche Forschungsgemeinschaft, the Bundesministerium für Bildung, Wissenschaft, Forschung und Technologie, the Siemens AG, the Humboldt Foundation, the European Community, the European Science Foundation, INTAS, the State of Rheinland-Pfalz and the University of Kaiserslautern. My special thanks go to Tim Mewes, Sibylle Müller and Heike Schuster for their technical help in preparing this report.

If you are interested in our work we would be happy to hear from you. If you have any questions, comments, suggestions, or any kind of criticism, please contact us.

With all my best wishes for Christmas, and a Happy New Year,

Burkard Hillebrands

Kaiserslautern, November 2000

Chapter 2: Personnel

2.1 Members of the Group

Group leader:

Prof. Dr. Burkard Hillebrands

Senior Scientists:

Dr. Heinz Busch, Wiss. Assistent (Rheinbreitbach)	
Dr. Sergey Demokritov, Wiss. Assistent (C1)	
Dr. Jürgen Fassbender, Wiss. Assistent (C1)	
Dr. Udo Grabowy, Wiss. Assistent (Rheinbreitbach)	
Dr. Kurt Jung, Akad. Direktor	
Dr. Claudius Osthöver (Rheinbreitbach)	until 09/00

Post Docs:

Dr. Alexandra Mougin	until 09/00

PhD students:

Dipl.-Phys. Martin Bauer	
Dipl.-Phys. Oliver Büttner	until 01/00
Dipl.-Phys. André Frank	
Dipl.-Phys. Jörg Jorzick	
Dipl.-Phys. Lisa Kleinen	since 10/00
Dipl.-Phys. Radek Lopusnik	
Dipl.-Phys. Tim Mewes	
Dipl.-Phys. Hans Nembach	since 04/00
Dipl.-Phys. Stefan Poppe	
Dipl.-Phys. Marc Rickart	
Dipl.-Phys. Björn Roos	
Dipl.-Phys. Thomas Wittkowski	

Diploma Students:

Andreas Beck	since 03/00
Christian Krämer	
Andreas Rueff	until 03/00

Engineers and Technicians:

Mathias Mautner	since 11/99
Bernd Pfaff	
Sven Schlierkamp (Rheinbreitbach)	

Secretary:

Sibylle Müller
Heike Schuster (Schwerpunkt Materialwissenschaften) since 07/00

2.2 Visiting Scientists and Postdoctoral Fellows

Dr. Alexandra Mougin, Laboratoire de Physique des Materiaux, Université Henri Poincaré, Nancy, France 01.08.99 – 30.09.00

Alexandra spent 14 months in our lab supported by the EU-TMR programme "DYNASPIN". She worked mostly on the exchange bias effect modified by ion irradiation.

Prof. Dr. Carl E. Patton, Colorado State University, Fort Collins, U.S.A. 16.08.99 – 13.07.00

Carl spent his sabbatical in our lab supported by the Alexander von Humboldt foundation. He worked mostly on time resolved Brillouin light scattering experiments and on the analysis of the mode spectrum measured by time resolved magneto-optic Kerr magnetometry.

Dr. Alexander Serga, Radiophysical Faculty, Taras Shevchenko Kiev University, Kiev, Ukraine 01.07.00 – 31.08.00

Alexander spent a short research stay in our lab supported by the Graduiertenkolleg "Laser- und Teilchenspektroskopie". He worked on time resolved Brillouin light scattering, in particular on the preparation of experiments for parametric pumping of wave packets.

Prof. Dr. Andrei Slavin, University of Rochester, Michigan, U.S.A. 15.05.00 – 18.06.00

Andrei spent a short research stay in our lab supported by funds of the Laserzentrum. He was heavily involved in the modeling of nonlinear spin wave propagation and in the modeling of laterally quantized spin wave modes in confined magnetic objects.

2.3 Guest Seminars

Prof. Dr. C.E. Patton 15.08.99 – 15.07.00	Colorado State University, Fort Collins, USA *Nonlinear magnetic excitations* Group seminar, 15.11.1999
	Relaxation and damping phenomena Group seminar, 29.11.1999
	Linear and nonlinear spin wave excitations Seminar des Zentrums für Lasermesstechnik und Diagnostik, gemeinsam mit dem Graduiertenkolleg Laser- und Teilchenspektroskopie, 14.01.2000
Prof. Dr. B. Kalinikos 30.11.99 – 01.12.99	Electrotechnical University, St. Petersburg, Russia *Nonlinear spin waves* Group seminar, 1.12.2000
Dr. D. Berkov 22.-23.02.00	Innovent e.V., Jena *Mikromagnetische Simulationen für MRAM-Speicherzellen* Sonderseminar, 23.02.00
Dr. A. Brodyanski 28.02.00	z.Zt. Universität Kaiserslautern *Magnetismus am festen Sauerstoff* Group seminar,

"Kaiserslautern meets Orsay" – bilateral workshop in Kaiserslautern
29.02.–01.03.00

J. Miltat, A. Thiaville (O)	*Micromagnetic investigations of the magnetic switching process*
D. Ravelosona (O)	*Geometrically induced domain wall pinning in mesoscopic wires*
C. Chappert (O)	*Sub-50 nm planar magnetic nanostructures fabricated by ion irradiation*
T. Devolder (O)	*Effect of ion beam irradiation on the magnetic properties of Co/Pt films*
J. Jorzick (KL)	*Spin waves in wires, dots and squares*
A. Mougin (KL)	*Tayloring exchange bias using ion irradiation*
M. Bauer (KL)	*Time resolved Kerr magnetometry*

Dipl.-Phys. Hans Nembach 02.03.00	Universität Stuttgart *Untersuchungen an der magnetischen Formgedächtnislegierung FeNiCoTi* Sonderseminar

Prof. Dr. R.L. Stamps 20.04.00	University of Western Australia *Dynamics of magnetization processes* Sonderseminar
Prof. Dr. B. Heinrich 08.05.00	Simon Frazer University, Burnaby, Canada *The role of interfaces in magnetic and electron transport properties in GaAs/Fe/Cu/Fe(001) and Fe whisker/MgO/Fe(001) systems* Kolloquium des Fachbereichs Physik
Prof. Dr. G. Bayreuther 18.05.00	Universität Regensburg *Schichtsysteme für die Magnetoelektronik* Materialwissenschaftliches Kolloquium
Prof. Dr. M. Farle 25.05.00	Technische Universität Braunschweig *Ferromagnetische Resonanz an ultradünnen Filmen* Materialwissenschaftliches Kolloquium
N. Nielsen 26.05.00	MPI Stuttgart *Coherent resonant pulse propagation in organic and anorganic semiconductors at high intensities* Sonderseminar
Prof. Dr. A.N. Slavin 28.05.00 - 18.06.00	University of Rochester, USA *Spin wave spectra of non-ellipsoidal magnetic dots* Sonderseminar, 02.06.2000
Prof. Dr. S. Visnovsky 07.–10.06.00	Charles University Prague *Magnetooptics in multilayered systems* Materialwissenschaftliches Kolloquium, 08.06.2000
Dr. E. Schloemann 21.06.00	Raytheon Coorperation, USA *Low-frequency radiation loss in ferrite microwave devices: application to filters, circulators and isolators* Sonderseminar
Dipl.-Phys. Wayne Hiebert 10.07.00	University of Alberta, Canada *Magnetization dynamics – time resolved Kerr microscopy* Sonderseminar
Dr. Russel Cowburn 13.07.00	Cambridge University, United Kingdom *Configurational anisotropy in patterned films* Materialwissenschaftliches Kolloquium
Dr. Jean Juraszek 07.09.00	Université de Rouen, Frankreich *Fast heavy ion irradiation effects in magnetic Tb/Fe multilayers* Sonderseminar

2.4 Group Member Photo Gallery

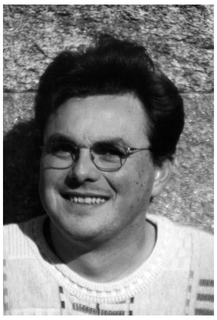
Martin Bauer
Ph.D. student


Andreas Beck
Diploma student

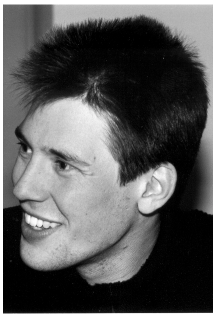
Oliver Büttner
Ph.D. student


Dr. Heinz Busch (Rbb)
Senior scientist


Dr. Sergey Demokritov
Senior scientist


Dr. Jürgen Fassbender
Senior scientist


André Frank
Ph.D. student


Dr. Udo Grabowy (Rbb)
Senior scientist


Prof. Dr. Burkard Hillebrands
Group leader


Jörg Jorzick
Ph.D. student


Dr. Kurt Jung
Senior scientist


Lisa Kleinen (Rbb)
Ph.D. student

Rbb: working at the Institut für Dünnschichttechnologie – Transferstelle der Universität Kaiserslautern – Rheinbreitbach, Germany

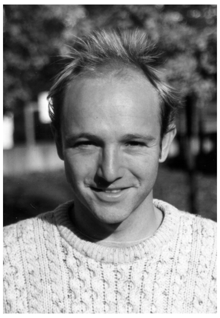
Christian Krämer
Diploma student


Radek Lopusnik
Ph.D. student


Mathias Mautner
Mechanical engineer


Tim Mewes
Ph.D. student


Dr. Alexandra Mougin
Postdoctorial fellow

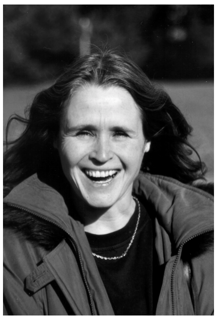
Sibylle Müller
Secretary


Hans Nembach
Ph.D. student

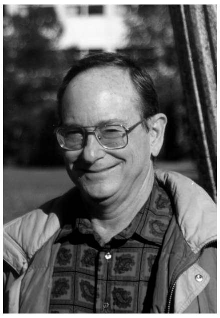
Prof. Dr. Carl Patton
Guest scientist


Bernd Pfaff
Technician


Stefan Poppe
Ph.D. student

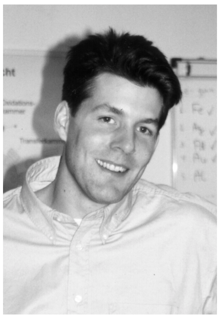
Marc Rickart
Ph.D. student


Björn Roos
Ph.D. student

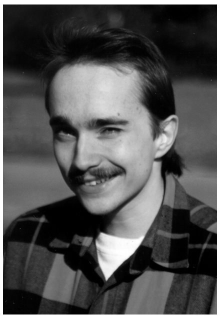

Andreas Rueff
Diploma student

Sven Schlierkamp (Rbb)
Technician

Heike Schuster
Secretary

Thomas Wittkowski
Ph.D. student

Chapter 3: Research Topics

We study mostly magnetic phenomena in ultrathin films and multilayers. Many activities belong to the field of magneto-electronics, a rapidly developing area bridging the gap between conventional magnetism and semiconductor physics in view of potential applications as sensor devices and magnetic random access memories. One key issue is the fabrication of high-quality epitaxial film and multilayer systems and devices using molecular beam epitaxy.

Our scientific work addresses largely problems in basic research, which emerge from applications of magnetic structures in data storage and sensor devices. We investigate both material sciences aspects of magnetic films, multilayers and patterned structures, and high frequency magnetic properties like linear and nonlinear spin waves, time dependent magnetization effects, and the time structure of the magnetic switching process.

In detail, our research subjects are:

1) Epitaxial magnetic films and multilayers: growth and structure

To study magnetic phenomena with the necessary precision, the preparation of samples with highest possible structural quality is very important. We achieve this by using molecular beam epitaxy (MBE), in which the standard *in situ* methods for chemical and structure analysis are employed. They comprise Auger spectroscopy for chemical analysis, low and high energy electron diffraction (LEED, RHEED), and a combined *in situ* scanning tunneling and atomic force microscope (STM/AFM).

2) Epitaxial magnetic films and multilayers: magnetic properties

Of interest to us is the determination and the origin of all contributing magnetic anisotropies, of coupling phenomena between magnetic films, and of the influence of atomic defects, steps, roughness and interdiffusion on the magnetic properties. We perform *in situ* Brillouin light scattering spectroscopy (BLS) and magneto-optic Kerr-magnetometry in the MBE system. *Ex situ,* the samples are investigated using Brillouin light scattering, vector Kerr magnetometry and vibrating sample magnetometry (VSM).

3) Exchange bias systems

An important issue is to clarify the origin of the exchange bias mechanism, a shift of the hysteresis loop along the field axis in bilayers of ferromagnetic and antiferromagnetic films by using *in situ* and *ex situ* Brillouin light scattering spectroscopy and magneto-optic Kerr magnetometry.

Emphasis is placed on effects of the modification of the exchange bias field and the coercive field by ion irradiation.

4) Tunneling magnetoresistance

We investigate transport phenomena based on the magnetic tunneling effect with the aim to develop new magnetic sensors. In a dedicated project we put special emphasis on the development of new methods to improve the structural quality of the insulating tunneling layers. We also conduct a program to search for new tunneling barrier materials.

5) Modification of magnetic properties by patterning

Patterning of magnetic films allows one to generate materials with new magnetic properties, like magnetic dot or wire arrays. Such structures probably will play a dominant role in future data storage and sensor applications. We focus on the investigation of the basic magnetic properties of such structures, in particular the domain structure and the change in the spin wave mode spectrum due to lateral confinement effects.

6) Fast magnetic switching

For memory devices it is of special importance how fast and secure magnetic domains can be written or the magnetization of a single magnetic object can be reversed. These switching phenomena take place on the nanosecond time scale. A time-resolved magneto-optic Kerr effect experiment and a Brillouin light scattering experiment are used to address the time-evolution of the magnetization reversal upon the application of short magnetic field pulses.

7) Nonlinear properties of microwave excited spin waves

Using Brillouin light scattering we measure the intensity distribution of spin waves propagating in a magnetic film with spatial and temporal resolution. The spin waves are excited by microwaves using a strip antenna. Central problems are the propagation of spin waves in the linear and nonlinear intensity regimes, the formation of instabilities (e.g. self-focusing), the propagation of nonlinear excitations (solitons, magnetic "bullets") and collision experiments of these excitations, as well as three wave processes.

8) Elastic properties of hard, super-hard and inhomogeneous films and multilayers

We prepare hard and super-hard films and investigate their elastic properties using Brillouin light scattering. Research subjects are amorphous carbon (a-C:H and ta-C:H) and boron nitride films, which are prepared using unbalanced magnetron sputtering. The elastic constants are determined from the dispersion curves of surface and film phonons (Rayleigh and Sezawa modes). Our aim is to prepare hard and super-hard films with minimized internal stresses.

Chapter 4: Equipment

A) Preparation and characterization of thin films and multilayers

1. multi-chamber molecular beam epitaxy system (Pink GmbH) comprising
   a. deposition chamber
   (electron beam and Knudsen sources, RHEED, LEED, Auger)
   b. scanning tunneling and atomic force microscopy chamber
   (*in situ* STM/AFM, Park Scientific)
   c. Brillouin light scattering and Kerr magnetometry chamber
   (magnetic field 1.2 T, temperature range 80 – 400 K)
   d. load lock chamber
   e. preparation chamber
   (optical coating, heating station 2300° C)
   f. transfer chamber
   g. atom beam oxidization chamber with *in situ* four-probe resistively measurement stage
2. two-chamber UHV deposition system
3. two-magnetron sputtering system
4. scanning tunneling and atomic force microscope (TopoMetrix)

B) Patterning of magnetic films

1. UV laser interference lithography setup
2. clean room facility with flow box, spin coater, etc.
3. reactive ion beam etching facility with *in situ* metal coater

C) Magnetic characterization

1. vibrating sample magnetometer
   (magnetic field 1.6 T, room temperature)
2. vibrating sample magnetometer
   (magnetic field 5 T, temperature range 2 – 350 K)
3. vector Kerr magnetometer
   (longitudinal and transverse Kerr effect, magnetic field 1.2 T, temperature range 2 – 350 K, automated sample positioning)
4. high-field polar Kerr magnetometer
   (magnetic field 5 T, temperature range 2 – 350 K)
5. Kerr magnetometer with time resolution and setup for generation of short field pulses
6. two Brillouin light scattering spectrometers, computer controlled and fully automated (magnetic field 2.2 T) with stages for
   a. low temperature measurements (2 – 350 K)
   b. space-time resolved measurements for spin wave intensity mapping (resolution 50 µm, 0.83 ns)
   c. UHV *in situ* measurements
   d. elastic measurements
7. microwave setup (up to 32 GHz) comprising a network analyzer, microwave amplifiers, modulators, pulse generators, etc.
8. two magneto-transport setups (magnetic field 1.5 T, temperature range 20 – 400 K)

Chapter 5: Transfer of Technology

1. Magnetic films and multilayers

With our facilities within the Department of Physics at the University of Kaiserslautern we offer consultance and transfer of technology in the areas of thin film magnetism, magnetic film structures and devices, magnetic sensors, and in corresponding problems of metrology.

We are equipped to perform magnetic, transport, elastic and structural measurements of films and multilayer systems.

This is in detail:

- magnetometry (magnetic field up to 5 T, temperature range 2 – 400 K) using vibrating sample magnetometry, Kerr magnetometry, Brillouin light scattering spectroscopy
- magnetic anisotropies (out-of-plane and in-plane), optionally with high spatial resolution
- magneto-transport properties
- test of homogeneity of magnetic parameters
- exchange stiffness constants in magnetic films
- elastic constants
- surface topography

2. Institut für Dünnschichttechnologie – Transferstelle der Universität Kaiserslautern

(Institute for Thin Film Technology – Center For Technology Transfer of the University of Kaiserslautern)

Aim of the Center is to assist companies in applications of thin film coatings to increase surface hardness, wear resistivity and bio-compatibility with the aim to reduce production costs and to increase product quality. Special emphasis is placed on coatings for medical applications.

The Center is part of the University of Kaiserslautern. It is located at the TZO (Technologiezentrum für Oberflächentechnik GmbH) in Rheinbreitbach, Germany.

The following services are offered:

- Consultance in tribological problems
- Analysis of wear problems
- Development of product specific coatings
- Optimization of coatings
- Coating of samples and small scale production series
- Consultance for implementation of coating procedures into the production process
- Courses and seminars concerning coating problems

Address:

Institut für Dünnschichttechnologie – Transferstelle der Universität Kaiserslautern
Maarweg 30
53619 Rheinbreitbach, Germany

Scientific director:

Prof. Dr. B. Hillebrands	phone: +49 631 205 4228 e-mail: hilleb@physik.uni-kl.de

Contact:

Dr. K. Jung	phone: +49 631 205 2278 e-mail: jung@physik.uni-kl.de

Representatives in Rheinbreitbach:

Lisa Kleinen	phone: +49 2224 900 693 e-mail: idst_ost@t-online.de
Dr. S. Sattel (TZO)	phone: +49 2224 942 113 e-mail: rtzo@rz-online.de

Please contact us for more informations.

Chapter 6: Experimental Results

A. Magnetic Tunnel Junctions

6.1 Direct investigation of the barrier oxidation process in magnetic tunnel junctions using atomic beam oxidation

B.F.P. Roos, P.A. Beck, S.O. Demokritov, and B. Hillebrands

The crucial step in the fabrication of magnetic tunnel junctions (MTJs) is the preparation of a homogeneous and pinhole free insulating barrier. The most widely used barrier material is Al_2O_3, and it is usually obtained by the deposition of a thin metallic Al layer onto a magnetic electrode followed by an oxidation process. Although the first room temperature MTJs were prepared using natural oxidation of Al in air [1], it was found that plasma oxidation seems to be the most reliable technique for producing MTJs with high tunneling magnetoresistance (TMR) [2]. However, contrary to thermal oxidation, which is elaborately studied, the process of Al oxidation using a plasma is not deeply understood yet. It is connected with the fact, that the ion energy distribution, dissociation rate, as well as the ion current density in the plasma near the oxidized surface is difficult to control. A novel type, ion beam oxidation method taking advantage of a low energy ion beam source (CCR Technology) allows us to control the ion current density (0.02–2 mA/cm^2) , ion energy (30–80 eV) and dissociation degree (up to 80%) of the beam independently. The kinetic energy of the ions is reduced to a level at which no sputtering and barrier defect formation occurs, making low energy ion beam oxidation a good candidate for producing high quality tunneling barriers.

The chosen magnetic electrode materials, NiFe and Co, do not provide the highest TMR values, as, for example, do the materials Co and CoFe. However, due to the large difference in their coercive fields, they allow us to realize the antiparallel orientation of the magnetizations without any additional layers, such as exchange biased layers or artificial antiferromagnets. The TMR value is 12% at room temperature. Figure 1 shows a TEM image of a three layer MTJ prepared with an ion dose of $3\cdot10^{16}$ ions/cm^2 and an ion energy of 30 eV. A clear separation between the electrodes and the barrier layer is observed without any indication of over-oxidation. The meas-

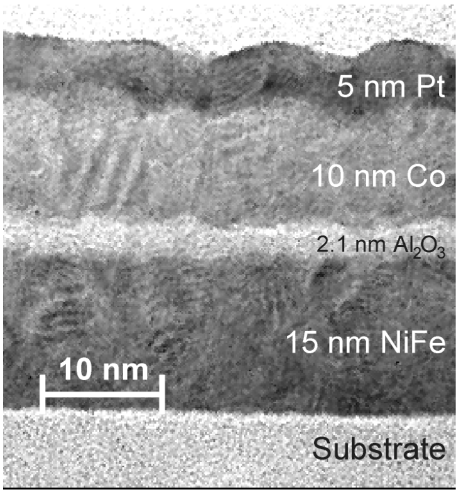

Fig. 1: TEM image of a three layer MTJ (image courtesy of Dogan Ozkaya, University of Oxford).

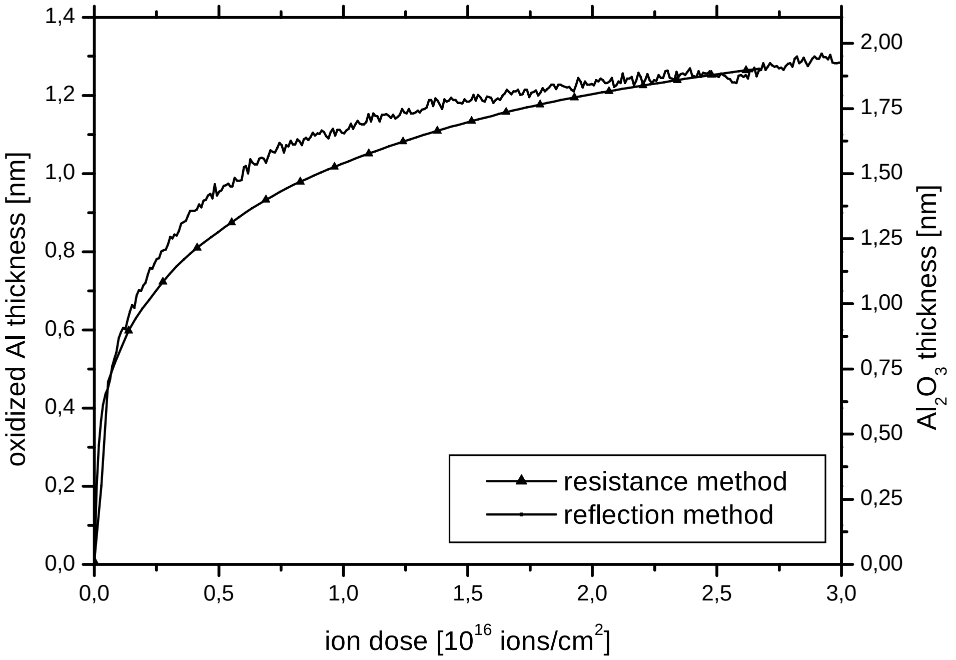

Fig: 2: Resistance and optical reflectivity measurements of thin Al films during oxidation with 30 eV O^+-ions to determine the oxidized Al layer thickness as a function of the ion dose.

ured Al_2O_3 thickness of 2.1 nm agrees very well with the value of 2.3 nm that corresponds to the initial Al layer thickness.

The oxidation depth is the most important parameter to be controlled during the oxidation process. For a reliable MTJ fabrication an optimization of the oxidation process must ensure that the oxidation process stops exactly at the Al layer/electrode interface.

We developed two independent *in-situ* techniques [3], an optical and a resistance method, for the direct determination of the oxidation depth as a function of the beam parameters. The change of resistance during the oxidation process of a thin Al stripe is measured with a four probe method. To derive the oxidation depth from the measured changes of the stripe resistance a calibration was performed on non-oxidized Al stripes. For the independent determination of the oxidation depth an *in-situ* optical reflection method was used. For small thicknesses of the metallic film its reflectivity drastically depends on its thickness. Thus, due to the fact that Al_2O_3 is transparent for visible light, the reflectivity is determined by the thickness of the non-oxidized Al layer which allows one to determine the oxide layer thickness. Reflectivity measurements provide a simple and reliable tool for the determination of the thickness of a non-oxidized Al-layer.

Figure 2 shows the oxidized Al layer thickness determined from the change of resistance of a 10 nm thick Al stripe and from the measured reflectivity change of a 1.8 nm thick Al film during oxidation with 30 eV O^+-ions. Directly after starting the oxidation process a few monolayers of Al oxidize rapidly. Then the oxidation process slows down, and diffusion is the dominant oxidation process. Note here that the ion dose range (10^{16} ions/cm^2) indicates a high efficiency of the oxidation process using ionized atomic oxygen beams. After exposing the sample to high (> 10^{17} ions/cm^2) doses the diffusion slows down and saturates soon completely. The process is self limiting.

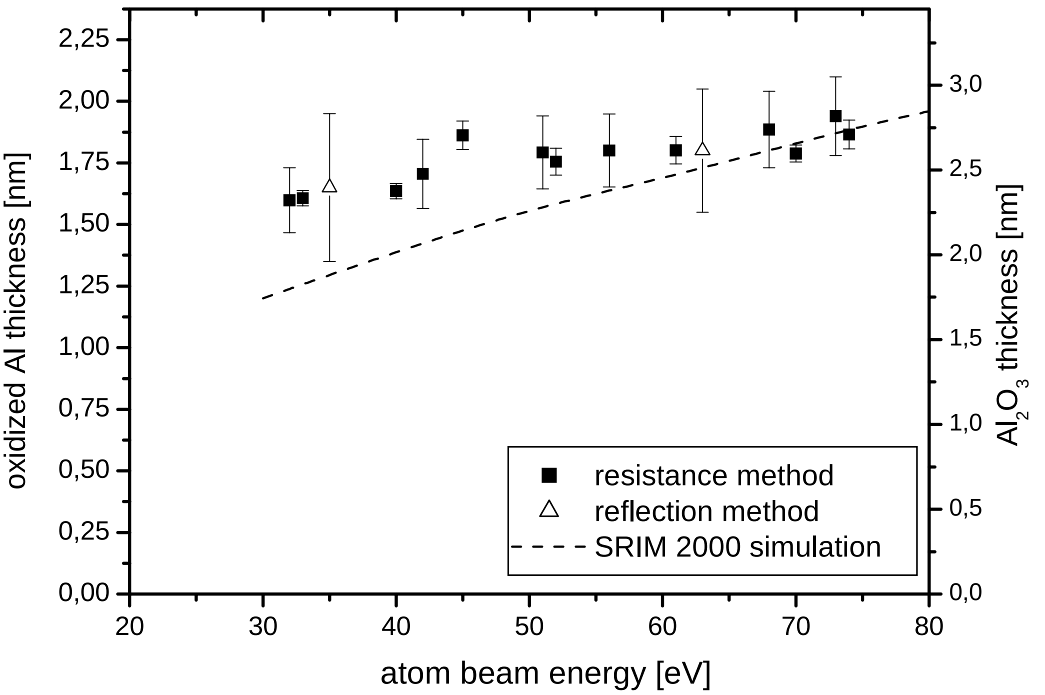

Fig. 3: Oxidation depth measured as a function of the O^+-ion beam energy at the high dose saturation limit by means of *in-situ* resistance and optical reflectivity techniques. The penetration depth is simulated using the SRIM-2000 software package.

The above *in-situ* resistance and optical reflectivity measurements were performed at various energies of the ion beam. The values of the oxidation depth at the high dose saturation limit, measured using both techniques, are presented in Fig. 3. With increasing energy of the ion beam the oxidation depth rises slightly. The observed values (1.5–2 nm) of the oxidation depth and their energy dependence can be understood on the basic assumption that the oxidation an by atom beam takes place in the region of the Al film in which the O^+-ions can penetrate. To simulate the process, we have performed Monte Carlo simulations using the TRIM [4] software package. The oxidation depth is determined from the ion penetration range assuming that each ion oxidizes the Al at the depth where it stops. No further diffusion of oxygen is taken in account. The obtained simulation curve confirms the model assumption that the oxidation region is determined by the penetration of the ions. The deviation of the simulated curve form the measured values at low ion energies is apparently due to an additional mechanism connected with the oxygen diffusion, which is mostly important at low energies of the ions.

Work supported by the Deutsche Forschungsgemeinschaft.

References

[1] T. Miyazaki, N. Tezuka, J. Magn. Magn. Matter. **139**, L231 (1995).
[2] J.S. Moodera, L.R. Kinder, T.M. Wong, R. Meservey, Phys. Rev. Lett. **74**, 3273 (1995).
[3] W. Maass, B. Roos, S.O. Demokritov, B. Hillebrands, M. Weiler, Chip 3, July 2000, 51, in: Semiconductor Industry Sourcebook, Unaxis.
[4] SRIM 2000 code, J.F. Ziegler, J.P. Biersack, U. Littmark, *The Stopping and Range of Ions in Solids*, Pergamon, New York, Oxford (1985).

6.2 Annealing effects of ion beam oxidized magnetic tunnel junctions

P.A. Beck, B.F.P. Roos, S.O. Demokritov, and B. Hillebrands

A magnetic tunnel junction (MTJ) is basically a sandwich structure consisting of two ferromagnetic layers (FM) separated by a thin insulating barrier layer. The tunneling magnetoresistance (TMR) describes the dependence of the electrical resistance of such a junction on an applied magnetic field or on the angle between the magnetizations of the two FM layers. The main applications for MTJs are non volatile magnetic random access memory (MRAM) elements and spin-valve reading heads. Recently magnetic tunnel junctions with a relative change in resistance of over 35% at room temperature were reported by several groups [1, 2]. The most popular material for a tunnel barrier is Al_2O_3, which is obtained by evaporation of metallic aluminum followed by an oxidation process. As this process, thermal oxidation, plasma oxidation or ion beam oxidation are used. It is very important for applications that MTJs can survive at high temperatures. Depending on the preparation parameters different behaviors of MTJs were found after annealing at high temperatures. *Sato* et al. [3] found an increase of the TMR ratio from 16% up to 24% for MTJs which were oxidized for a short time using an oxygen plasma. Other groups have also reported a similar increase in the TMR ratio [4]. *Kikuchi* et al. [5] have shown that the increase of the TMR is caused by a slightly oxidized layer at the bottom Co/Al interface.

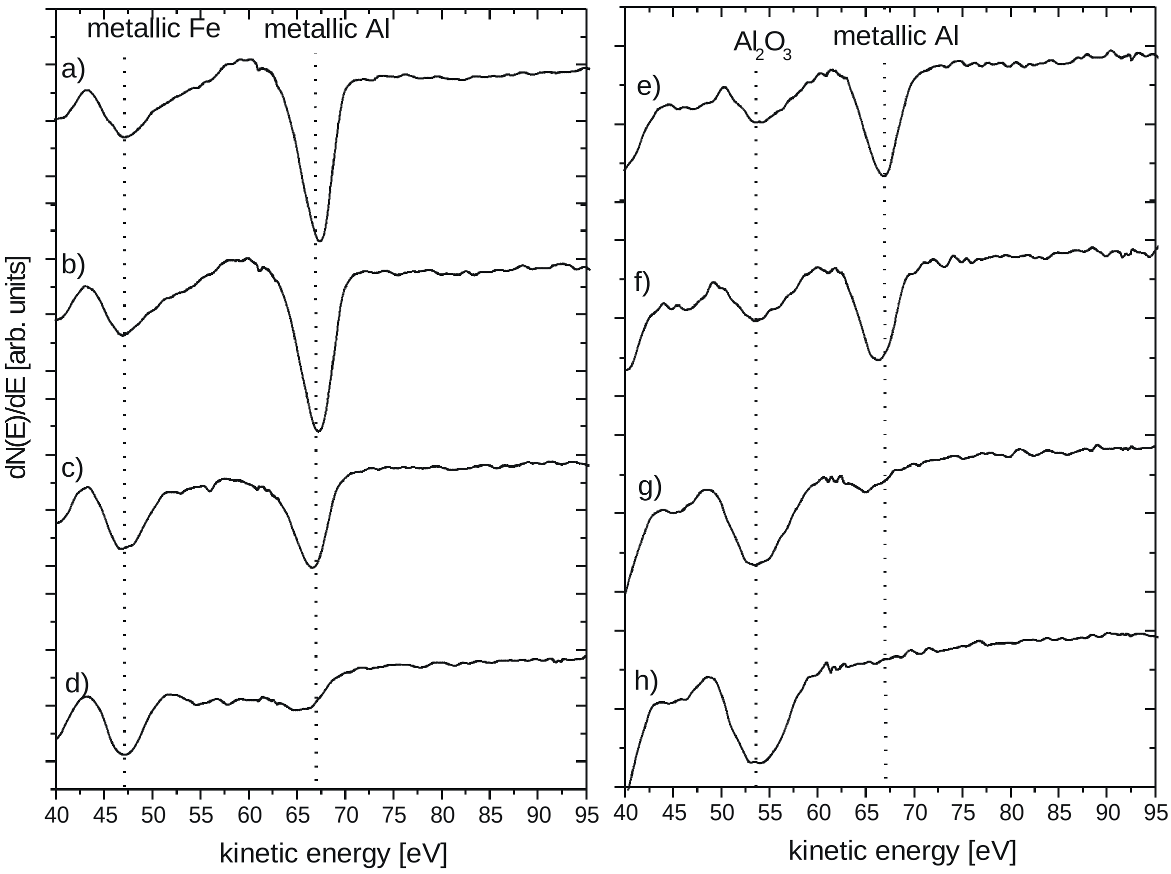

Fig. 1: AES spectra for 10 nm Fe/1.2 nm Al : (a) after deposition at room temperature; (b) after 1200 s; (c) after annealing at 370 K; and (d) after annealing at 470 K. (e) to (f) AES spectra for 10 nm Fe/FeO$_x$/ 1.2 nm Al: (e) as prepared; (f) after 1200 s; (g) after annealing at 370 K; and (h) after annealing at 470 K.

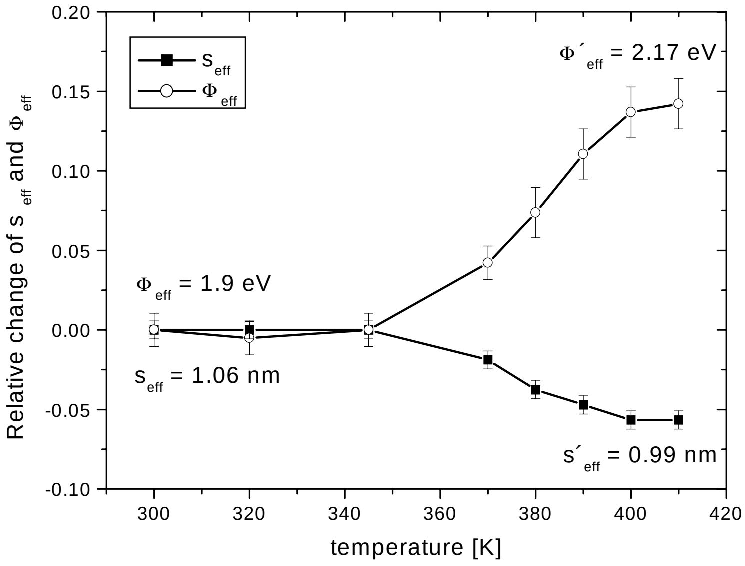

Fig. 2: Dependence of the barrier parameters s_{eff} and Φ_{eff} of a 15 nm $Ni_{81}Fe_{19}$/1.8 nm Al_2O_3/2 nm Co/12 nm Pt magnetic tunnel junction on the annealing temperature.

In this contribution we present a study of the MTJ annealing process. We are especially interested in oxygen migration over the tunnel barrier during annealing and the correlation between the properties of MTJs and the potential oxidation of the FM layers. The MTJs under investigation were prepared on a Si/SiO_2 substrate and have the layer sequence 15 nm $Ni_{81}Fe_{19}$/1.8 nm Al_2O_3/2 nm Co/12 nm Pt. The junction area was 0.25 mm^2. All samples were prepared at room temperature in a multi chamber MBE system with a base pressure less than $5\cdot10^{-10}$ mbar using shadow masks for patterning. The layers were deposited using a five pocket electron beam evaporator. The oxygen migration was investigated using Auger electron spectroscopy (AES). For these studies an incomplete MTJ of the composition Ni/NiO_x/Al/ or Fe/FeO_x/Al/ was used. Due to the small escape depth of low energy Auger electrons (few monolayers) AES is very surface sensitive. By detecting the chemical shifts of Auger peaks, it is possible to distinguish between a pure metal and its oxide. In particular the chemical shift of the Al LMM (68 eV) Auger peak near 54 eV in Al_2O_3 can be easily detected. In the first series of experiments 10 nm Fe was covered with a 1.2 nm thick Al film and then annealed in ultra-high vacuum (UHV). Figures 1a-1d illustrate the process of Fe and Al intermixing. The AES spectrum shown in Fig. 1a was recorded directly after the deposition of Al. The Auger peaks of Fe MNN (47 eV), and Al LMM (68 eV) are easily identified. The AES spectrum shown in Fig.1b was recorded 1200 s after deposition of Al. It shows no changes in positions and intensities of both AES peaks indicating no essential chemical reaction or intermixing between Fe and Al at room temperature. The AES spectra shown in Fig.1c and Fig. 1d were recorded after annealing for 600 s at T = 370 K and T = 470 K, respectively. They demonstrate the interdiffusion of Al and Fe at elevated temperatures. In a second series of experiments the Fe layer was oxidized using an ionized oxygen atom beam. Thus a thin, 1–1.5 nm thick iron-oxide layer was formed. Next the sample was covered with a 1.2 nm thick Al film. Figures 1e-1h illustrate the process of oxygen migration between Fe and Al. The AES spectrum shown in Fig.1e was recorded right after the deposition of Al on the iron-oxide layer. The Auger peak of Al in Al_2O_3 (54 eV) is already visible in the spectrum in addition to the peak at 68 eV corresponding to metallic Al. The presence of the Al_2O_3-peak indicates an essential migration of oxygen from FeO_x to Al even at room temperature. After 1200 s (see the AES spectrum in Fig. 1f) there is no significant change. The AES spectra recorded after annealing for 600 s at T = 370 K (Fig. 1g) and T = 470 K (Fig. 1h) demonstrate an increasing migration of oxygen at elevated temperatures. The metallic Al peak at 68 eV disappeares after annealing at T = 470 K indicating a complete oxidation of the Al layer. The oxygen

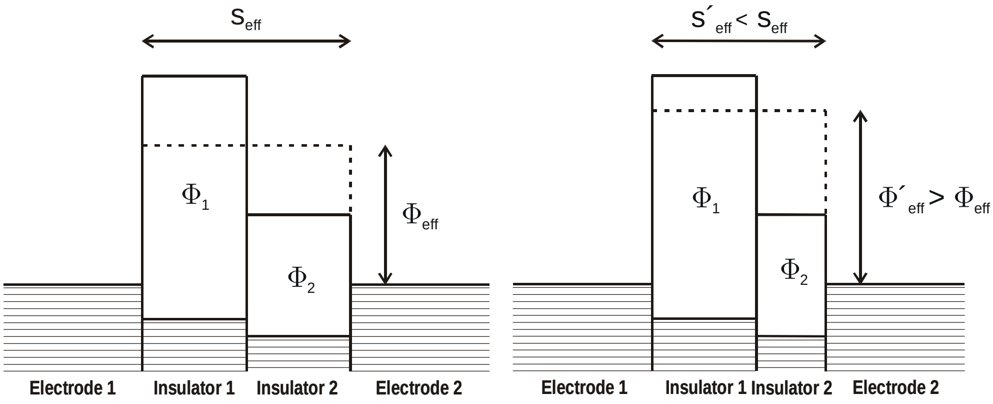

before annealing

after annealing

Fig. 3: Simple rectangular model of an MTJ with the barrier made of two different insulators (a) before annealing and (b) after annealing.

necessary for the oxidation of the Al layer must originate from the FeO$_x$ layer. It cannot be obtained from the residual gas, since no Al_2O_3 is detected in the AES spectra presented in Fig. 1a-d, and since both series of experiments were performed under the same vacuum conditions. The deoxidization of FeO$_x$ by Al is caused by the higher electron affinity of Al compared to Fe. Finally, it is also clear from Fig. 1e-h that there is no interdiffusion between Fe and Al through Al_2O_3., since no additional peaks corresponding to Fe or FeO$_x$ appear after the annealing process. Thus, the Al_2O_3 layer acts as a diffusion barrier.

The MTJs with the layer sequence Si/SiO$_2$/15 nm Ni$_{81}$Fe$_{19}$/NiFeO$_x$/1.8 nm Al_2O_3/2 nm Co/12 nm Pt were annealed up to 410 K for 1800 s in an oven with a pressure of less than 10^{-2} mbar. The measued $I(V)$ curves were obtained at room temperature with an applied magnetic field of 300 Oe, which aligns the magnetization of the two FM electrodes parallel to each other. The barrier height Φ_{eff} and the barrier width s_{eff} were calculated by fitting the measured $I(V)$ curves by the Brinkman equation [6]. Figure 2 shows the relative change of Φ_{eff} and s_{eff} after annealing as a function of the annealing temperature. Up to 345 K there is no significant change in both values. However, for $T_{an} > 370$ K, Φ_{eff} increases and s_{eff} decreases after annealing. The TMR is increasing similar to Φ_{eff} from 10 % up to 13 %.

The above results can be understood on the basis of a simple model, as illustrated in Fig. 3. It shows the rectangular potential barriers of Al_2O_3 (higher barrier height Φ_1) and NiFeO$_x$ (lower barrier height Φ_2) in the MTJ. Figures 3a and 3b correspond to the MTJ before and after annealing, correspondingly. Due to the ability of aluminum to deoxidize other oxides, oxygen migrates from the NiFeO$_x$ layer to the Al_2O_3 layer during the annealing process. The effective barrier hight Φ_{eff} obtained from the fit of the measured $I(V)$-curves represents an average value between Φ_1 and Φ_2. Since in the annealing process oxygen migrates from NiFeO$_x$ to Al_2O_3, the former layer becomes thinner while the latter becomes thicker. Thus, the effective barrier Φ_{eff} increases due to the higher barrier height of Al_2O_3.

In summary, we fabricated magnetic tunnel junctions with a barrier formed using an ionized oxygen beam. It was shown that aluminum may deoxidize oxides of Fe and Ni, and Al_2O_3 acts as an diffusion barrier for the metals used. A simple model is proposed to understand the change of the barrier height with annealing in agreement with AES studies.

Work supported by the Deutsche Forschungsgemeinschaft and the BMBF (Leitprojekt Magnetoelektronik).

References

[1] S. S. Parkin, K.-S. Moon, K. E. Pettit, *Magnetic tunnel junctions termally stable to above 300°C*, Appl. Phys. Lett. **75**, 543 (1998).

[2] R. C. Sousa, J. J. Sun, V. Soares, P.P. Freitas, *Large tunneling magnetoresistance enhancement by thermal anneal*, Appl. Phys. Lett. **73**, 3288 (1998).

[3] M. Sato, H. Kikuchi, *Ferromagnetic tunnel junctions with plasma-oxidized Al barriers and their annealing effects*, J. Appl. Phys. **83**, 6691 (1998).

[4] S. Cardoso, P. P. Freitas, *Spin-tunnel-junction thermal stability and interface interdiffusion above 300°C*, Appl. Phys. Lett. **76**, 610 (2000).

[5] H. Kikuchi, K. Kobayashi, M. Sato, *The annealing effect of spin-valve-like ferromagnetic tunnel junctions*, J. Magn. Soc. Jpn. **23**, 49 (1999).

[6] W. F. Brinkman, R. C. Dynes, J. M. Rowell, *Tunneling Conductance of Asymmetrical Barriers*, J. Appl. Phys. **41**, 1915 (1970).

B. Dynamic Magnetic Phenomena

6.3 Magneto-dipole coupling in arrays of micron-size rectangular magnetic elements

C. Krämer, J. Jorzick, S.O. Demokritov, and B. Hillebrands[1]

Due to the increasing interest in high-density magnetic memory devices (MRAM) it is essential to study the dynamic and static properties of close packed arrays of magnetic elements. In this contribution an experimental study of the static properties of rectangular micron-size magnetic elements arranged in arrays investigated by magneto-optic Kerr-effect magnetometry (MOKE) and magnetic force microscopy (MFM) is presented while the dynamic properties will be discussed in Chapter 6.4.

The samples were prepared from $Ni_{81}Fe_{19}$ films, which were grown in an UHV chamber by means of e-beam evaporation. Before patterning the samples were tested by MOKE. They show a low coercivity and negligible in-plane anisotropy as indications of the high quality of the samples. Patterning was performed using e-beam lithography and ion-etching. The rectangular elements have a thickness of 35 nm with lateral dimensions of 1×1 μm^2, 1×1.2 μm^2 and 1×1.75 μm^2 and varying spacing between the samples (0.1, 0.2, 0.5, and 1 μm). They were arranged in arrays with total lateral dimensions of 800×800 μm^2.

The hysteresis loops of the patterned sample reveal much higher coercivities and saturation fields than the unpatterned film, and they show the expected in-plane anisotropy when rotated in the external field. This is displayed in Fig. 1 showing a four-fold configurational anisotropy for the

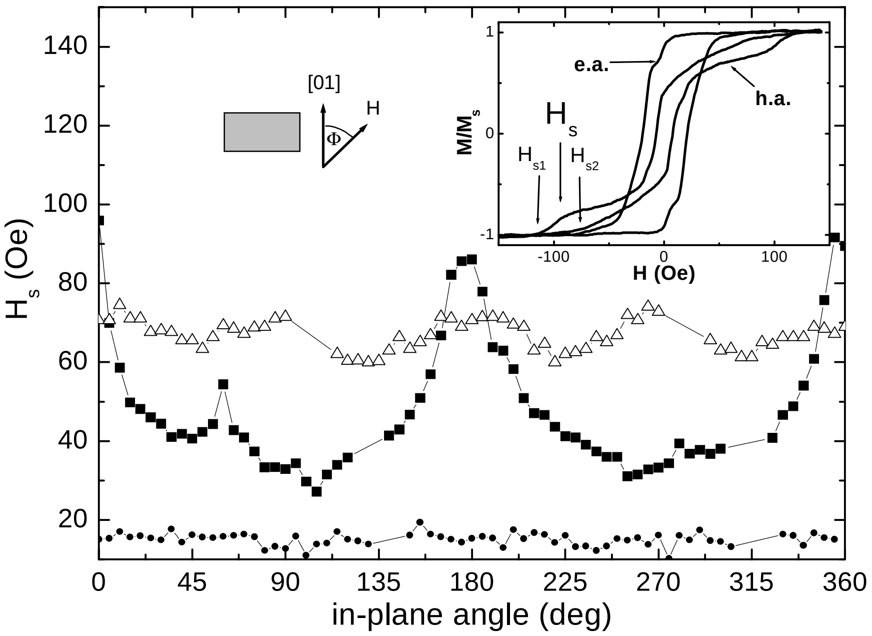

Fig. 1: Saturation field as a function of the in-plane angle measured with respect to the short axis of the element: small dots: continuous film; open triangles: array of 1×1 μm^2 square elements with spacing $\delta = 0.1$ μm, full squares: array of 1×1.75 μm^2 rectangular elements with spacing $\delta = 0.1$ μm. The inset shows the magnetization curves along the easy and hard axes for the 1×1.75 μm^2 array.

---

[1] In collaboration with E. Søndergard, M. Bailleul, and C. Fermon, CEA Saclay, Service de physique de l'état condense, Gif sur Yvette, Cedex, France, U. Memmert, A.N. Müller, and U. Hartmann, Institut für Experimentalphysik, Universität Saarbrücken, Germany, and E.Y. Tsymbal, Department of Materials, University of Oxford, Oxford, United Kingdom.

square sample and a two-fold, shape-dominated anisotropy for the rectangular samples. The anisotropy increases for larger lateral aspect ratios. The easy axis lies along the long axis of the element. Typical examples of the magnetization curves measured for the magnetic field applied along the long and short sides of the rectangles are presented in the inset of Fig.1. The experimental value of the saturation field is obtained by averaging over the two values H_{s1} and H_{s2} as also shown in Fig. 1; this is done to compensate for hysteresis effects.

Although the observed magnetic anisotropy is strongly correlated with the shape of the elements, it depends on the inter-element spacing. This is shown in Fig. 2 where the saturation field is plotted as a function of the spacing between the elements for the series of samples with the lateral dimensions of 1×1.75 µm^2 with the field applied along the easy (squares) and hard (circles) axis. A sizeable increase in the saturation field with increasing spacing and nearly constant values for large spacings demonstrates an essential dipolar interaction. For large spacings (well above 0.7 µm) the elements are isolated and the value of the saturation field is determined by the demagnetizing field of a single element which increases strongly at the edges of the element due to its non-ellipsoidal shape. Bringing the elements closer together, the demagnetizing fields of the elements partly compensate each other resulting in a lower value for the saturation field, and finally the value for zero spacing (continuous film) is determined by the intrinsic coercivity of the sample. An analytical approach [1] reproduces the experimentally obtained results as also shown in Fig. 2. However the calculated values of the saturation field in the middle of the elements are lower due to the strong increase of the dipolar field at the element edges resulting in higher values in the experimental data, but showing the same qualitative behavior

The dipolar interaction for elements with small inter-element spacing is also obvious from MFM measurements as shown in Fig. 3. The elements with lateral dimensions of 1×1.75 µm^2 and 0.1 µm separation are saturated by a field of 120 Oe applied along the easy axis. Applying a reversal field with a value of 48 Oe the magnetization reversal starts and a complete row of elements switches as can be seen in Fig. 3a in the second row from the bottom. Increasing the reversal field all rows switch, until at a field of 64 Oe only one row keeps the initial magnetization state (Fig. 3b). This intra row interaction is very strong for the elements with small spacing and vanishes for larger element separation. However there is also inter row interaction present which

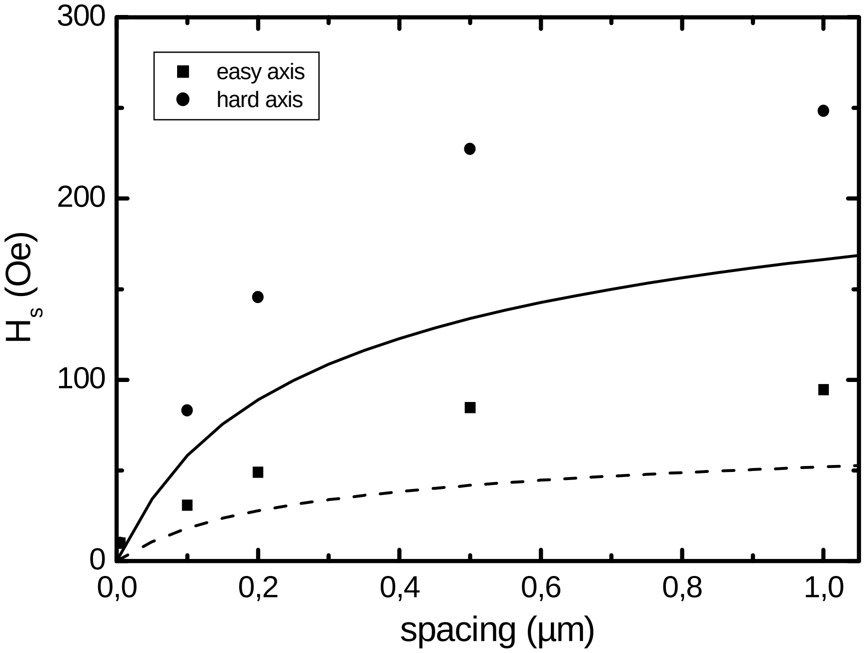

Fig. 2: Measured and calculated saturation fields as functions of the inter-element spacing for the sample with the lateral dimensions of 1×1.75 µm^2 for the easy (squares) and hard axis (circles) showing the essential dipolar interaction between the elements for small separations. The lines show the results of an analytical approach for the saturation field in the middle of the elements for the easy (dotted line) and hard axis (solid line).

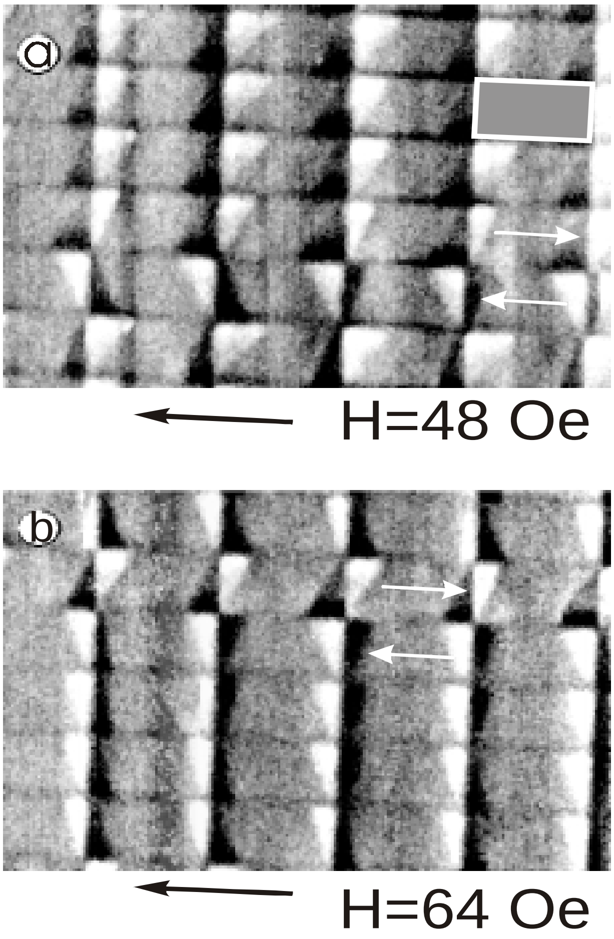

Fig. 3: MFM images (6.5×9 μm^2) of the array of the 1×1.75 μm^2 rectangular elements recorded during a magnetization reversal process. The sample was magnetized at 120 Oe. (a) MFM image taken at –48 Oe. The gray rectangle indicates a single element; the white arrows indicate the main orientation of the magnetization within the element. (b) MFM image taken at –64 Oe.

is much weaker, but can be observed when the samples are demagnetized in an ac-field. Demagnetizing the arrays of elements along the easy axis, a single row still keeps the magnetization in one direction with resulting magnetic charges that are positioned close to the short edges of the elements. However this direction is reversed in the neighboring row, so that the whole array is demagnetized. This is surprising because one might think that it is energetically favorable to have the single element demagnetized. This state can indeed be obtained, when the ac-field is applied along the hard axis of the elements and most of the elements are found in the Landau state.

A full report about the static properties is published in Ref. [2].

Work supported by the Deutsche Forschungsgemeinschaft, the BMBF (Leitprojekt Magnetoelektronik) and the EC-TMR program "DYNASPIN" No. FMRX-CT97-0124.

References

[1] E.Y. Tsymbal, J.Magn. Magn.Mat. **130**, L6 (1994).
[2] J. Jorzick, C. Krämer, S.O. Demokritov, B. Hillebrands, E. Søndergard, M. Bailleul, C. Fermon, U. Memmert, A.N. Müller, U. Hartmann, E.Y. Tsymbal, submitted to Phys. Rev. B.

6.4 Spin waves in arrays of interacting, micron-size rectangular magnetic elements

J. Jorzick, C. Krämer, S.O. Demokritov, and B. Hillebrands[1]

Earlier Brillouin light scattering (BLS) studies of micron-size wires and circular dots in our group have demonstrated new physical phenomena, like i) the lateral spin wave quantization effect in a single element, which is due to the confinement of the spin wave modes in the element, and ii) dynamic coupling between elements [1-3]. By measuring the BLS cross section as a function of the transferred wave vector the mode profiles are accessible [1, 2]. The frequencies of the modes in the wires and their profiles have been described for wires in the framework of a model which considers lateral standing waves with quantized values of the in-plane wave vector [1, 2]. In this contribution we focus on spin wave properties of micron-size rectangular magnetic elements.

The samples under investigation are rectangular shaped (1×1, 1×1.2 and 1×1.75 μm^2), 35 nm thick FeNi (permalloy) elements arranged in arrays with the over-all dimensions of 800×800 μm^2. The sample preparation as well as the static magnetic properties of the samples are described in Chapter 6.3. Figure 1 shows BLS spectra obtained for an array of elements with the lateral dimensions of 1×1.75 μm^2 and 0.1 µm element separation for a transferred wave vector of $q_{||} = 0.75 \cdot 10^5$ cm^{-1} and an external field of $H = 600$ Oe.

Several quantized spin wave modes confined in the element (indicated in the figure by arrows) are clearly seen. The two shown spectra were recorded for different orientations of the transferred in-plane wave vector with respect to the magnetization ($\mathbf{q}_{||} \parallel \mathbf{M}$ and $\mathbf{q}_{||} \perp \mathbf{M}$, respectively). Since the BLS cross section at a given value and direction of $\mathbf{q}_{||}$ is determined by the corresponding Fourier component of the dynamic mode profile, the observed difference in the intensities of the modes indicates already different mode profiles along the two in-plane directions.

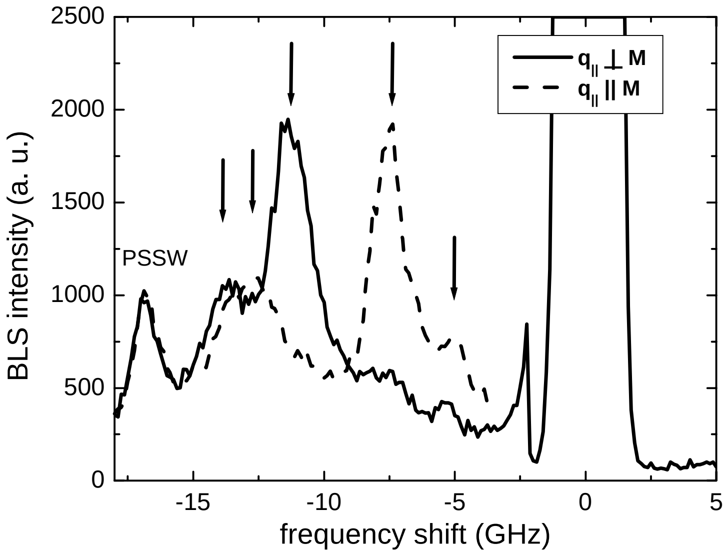

Fig. 1: Typical BLS spectra for a sample with the lateral dimensions of 1×1.75 μm^2 and an inter-element spacing of 0.1 µm for different geometries ($\mathbf{q}_{||} \parallel \mathbf{M}$ and $\mathbf{q}_{||} \perp \mathbf{M}$). At 17 GHz the exchange dominated perpendicular standing spin wave mode (PSSW) is observed.

---

[1] In collaboration with E. Søndergard, M. Bailleul, and C. Fermon, CEA Saclay, Service de physique de l'état condense, Gif sur Yvette, Cedex, France.

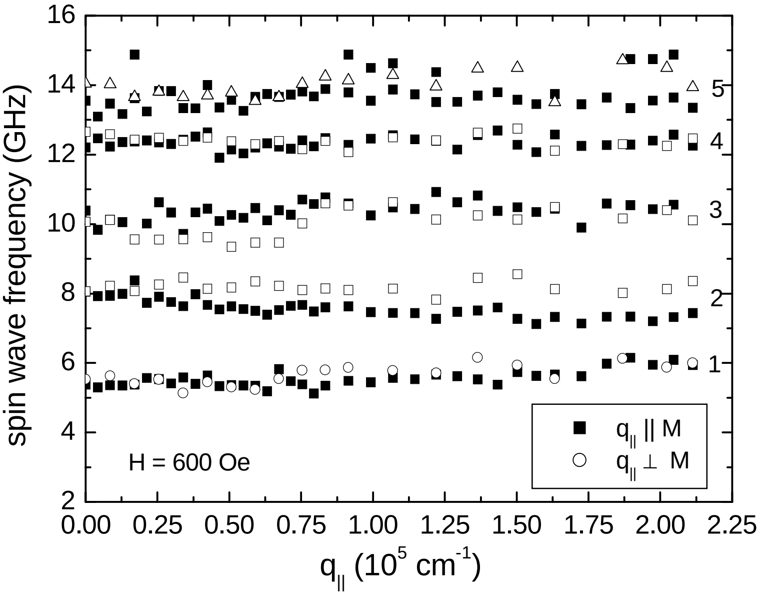

Fig. 2: Frequencies of spin wave modes (numbered on the right side of the graph) as a function of the transferred in-plane wave vector for two scattering geometries, obtained in an array with the lateral dimensions for each element of 1×1.75 μm^2 and the element separation of 0.1 μm. An external field of H = 600 Oe is applied.

By changing the angle of light incidence the transferred wave vector $\mathbf{q}_{||}$ is varied and the mode dispersion $\omega(\mathbf{q}_{||})$ is obtained as shown in Fig. 2. Similar to the modes in the wires the detected modes show no dispersion (ω = const) over a large wave vector interval. The measured frequencies of the quantized spin wave modes presented in Fig. 2 are the same for both geometries used. The BLS intensity for a given mode, however, depends on the value and the direction of the transferred wave vector. Measuring the intensities as a function of the transferred in-plane wave vector one can obtain information on the mode profile by a comparison of the experimental data to the Fourier transform of assumed mode amplitude profiles [1, 2]. The BLS intensity of the mode with the frequency $\omega/2\pi$ = 10 GHz measured for the sample with the lateral dimensions of 1×1.75 μm^2 and a separation between the elements of 0.1 μm is presented in Fig. 3. For the geometry $\mathbf{q}_{||} \perp \mathbf{M}$ a typical curve with a typical maximum, similar to those obtained for the modes in the wires, is measured. It is consistent with the mode profile shown in the inset. For the geometry $\mathbf{q}_{||} \parallel \mathbf{M}$, however, the BLS intensity is almost independent of the in-plane wave vector. Essential Fourier components corresponding to high values of the wave vector indicate small width, or localization of the mode profile along the measured direction. It is impossible to determine directly the position of the localization region from the BLS-data. However, the edges of the element perpendicular to the magnetization are apparently potential regions for spin wave localization. In fact, due to the non-ellipsoidal shape of an element the demagnetizing field is non-uniform over the element. The profile of the demagnetizing field of a uniformly magnetized rectangular element calculated in [4] shows a strongly increasing field near the edges. The internal field, which is a sum of the applied field and the demagnetizing field, is plotted in Fig. 4 for the applied field of H = 600 Oe used in the experiments. Areas of negative internal field near the edges mark regions of non-saturated magnetization, i.e., the formation of (partial) domains. Contrary to the remaining parts of the element the static internal field in these regions is zero. Since the internal field changes dramatically over the element, the spectra of the spin waves in the saturated and in the non-saturated parts of the element are different. Therefore, the partial domain walls separating the saturated and non-saturated parts act as localization walls for the spin wave mode. Moreover, the spin wave modes localized in the non-saturated regions mainly contribute to the BLS cross section, since they have large amplitudes due to high magnetic susceptibility at zero internal field.

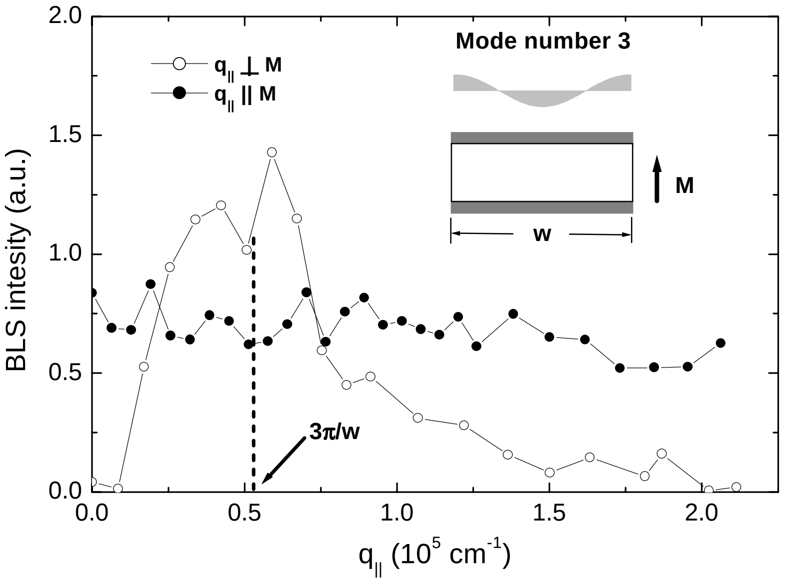

Fig. 3: BLS intensity from the mode with the frequency 10 GHz (mode number 3 in Fig. 2) as a function of the transferred in-plane wave vector for two scattering geometries. Inset: bottom: sketch of the element under consideration with gray color marking non-saturated parts; top: a mode profile consisting with the measured BLS intensities.

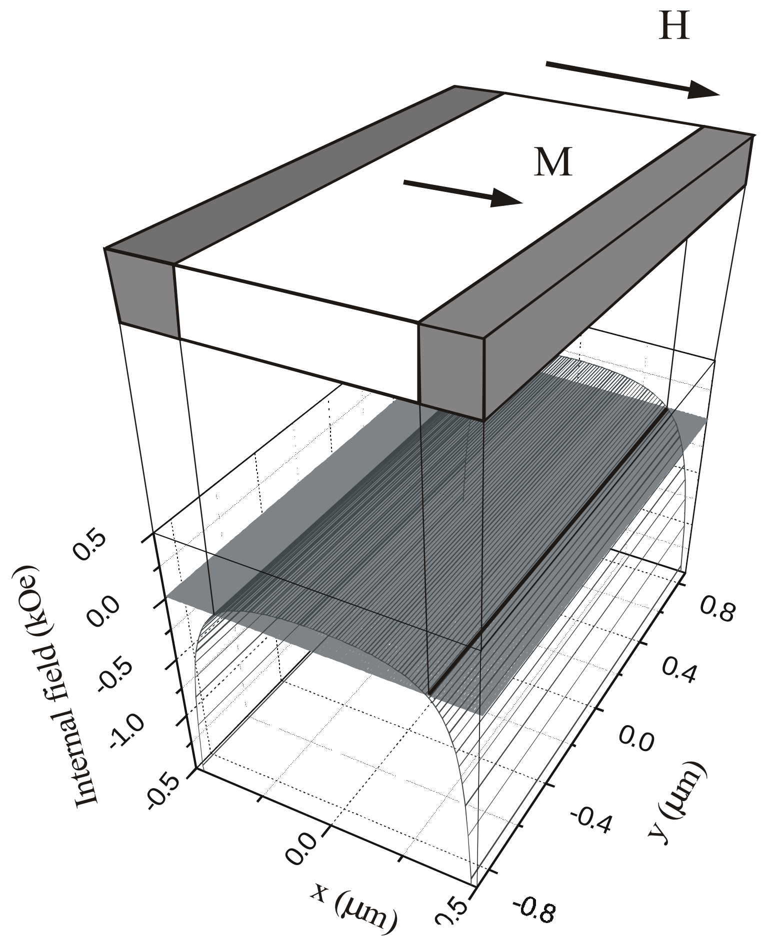

Fig. 4: Calculated internal field over a uniform magnetized permalloy element with the lateral dimensions of 1×1.75 μm^2 , demonstrating a dramatic increase of the demagnetizing field near the edges of the element. An external field of $H = 600$ Oe is applied as shown. In the regions of a negative internal field near the edges of the element (marked gray) domains with an non-saturated magnetization are created.

Work supported by the Deutsche Forschungsgemeinschaft, the BMBF (Leitprojekt Magnetoelektronik) and the EC-TMR program "DYNASPIN" No. FMRX-CT97-0124.

References

[1] C. Mathieu, J. Jorzick, A. Frank, S.O. Demokritov, B. Hillebrands, A.N. Slavin, B. Bartenlian, C. Chappert, D. Decanini, F. Rousseaux, E. Cambril, Phys. Rev. Lett. **81**, 3968 (1998).

[2] J. Jorzick, S.O. Demokritov, B. Bartenlian, C. Chappert, F. Rousseaux, A.N. Slavin, B. Hillebrands, Phys. Rev. B **60**, 15194 (1999).

[3] J. Jorzick, S.O. Demokritov, B. Hillebrands, B. Bartenlian, C. Chappert, D. Decanini, F. Rousseaux, E. Cambril, Appl. Phys. Lett. **75**, 3859 (1999).

[4] R.I. Joseph, E. Schloemann, J. Appl. Phys. **36**, 1679 (1965).

.

6.5 Successful suppression of magnetization precession after short field pulses by static field variation

M. Bauer, R. Lopusnik, J. Fassbender, and B. Hillebrands[1]

The investigation of the magnetization dynamics has become technologically important [1-8], in particular since the data rate for magnetic recording approaches now values above 1 Gbit/s. One issue is to maximize the switching speed of the read heads or, for the same reason, of MRAM storage elements. If the applied field is abruptly changed by, e.g., the application of a very short magnetic field pulse, generally a damped precession of the magnetization occurs, so-called magnetic ringing. In a device the appearance of ringing will increase the dead time between two consecutive switching events, and thus must be avoided.

It has been predicted by numerical simulations [9] and experimentally verified [7] that the magnetization ringing can be suppressed by tailoring the length of the applied field pulse. Moreover it has been demonstrated that the ringing in magnetization dynamics can also be suppressed by an appropriate timing between two field step excitations propagating in opposite directions [8]. Here it is demonstrated, that for fixed pulse parameters the control of the ringing amplitude can also be realized by the variation of the strength of a constant static field which affects the precession frequency.

The main advantage of ringing suppression over tailoring the magnetic damping mechanism is that for the former case damping effects are of only minor importance. In particular, it is not necessary to increase the magnetic damping parameter to suppress the magnetization precession.

The results presented here were obtained by means of a time resolved magneto-optical Kerr effect (TIMO) magnetometer [8]. A 1 mm square, 1.5 µm thick film of lutetium substituted bismuth iron garnet, $Lu_{2.04}Bi_{0.96}Fe_5O_{12}$, was investigated, which was grown by liquid phase epitaxy onto one side of a (111) oriented gadolinium gallium garnet of thickness of 0.4 µm. The magnetic parameters are the nominal saturation magnetization $4\pi M_s$ of 1750 G and a half maximum ferromagnetic resonance (FMR) linewidth of 0.9 Oe at 8.1 GHz [10]. Static hysteresis loop measurements indicated no significant anisotropy other than shape anisotropy. Iron garnet films are known to exhibit a very low magnetic damping constant [11]. Therefore, the pronounced ringing can be excited and observed within long time which allows to rigorously verify the suppression ringing mechanism on the time scale shorter than the damping time.

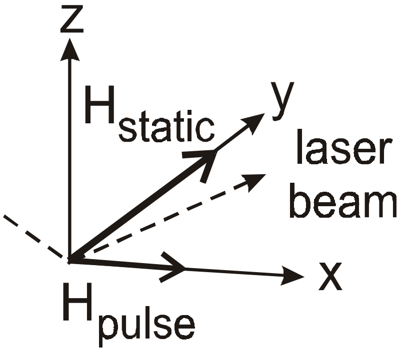

Fig. 1: Geometry of the experiment.

---

[1] In collaboration with H. Dötsch, Fachbereich Physik, Universität Osnabrück, Germany.

Figure 1 shows the experimental geometry. The initial orientation of magnetization is set by the in-plane static field $\mathbf{H}_{\mathrm{static}}$, which is applied perpendicular to the plane of light incidence in the TIMO setup. A fast rise-time current pulse (duration 18 ns, rise and fall time 0.4 ns, amplitude 1.6 Oe, repetition rate 100 kHz) is applied to a 0.3 mm wide microstrip antenna with the film on top, face up, producing a magnetic field pulse. Its direction lies in the film plane and perpendicular to $\mathbf{H}_{\mathrm{static}}$. The magnetization response is probed by a 10 pJ diode laser pulse with 15 ps duration and a wavelength of 810 nm applied with a computer controlled delay time. The TIMO

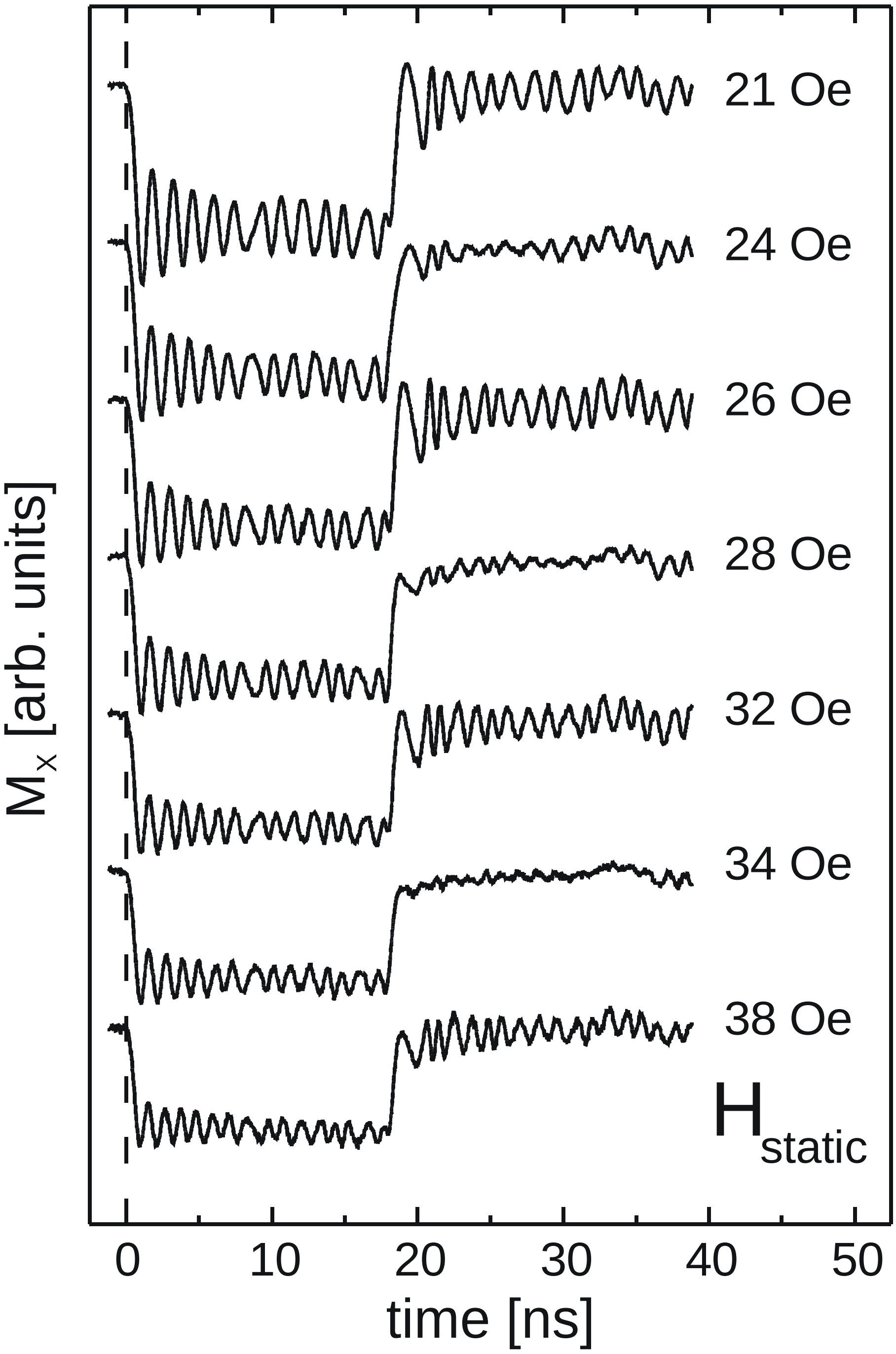

Fig. 2: Time evolution of the x-component of the magnetization, M_x, measured at the center of the sample during and after field pulse excitation for different static magnetic field values, H_{static}, as indicated. The magnetic field pulse amplitude is 1.6 Oe and the pulse length is 18 ns. The pulse is turned on at time $t = 0$.

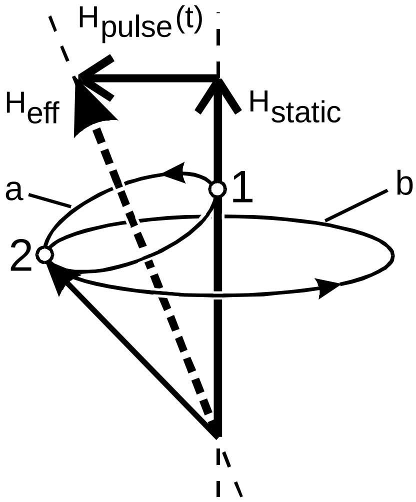

Fig. 3: Magnetization motion before, during and after the application of the magnetic field pulse. $\mathbf{H}_{\text{static}}$, $\mathbf{H}_{\text{pulse}}$, and $\mathbf{H}_{\text{eff}}$ denote the static, pulse, and corresponding effective magnetic fields. "*a*" and "*b*" denote traces of the magnetization vector about the effective and static fields, respectively. Upon field termination in point "1" the ringing is maximally suppressed, whereas in point "2" the oscillations are most pronounced.

signal as a function of the delay time yields the magnetization dynamics. The light was *s*-polarized and applied at an angle of 55° with respect to the surface normal, yielding a signal proportional to the longitudinal magnetization component only, i.e., to the component of magnetization along the pulsed field direction. The jitter limited time resolution was estimated to be better than 100 ps. Meanwhile an improvement of the time resolution has been achieved (see Chapter 6.15).

The magnetization response for several different static field values H_{static} is shown in Fig. 2. The oscillating behavior of the ringing amplitude after field pulse termination is observed as a function of H_{static}. The ringing is suppressed at $H_{\text{static}} = 24$ Oe, 28 Oe, and 34 Oe. A pronounced ringing is observed for $H_{\text{static}} = 21$ Oe, 26 Oe, 32 Oe, and 38 Oe. An increase in H_{static} causes: i) an increase in the precession frequency, and ii) a decrease in the tilt angle between the magnetization and $\mathbf{H}_{\text{static}}$ due to the constant pulse field magnitude. For two consecutive minima in the ringing amplitude the number of precession periods during the application of the pulse differs by one (see Fig. 2). During the field pulse ringing is always observed.

The ringing behavior after field pulse termination is mainly governed by the actual magnetization direction with respect to the static field direction at the moment when the pulse terminates. The effect is understood in terms of precession timing arguments. We first discuss the simplified case of a rectangular pulse and a medium without shape anisotropy and damping. Figure 3 provides simple insight into the magnetization processes which may be considered in three steps. (i) Before the pulse, the magnetization is aligned parallel to $\mathbf{H}_{\text{static}}$ and there is no precession. (ii) Once the pulse field is applied, the magnetization immediately begins precessional motion about the new effective field direction, given by the vectorial sum $\mathbf{H}_{\text{pulse}} + \mathbf{H}_{\text{static}}$. (iii) In absence of damping, the precessing magnetization vector will periodically return to its initial position (trace "*a*" in Fig. 3). If the pulse field terminates in point "1" in Fig. 3, when the magnetization is aligned with the static magnetic field, no ringing of the magnetization will occur since no torque is acting on the magnetization at this point. On the other hand, if the magnetization is at point "2" when the pulse terminates, the magnetization and $\mathbf{H}_{\text{static}}$ form an angle, and the acting torque will force the magnetization to precess along trace "*b*". A pronounced ringing is observed. This scenario can be realized either by changing the pulse duration and/or the amplitude of the static applied field. For inclusion of shape anisotropy, damping, and a realistic pulse shape the basic concept remains the same although the trace of precession is remarkably more complicated.

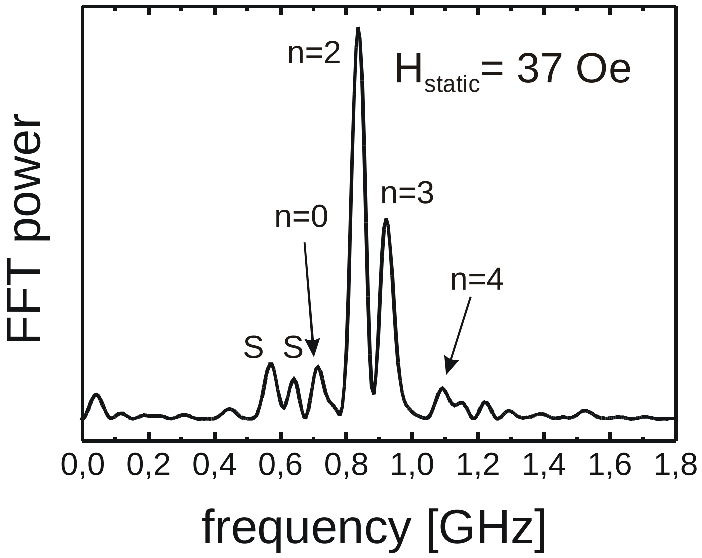

Fig. 4: Typical fast Fourier transform (FFT) power vs. frequency spectrum for ringing response time signals. The static field for these data was 37 Oe. The FFT analysis was for the ringing signal after pulse turn off. The *n* and *S* labels show the various modes with which the peaks may be identified.

In order to quantify the precessional nature of the response a FFT analysis of the ringing signals was done. Figure 4 shows a typical power spectrum. Several strong frequency components in the ringing response are observed. The *n*-values for the four peaks between 0.7 and 1.1 GHz label the resonance modes which appear to be associated with these peaks. For H_{stat} values above about 20 Oe, these peak positions track the predicted frequencies for uniform mode FMR ($n = 0$) and the low order spin wave resonance modes for unpinned surface spins with two ($n = 2$), three ($n = 3$), and four ($n = 4$) standing wave half wavelengths across the film. For lower fields, the measured peak positions fall below these predicted frequencies. The peaks labeled *S* in Fig. 4 fall below the FMR frequency. This is suggestive of surface modes created by partial pinning and surface anisotropy (see Chapter 6.6).

In order to provide an explicit and qualitative map of ringing suppression as a function of static field, the FFT peaks intensities corresponding to the ringing response during and after field pulse were examined. The results are presented in Fig. 5. The FFT peak intensity ratio is defined as a ratio of the peak intensity for the ringing after pulse turn off, where suppression is active, to the

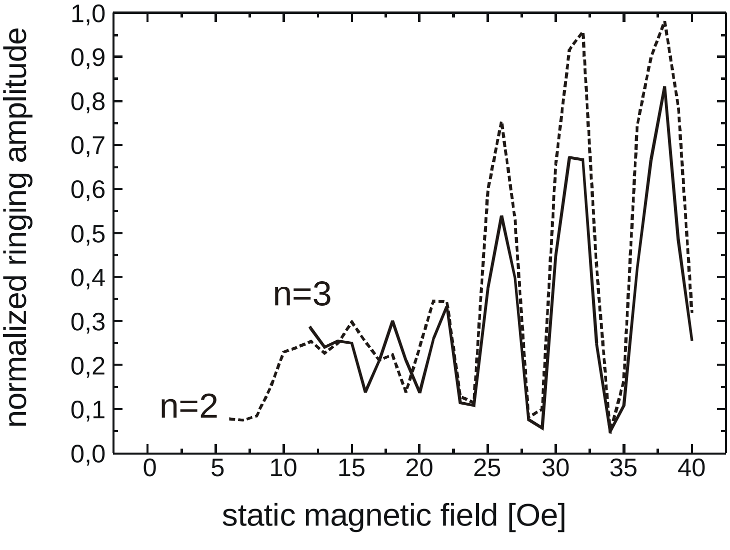

Fig. 5: Normalized FFT peak intensity ratio as a function of static field for the two strongest, $n = 2$ and $n = 3$, peaks in the FFT spectra. The vertical axis corresponds to the ratio of the FFT peak intensities for the pulse on and the pulse off signals.

corresponding intensity for the ringing during pulse is turned on, where precessional behavior is always present. The data are shown for the two strongest peaks, $n = 2$ and $n = 3$, in the FFT spectra. The maxima and minima occur at the same field values for *both* components of the FFT response. Note that the maxima increase and the minima decrease with static field. This means that the ringing suppression is actually enhanced for higher static fields.

Work supported by Siemens AG, the German Ministry of Research and Technology (BMBF), and the EC-TMR program "DYNASPIN" No. FMRX-CT97-0124. EMCO Elektronik, GmbH is gratefully acknowledged for the use of an ultra fast pulse generator for the measurements.

References

[1] W.K. Hiebert, A. Stankiewicz, M.R. Freeman, Phys. Rev. Lett. **79**, 1134 (1997).
[2] M.R. Freeman, W.K. Hiebert, A. Stankiewicz, J. Appl. Phys. **83**, 6217 (1998).
[3] R.H. Koch, J.G. Deak, D.W. Abraham, P.L. Touilloud, R.A. Altman, Yu Lu, W.J. Gallagher, Phys. Rev. Lett. **81**, 4512 (1998).
[4] T.J. Silva, C.S. Lee, T.M. Crawford, C.T. Rogers, J. Appl. Phys. **85**, 7849 (1999).
[5] C.H. Back, J. Heidmann, J. McCord, IEEE Trans. Magn. **35**, 637 (1999).
[6] T.M. Crawford, T.J. Silva, C.W. Teplin, C.T. Rogers, Appl. Phys. Lett. **74**, 3386 (1999).
[7] M. Bauer, R. Lopusnik, J. Fassbender, B. Hillebrands, Appl. Phys. Lett. **76**, 2758 (2000).
[8] T.M. Crawford, P. Kabos, T.J. Silva, Appl. Phys. Lett. **76**, 2113 (2000).
[9] M. Bauer, J. Fassbender, B. Hillebrands, R.L. Stamps, Phys. Rev. B **61**, 3410 (2000).
[10] M. Bauer, C. Mathieu, S.O. Demokritov, B. Hillebrands, P.A. Kolodin, S. Sure, H. Dötsch, V. Grimalsky, Yu. Rapoport, A.N. Slavin, Phys. Rev. B **56**, R8483 (1997).
[11] *Ferromagnetic Materials*, ed. by E.P. Wohlfarth, Amsterdam, North-Holland (1980).

6.6 Analysis of exchange surface modes in Bi substituted yttrium iron garnet films

C. E. Patton, R. Lopusnik, M. Bauer, J. Fassbender, and B. Hillebrands

Time resolved magneto-optic (TIMO) Kerr effect measurements on Bi substituted yttrium iron garnet (BYIG) films yield dynamic magnetization response data with many fascinating features [1, 2]. One such feature involves the frequency response which results from the fast Fourier transform (FFT) of the dynamic time response. These power spectra show numerous peaks which shift with the in-plane field. Most of these peak frequency vs. field curves fall close to the dispersion curves expected for the uniform mode ferromagnetic resonance (FMR) and various standing spin wave (SW) resonance modes. Two of the curves, however, fall *below* the FMR dispersion. This work is concerned with a simple exchange surface (ES) mode analysis and fits of ES dispersion curves to the below FMR data and is still in progress.

The analysis was based on the simple surface pinning condition,

$$\left.\frac{\partial m}{\partial n}\right|_{\text{surf}} + \left.\frac{K_s}{A} m\right|_{\text{surf}} = 0\,, \tag{1}$$

and a dynamic response profile across the film of the form $m_k(x) = a\cos(kx) + b\sin(kx)$. In these equations, m denotes the dynamic magnetization, $\partial/\partial n = \pm\partial/\partial x$ for $x > 0$ and $x < 0$, respectively, where x denotes the coordinate perpendicular to the film plane, K_s is a surface anisotropy energy parameter, and A is an exchange parameter. The boundary value analysis for a film of thickness L yields a working equation for the k-values in $m_k(x)$ which is of the form

$$\frac{2\beta\pi z}{(\pi z)^2 - \beta^2} = \tan(\pi z)\,. \tag{2}$$

Here, $\beta = K_s L/A$ and $z = kL/\pi$ define a reduced surface anisotropy parameter and a reduced wave number, respectively. Schematic results for the modes which result from such an analysis and important references are given in [3]. Solutions to Eq. (2) for real k yield the usual SW modes. For K_s and β equal to zero, one obtains solutions at $z = 0,1,2,3,\ldots$ which correspond to the uniform mode and higher order spin wave modes which are unpinned at the film surfaces. In the limit of very large positive or negative K_s and β, the solutions are at $z = 0,1,2,3,\ldots$ and correspond to pinned spin wave modes. In both cases, the nonzero integer z-values correspond to the number of standing wave half wavelengths across the film cross section. Intermediate K_s values yield real z-solutions which range between these limits. The corresponding k-values translate into mode frequencies through the applicable spin wave dispersion relation,

$$\omega_k = |\gamma|\left[(H + Dk^2)(H + Dk^2 + 4\pi M)\right]^{1/2}, \tag{3}$$

where ω_k is the mode frequency, $|\gamma|$ is the absolute value of the gyromagnetic ratio, H is the in-plane static magnetic field, D is an exchange stiffness parameter defined by $D = 2A/M$, and $4\pi M$ is the saturation induction.

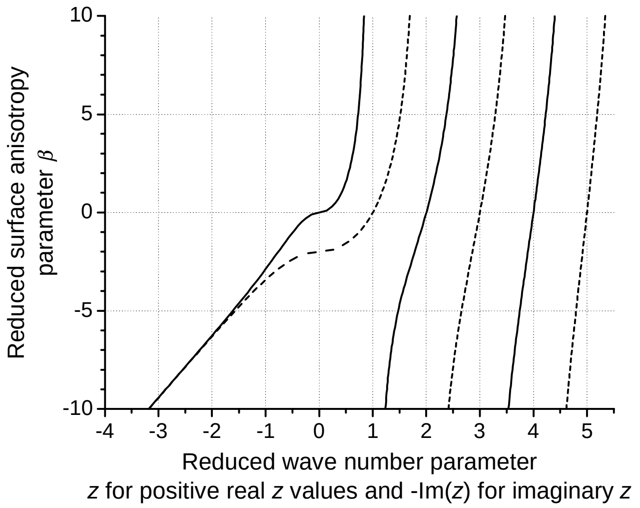

Fig. 1: Standing spin wave and exchange surface mode solutions for reduced wave number z as a function of a reduced surface anisotropy parameter β for the simple pinning model discussed in the text.

Negative K_s, and the resulting negative β in Eq. (2), give additional solutions with imaginary z. The corresponding imaginary k values yield frequencies from Eq. (3) which fall *below* the FMR dispersion curve. These modes may be termed exchange surface (ES) modes. For $0 > \beta > -2$, there is only one ES mode solution and for $-2 > \beta > -\infty$, there are two such solutions. Figure 1 shows the various z vs. β solutions from Eq. (2) for $+10 > \beta > -10$. The horizontal axis shows the actual z-values for positive real z and $-\mathrm{Im}(z)$ for the imaginary z-solutions which occur for $\beta < 0$. The change in the positive z-solutions with β correspond to the FMR and standing spin wave modes discussed above for the case of pinned or partially pinned spins. The imaginary z solutions for negative β correspond to the ES modes. Note that the two ES mode branches come very close together for $\beta < -5$.

The (a) and (b) graphs in Fig. 2 show the mode frequencies vs. field from representative TIMO BYIG data from [1], as presented in the preceding Chapter 6.5. The field H was in-plane. The solid lines in (a) correspond to calculated curves for unpinned surface spins, and $k_n = n\pi / L$ $(n = 0, 1, 2, \ldots)$. Note that crystalline anisotropy is not considered. The solid lines in (b) correspond to the z- and k-values from Fig. 1 at $\beta = -5.195$. This β-value corresponds to $K_s = 0.013\,\mathrm{erg/cm^2}$. The solid curves were obtained for typical BYIG values of 2.8 MHz/Oe, $5.4\times10^{-9}\,\mathrm{Oe\cdot cm^2/rad^2}$, and 1750 G for $|\gamma|$, D, and $4\pi M$, respectively. Except for the lowest two experimental branches, the solid curves in (a) match the data reasonably well. The FMR or $k = 0$ curve matches the triangle data almost perfectly. For (b), the two nearly degenerate surface mode curves ES1 and ES2 thread the two lowest branches from the data and support the hypothesis that these branches represent surface modes. Because of the large value of β needed to match the general trend of the ES mode curves to the data, the curves are too close together to account for the two branches found experimentally. The remaining SW1, SW2, … curves in (b) give no reasonable match to the other data.

The above results show that a simple ES mode analysis based on the simplest possible pinning model with a reasonable value of K_s can qualitatively account for the below FMR modes observed experimentally. The fits cannot match both the size of the ES mode shift below the FMR response and the two modes shown by the data. The fits also cannot give a match to the higher frequency modes which are found experimentally. The best match to these modes appears to come from a model with completely unpinned surface spins. Equation (1), however, does not

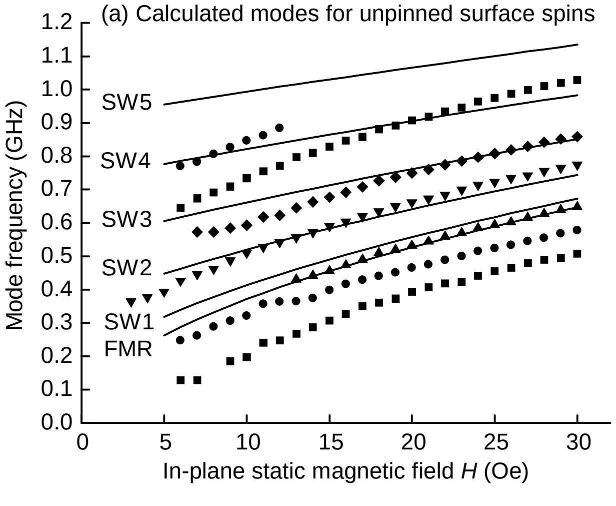

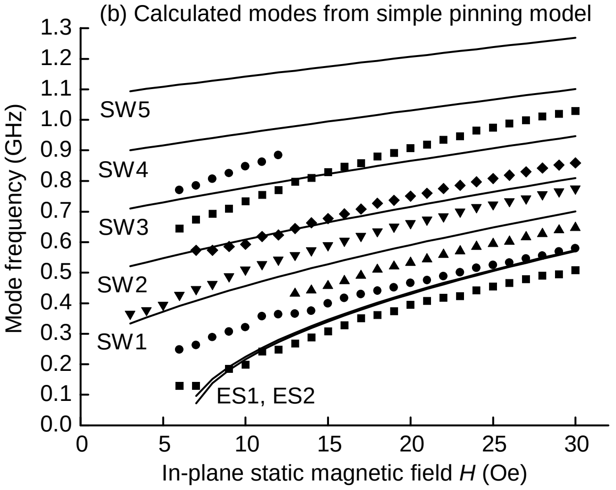

Fig. 2: The solid points in (a) and (b) show experimental data on mode frequency vs. in-plane magnetic field H from Ref. [2]. The solid lines show fits to the data for (a) a model with no pinning and (b) the simple pinning model described in the text. The FMR and ES labels denote the calculated curves for ferromagnetic resonance and the exchange surface branches, respectively, and the SW labels indicate the spin wave branches.

correspond to a true perpendicular surface anisotropy for in-plane magnetized films [4]. It is anticipated that a more rigorous ES mode analysis for a true perpendicular surface anisotropy will give a better quantitative match to all the data.

Work supported by Siemens AG, the German Ministry of Research and Technology (BMBF), and the EC-TMR program "DYNASPIN" No. FMRX-CT97-0124. C. E. Patton acknowledges financial support from the Alexander von Humboldt Foundation. This work was done during a sabbatical leave from the Department of Physics, Colorado State University, Fort Collins, Colorado 80523, USA.

References

[1] M. Bauer, R. Lopusnik, J. Fassbender, B. Hillebrands, Appl. Phys. Lett. **76**, 2758 (2000).

[2] M. Bauer, R. Lopusnik, H. Dötsch, B. A. Kalinikos, C.E. Patton, J. Fassbender, B. Hillebrands, J. Magn. Magn. Mat., in press (2000).

[3] C.E. Patton, Phys. Rep. **103** (5), 251 (1984).

[4] B.A. Kalinikos, A.N. Slavin, J. Phys. C **19**, 7013 (1986).

6.7 Numerical investigations on the switching behavior of magnetic tunnel junctions in the quasi-static and dynamic regime

J. Fassbender and M. Bauer

Magnetic tunnel junctions have attracted a lot of attention since the successful experimental realization of significant magnetoresistance at room temperature [1] because of their potential use in several technological applications, e. g., the magnetic random access memory [2]. These devices consist of a fixed hard magnetic layer and a free soft magnetic layer separated by a tunnel barrier. The free layer exhibits two easy magnetization directions which are parallel and antiparallel to the magnetization direction of the fixed layer, representing a logical bit. The stored information can be read out by a simple resistance measurement. The most important technological problems are the stray field of the hard magnetic layer and the “orange-peel” coupling caused by interface roughness between the two magnetic layers [3]. Both mechanisms act as an additional static field on the soft magnetic layer and thereby shift its astroid curve [4, 5]. This especially becomes important when the access time reaches into a time regime which can no longer be considered as quasi-static.

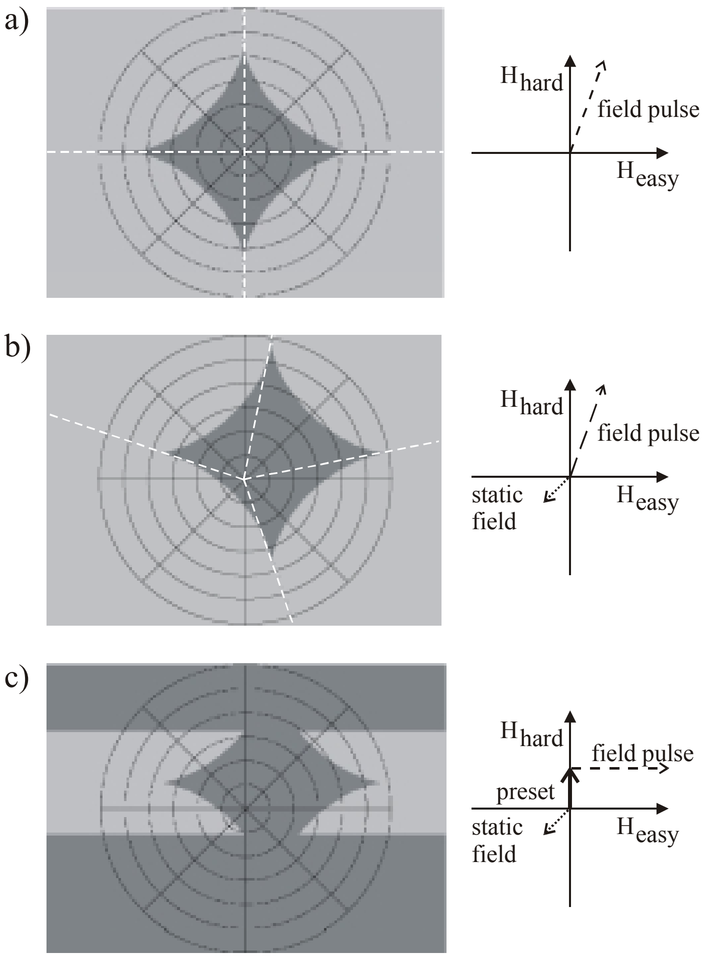

Fig. 1: Results of the numerical investigations based on the Landau-Lifshitz-Gilbert model in the quasi-static regime. Light (dark) gray corresponds to a parameter set which does (do not) lead to a switching event. In a) the well known astroid for a thin film with an uniaxial in-plane anisotropy is shown. In b) an additional static field is assumed. The dashed lines indicate the asymptotes. In c) the same astroid is shown but for the common experimental conditions, i. e., a constant preset field is applied along the hard axis and hereafter an easy axis field sweep is performed. The increment between succeeding circles is 10 Oe. On the right hand side the corresponding geometries are shown schematically.

Numerical investigations for these special cases are performed based on the Landau-Lifshitz-Gilbert equation. The saturation magnetization and magnetic damping of permalloy ($4\pi M_s = 10.8$ kG, $\alpha = 0.008$) and a uniaxial anisotropy field of 45 Oe are used for the calculation of the free layer. The pinned magnetic layer is assumed to have a fixed magnetization direction, i. e., an infinite coercive field, and acts only via a static field on the free layer. The magnetization reversal of the free layer is considered only. Prior to the magnetic field pulse the magnetization was aligned to one of the easy magnetization directions, i. e., for the simple case without additional field either along the –x or +x-direction. Then the dynamic evolution of the magnetization is calculated until the magnetization converges into an equilibrium position. A modified presentation for astroid curves is used [6]: The circular coordinate system indicates the direction and strength of the field pulse. The strength is zero at the center, and its increment is 10 Oe between two circles. The direction from the center indicates the direction of the pulse field. If the magnetization of the free layer has switched, the corresponding pixel is displayed in light gray. If for both (none) initial magnetization directions of the free layer switching occurs the corresponding pixel is white (dark gray).

The results for field pulses in the quasi-static regime are displayed in Fig. 1. A field pulse of 10 ns is used. Throughout this report the pulse rise time, the pulse duration and the pulse fall time are set to the same value. In a) and b) the results are obtained by applying a field pulse starting from zero applied field in the direction under investigation (cf. sketches on the right hand side). In a) the well known Stoner astroid [7] for a film with only uniaxial and shape anisotropy is shown. In b) an additional static field of 15 Oe oriented in-plane in the middle between the easy and hard axes originating from the hard magnetic layer is assumed. No other cou-

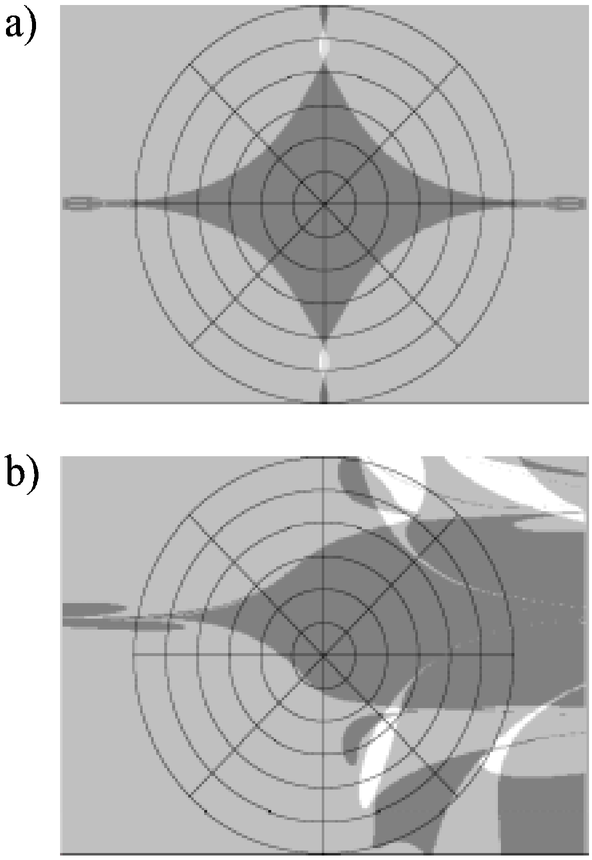

Fig. 2: Results of the numerical investigations based on the Landau-Lifshitz-Gilbert model in the dynamic regime. Light (dark) gray corresponds to a parameter set which do (do not) lead to a switching event. For a parameter set displayed in white the magnetization switches in any case irrespective of the initial magnetization direction. a) and b) correspond to the respective images of Fig. 1. For the calculation a field pulse of 1.2 ns is used. The increment between succeeding circles is 10 Oe.

pling mechanism between both magnetic layers is considered. A corresponding shift of the astroid by the same amount in the opposite direction is observed consistent with other studies [8]. Although the shape of the astroid remains the asymptotes are modified. This can be explained by calculating the magnetization direction in the ground state prior to the application of the magnetic field pulse. Due to the additional field the magnetization direction deviates from the *x*-axis. The easy axis asymptotes are antiparallel to these directions since no torque acts on the magnetization. Also the hard axis asymptotes are deformed.

In order to determine astroid curves experimentally often a different procedure is used. A static preset field is applied along the hard axis followed by an easy axis field pulse (cf. sketch on the right hand side of Fig. 1 c). In the case of the classical Stoner astroid (Fig. 1 a) both methods lead to the same results. In contrast, if an additional static field is assumed, both methods lead to different results (see Fig. 1 c). Is a preset field chosen larger than the value defined by the intersection of the shifted astroid with the abscissa an irreversible change of the magnetization direction occurs. Hereafter, upon an easy axis field pulse, the magnetization direction remains constant. Therefore the astroid can only be investigated between those limits. Sometimes a rotation of the astroid is experimentally observed [5]. This can be attributed to a misalignment of the pulsed magnetic fields with respect to the easy magnetization directions of the magnetic free layer.

Finally, we will address the additional problems arising when leaving the quasi-static limit and consider dynamic magnetic field pulses. It was demonstrated previously [6] that the magnetization dynamics can be considered as quasi-static down to pulse durations of about 2 ns. Figure 2 shows the results for a field pulse of 1.2 ns. Figure 2 a) and b) correspond to the respective images of Fig. 1. In the case of a film with only uniaxial and shape anisotropy the astroid is quite insensitive to the pulse duration (cf. Figs. 1 a and 2 a). In contrast, if an additional static field is assumed, the switching behavior is completely different (see Fig. 2 b). On the right hand side in a large angular range no switching can be achieved. Thus these elements cannot be used for ultrafast devices, i. e., when the magnetization precession cannot be neglected. In all circumstances residual static fields have to be suppressed.

Work supported by Siemens AG, the German Ministry of Research and Technology (BMBF), and the EC-TMR program "DYNASPIN" No. FMRX-CT97-0124.

References

[1] J.S. Moodera, L.R. Kinder, T.M. Wong, R. Meservey, Phys. Rev. Lett. **74**, 3273 (1995).

[2] S.S.P. Parkin, K.P. Roche, M.G. Samant, P.M. Rice, R.B. Beyers, R.E. Scheuerlein, E.J. O'Sullivan, S.L. Brown, J. Bucchigano, D.W. Abraham, Y. Lu, M. Rooks, P.L. Trouilloud, R.A. Wanner, W.J. Gallagher, J. Appl. Phys. **85**, 5828 (1999).

[3] L. Néel, Comptes Rendus Acad. Sci. **255**, 1676 (1962).

[4] Yu Lu, P.L. Trouilloud, D.W. Abraham, R. Koch, J. Slonczewski, S. Brown, J. Bucchignano, E.J. O'Sullivan, R.A. Wanner, W.J. Gallagher, S.S.P. Parkin, J. Appl. Phys. **85**, 5267 (1999).

[5] A. Anguelouch, B.D. Schrag, G. Xiao, Yu Lu, P.L. Trouilloud, R.A. Wanner, W.J. Gallagher, S.S.P. Parkin, Appl. Phys. Lett. **76**, 622 (2000).

[6] M. Bauer, J. Fassbender, B. Hillebrands, R.L. Stamps, Phys. Rev. B **61**, 3410 (2000).

[7] E.C. Stoner, E.P. Wohlfarth, Philos. Trans. R. Soc. London, Ser. A **240**, 599 (1948).

[8] H. Xi, R.M. White, J. Appl. Phys. **86**, 5169 (1999).

C. Epitaxial Growth

6.8 Magnetic in-plane anisotropy of epitaxially grown Fe-films on vicinal Ag(001) and Au(001) with different miscut orientations

M. Rickart, A.R. Frank, J. Jorzick, Ch. Krämer, S.O. Demokritov, and B. Hillebrands[1]

The influence of atomic steps at the interface on magnetic anisotropies is an attractive topic in recent research. Step induced anisotropy contributions appear because of the broken translational invariance of the electronic structure perpendicular to the steps. Additionally, lattice deformations at the steps cause elastic stress introducing a magnetoelastic contribution to the anisotropy. In principal, via the vicinal miscut, the mean step density can be chosen and thus the magnetic properties changed in a controlled way. In this contribution we report on the anisotropy of Fe films grown on isolating and semiconducting vicinal substrates. The use of such materials instead of single metallic crystals is important because of the technical relevance for magneto-transport studies.

The samples were prepared on vicinal GaAs(001) or MgO(001) substrates using a molecular beam epitaxy UHV system with a base pressure less than $5 \cdot 10^{-10}$ mbar. *In-situ* characterization was performed by LEED and RHEED, and chemical analysis by Auger electron spectroscopy. Scanning tunneling microscopy (STM) was applied for topographical studies of the grown films surfaces. In addition, *ex-situ* x-ray diffraction measurements were performed.

Vicinal to (001) GaAs wafers with various miscut orientations along the [100] and the [110] directions with *fcc* Ag buffers were used as substrates for preparation of *bcc* Fe films. The chemical cleaning procedure and the growth of the Ag and Fe films is described elsewhere [1].

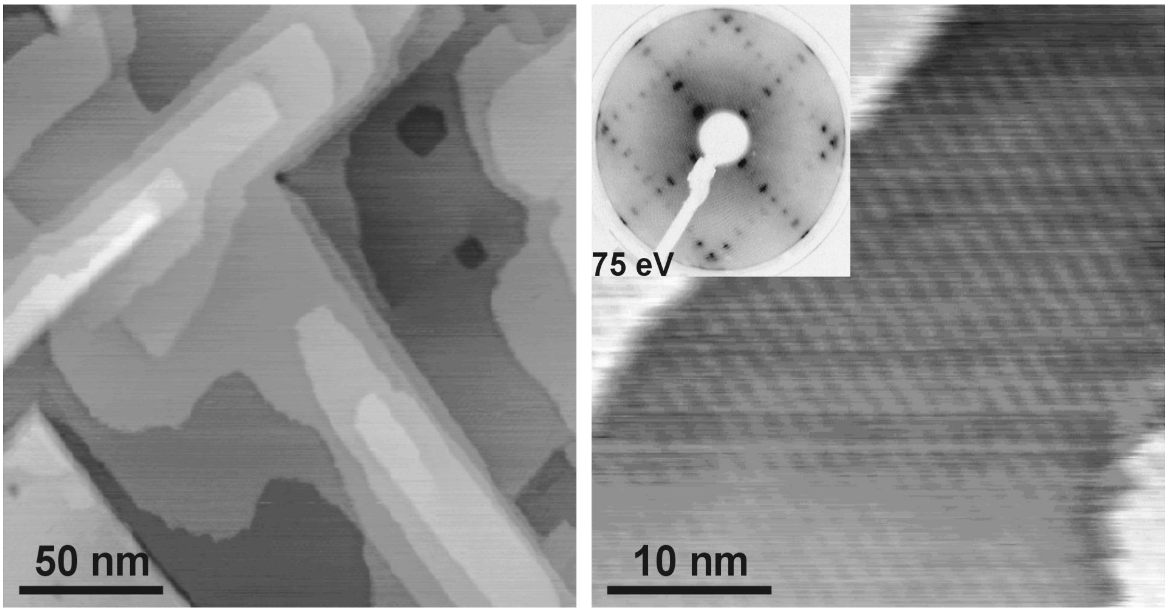

Fig. 1: Scanning tunneling microscope images of a 5×20 reconstructed Au surface. The inset shows the corresponding LEED image. The edges of the monatomic terraces as well as the reconstruction are orientated parallel and perpendicular to the [110] direction.

---

[1] In collaboration with M. Scheib, Institut für Oberflächen- und Schichtanalytik GmbH, Universität Kaiserslautern.

Polished MgO (001) substrates with miscut orientations along the [100] and [110] axes were precleaned in isopropanol before loading them into the preparation chamber. To remove the high carbon contamination at the surface the substrate was treated with a low energy O^+-beam. A 1 nm thick Fe nucleation layer was prepared onto the substrate at a temperature of 380 K with a deposition rate of 0.01 nm/s. The 150 nm *fcc* Au buffer was prepared at the same temperature with a rate of 0.1 nm/s. Finally the buffer was annealed for one hour at 520 K to improve the crystalline quality. Figure 1 shows a scanning tunneling microscope image and the LEED diffraction patterns (inset) of a (001) oriented sample without miscut. Au forms a quasi-hexagonal 5×20 reconstruction to minimize tensile stress by misplacing some of the atoms at the surface. The reconstruction as well as the step edges of the terraces are orientated parallel or perpendicular to the [110] axis. The width of the reconstruction stripes has been determined to be 0.149 nm. A further discussion of the Au reconstruction can be found in [2, 3].

The preparation of the vicinal to (001) samples is performed in the same manner. In contrast to the vicinal Ag buffer layers on GaAs, where additional LEED spots were found due to a periodic step distribution [1], such additional LEED spots are not observed for the Au buffer layer for both miscut orientations. The mean step density is therefore determined only by the miscut angle due to the non-periodic step distribution of the Au buffer. The Fe film was deposited at 390 K with a rate of 0.01 nm/s. An STM image of such a film is shown in Fig. 2. The Fe islands grow along a preferred orientation introduced by the surface reconstruction and the monoatomic steps of the Au buffer layer. AES analysis shows an intermixing of floating Au with Fe at the Fe surface. This is not of importance because the Fe film was covered in any case by a 4 nm Au cap layer for chemical symmetry at both sides of the magnetic layer as well as to prevent corrosion.

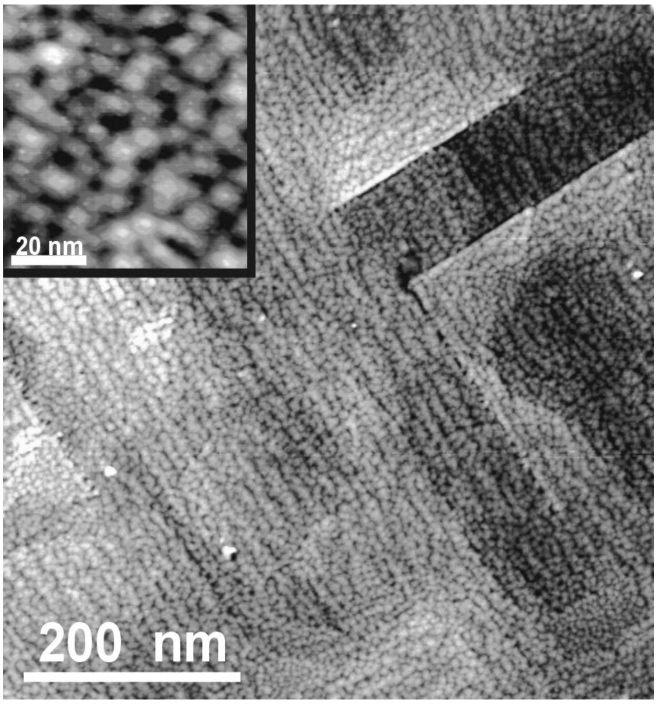

Fig. 2: STM images of a 3 nm thick Fe film prepared on a reconstructed Au surface. The inset shows an enlarged image of the island growth of Fe. The islands grow along the [110] direction.

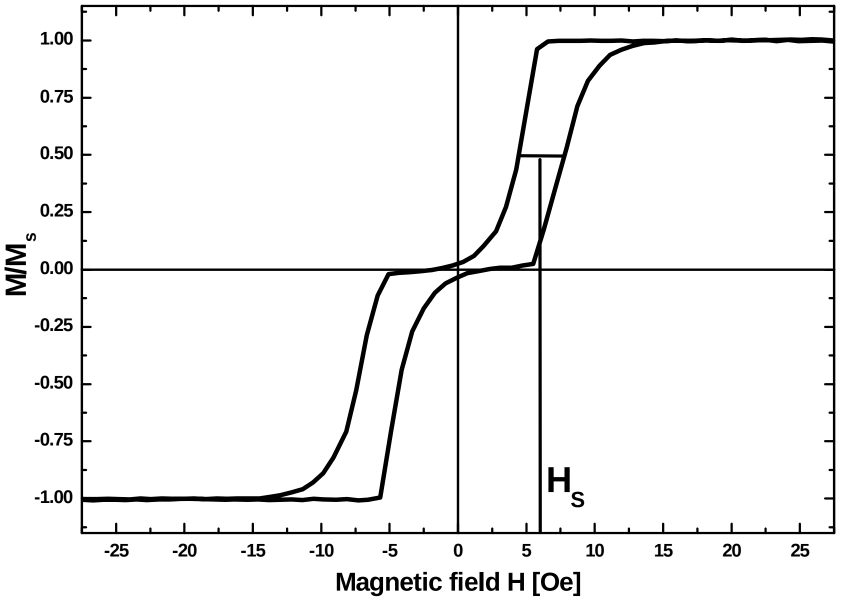

Fig. 3: Magnetization curve showing two steps of a 100 nm thick Fe vicinal film with the miscut angle of 7° along the $[10n]_{Fe}$ direction. The field is applied along the intermediate axis. The uniaxial anisotropy $K^{(2)}_{p,eff}$ is calculated using the indicated shift field H_S.

The vicinal samples have nominal miscut angles of 2°, 4°, 5°, 7° and 10° with miscut orientations along the [100] and the [110] directions. For reference, samples without miscut were prepared as well. The Fe films were grown as wedges with a continuously changing thickness d from 0.7 nm to 8 nm. In order to determine the in-plane uniaxial anisotropy contribution two experimental techniques were used. First, $M(H)$-curves were recorded using magneto-optical Kerr effect (MOKE) magnetometry. Second, the frequencies of spin waves were determined using Brillouin light scattering (BLS). In both cases the experiments were performed for different in-plane orientations of the in-plane applied field. The BLS technique has the advantage that

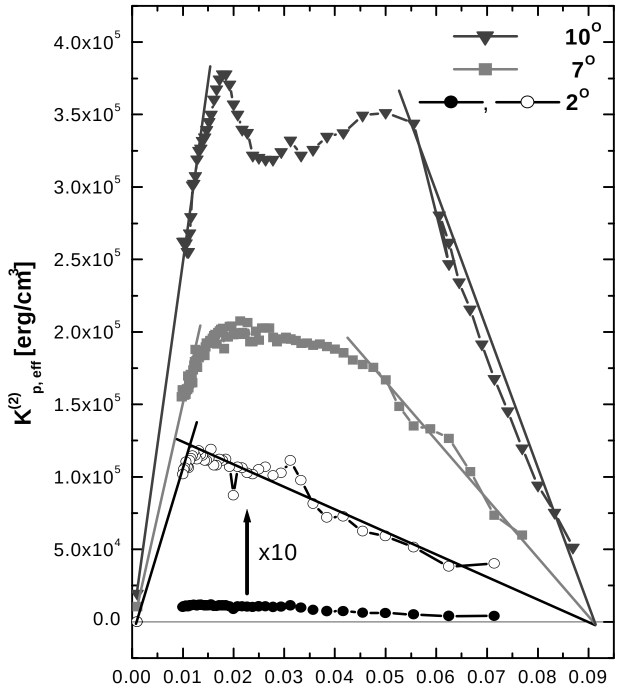

Fig. 4: Effective uniaxial in-plane anisotropy $K^{(2)}_{p,eff}$ versus the inverse Fe thickness d for different vicinal angles along the $[10n]_{Fe}$ orientation.

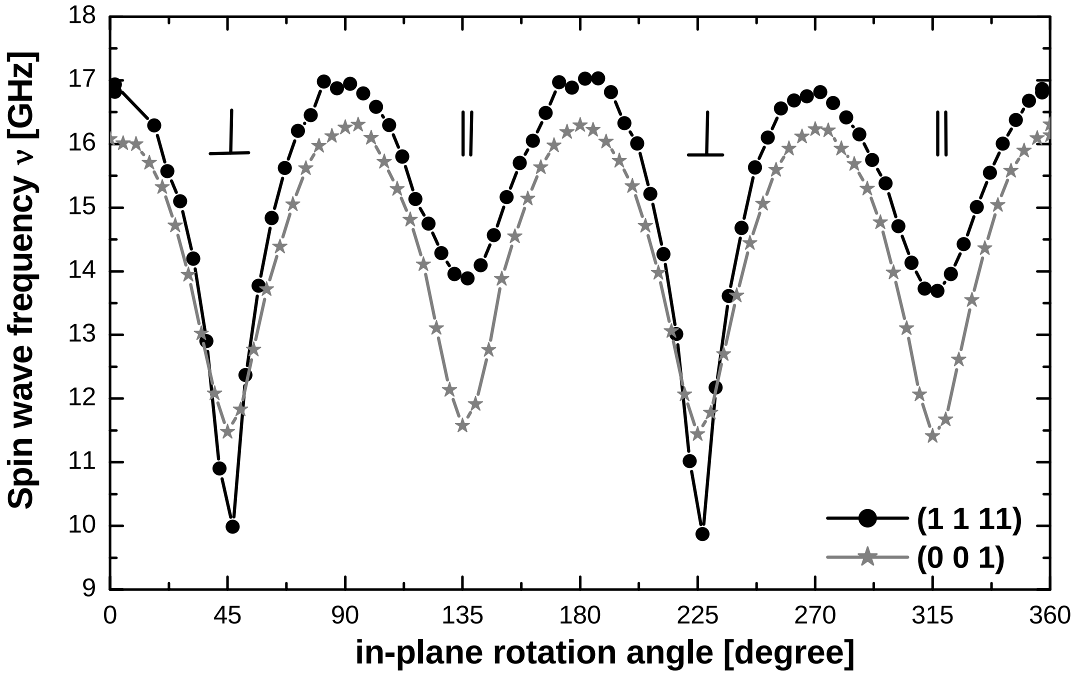

Fig. 5: Measured spin wave frequencies of 2 nm thick Fe films as a function of the azimuthal angle for a substrate without miscut and a substrate with 7° vicinal angle ((1 1 11) orientation). The external applied field was 1 kOe. The maxima in the spin wave frequencies indicate magnetic easy directions.

the out-of-plane anisotropy can be determined as well.

For the $[10n]_{\mathrm{Fe}}$ miscut orientation the equivalence between the two easy $[001]_{\mathrm{Fe}}$ and [010] axes is broken. One of these easy axes becomes the intermediate axis. Figure 3 shows a typical magnetization curve of a $[1\ 0\ 11]_{\mathrm{Fe}}$ vicinal Fe film with the field applied along the intermediate axis. In this case the $M(H)$-curve reveals a two-jump magnetization process.

The induced uniaxial in-plane anisotropy $K^{(2)}_{\mathrm{p,eff}}$ is given by $K^{(2)}_{\mathrm{p,eff}} = H_{\mathrm{S}} \cdot M_{\mathrm{S}}$, where H_{S} is the shift field as indicated in Fig. 3, and M_{S} is the saturation magnetization of the film. The measured values of the effective uniaxial in-plane anisotropy parameter are displayed in Fig. 4 as a function of the inverse thickness of the Fe film, d. For thick films the values of $K^{(2)}_{\mathrm{p,eff}}$ are small in agreement with the value of the cubic anisotropy of bulk Fe. In the thin film region a clear linear dependence is seen in Fig. 4. Thus, the volume and the surface anisotropy contributions can be separated: $K^{(2)}_{\mathrm{p,eff}} = K^{(2)}_{\mathrm{p}} + 2 \cdot k^{(2)}_{\mathrm{p}}/d$. A fit in this region yields a change in sign of $K^{(2)}_{\mathrm{p,eff}}$ at $d = 1.1 \pm 0.2$ nm. This is a manifestation of a spin reorientation transition, as also observed in non-vicinal (001) Fe films. At higher thicknesses the linearity is not fulfilled, which is an indication of the onset of lattice relaxation.

Since for the $[11n]_{\mathrm{Fe}}$ miscut orientation the two easy (100) and (010) axes are equivalent, no clear two-jump $M(H)$ curves can be recorded. The interpretation of the MOKE data is not obvious. Therefore, the effective anisotropy constant $K^{(2)}_{\mathrm{p,eff}}$ for the $[11n]_{\mathrm{Fe}}$ miscut orientation was determined by means of BLS. Figure 5 shows the measured spin wave frequencies as a function of the in-plane angle of the applied field. Maxima in the spin wave frequencies correspond to easy axes. A reference, (001) oriented Fe film shows a fourfold symmetry with maxima parallel to the [100] and [010] directions. The minima in the spin wave frequencies correspond to the hard axes. The induced twofold in-plane anisotropy breaks the equivalence between the four minima. The frequency difference between the two minima is directly connected with $K^{(2)}_{\mathrm{p,eff}}$.

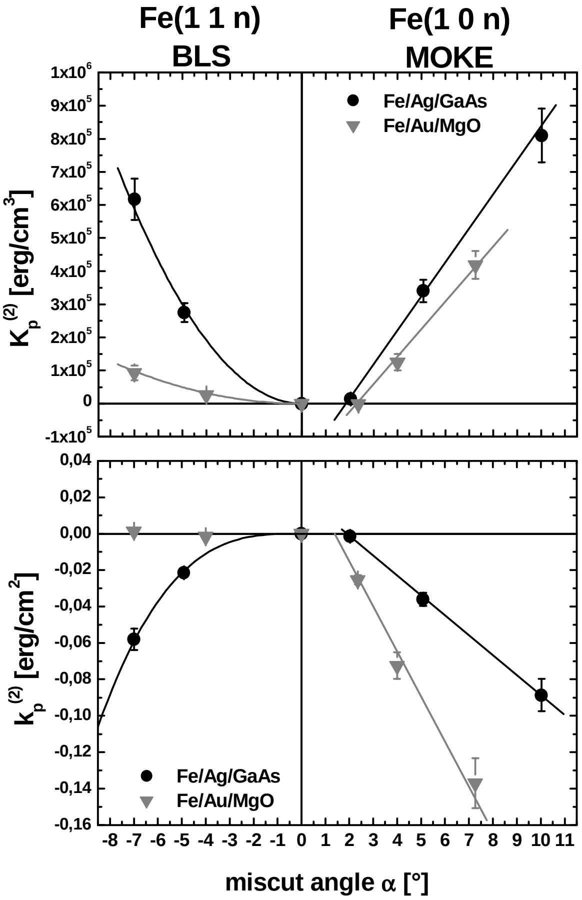

Fig. 6: Uniaxial in-plane anisotropy versus the vicinal miscut angle for two orientations of the miscut. The anisotropy constants are separated in volume ($K^{(2)}_p$) and surface ($k^{(2)}_p$) contributions. On the left hand side the measurements obtained by BLS are displayed, on the right hand side the results obtained by MOKE.

The fitted values of the anisotropy constants $K^{(2)}_p$ and $k^{(2)}_p$ for different values of the miscut angle and the miscut orientation are displayed in Fig. 6. The left panels present the data collected on $[11n]_{Fe}$ oriented samples, while the right panels correspond to the $[10n]_{Fe}$ orientation. For the $[11n]_{Fe}$ orientated films a quadratic dependence of $K^{(2)}_p$ and $k^{(2)}_p$ on the vicinal angle is clearly seen for the sample prepared on Ag as well as on Au buffers, although $k^{(2)}_p$ for Fe/Au is very small. This is in agreement with experimental data and the model published in [4]. However, for the $[10n]_{Fe}$ orientated films an almost linear dependence of $K^{(2)}_p$ and $k^{(2)}_p$ with a shift for both buffer layer materials, Ag and Au is observed. Due to the shift both $K^{(2)}_p$ and $k^{(2)}_p$ go to zero near the vicinal angle of 2°. Since the uniaxial anisotropy is absent for (001) Fe films (zero miscut angle), the measured dependencies can be described by a combination of a linear and quadratic terms with opposite signs.

Work supported by the Deutsche Forschungsgemeinschaft and the European Science Foundation.

References

[1] A.R. Frank, J. Jorzick, M. Rickart, M. Bauer, J. Fassbender, S.O. Demokritov, B. Hillebrands, M. Scheib, A. Keen, A. Petukhov, A. Kirilyuk, Th. Rasing, J. Appl. Phys. **87**, 6092 (2000).

[2] M.A. van Hove, R.J. Koestner, P.C. Stair, J.P. Biberian, L.L. Kesmodel, I. Bartos, G.A. Somorjai, Surf. Sci. **103**, 189 (1981).

[3] O.S. Hernan, J.M. Gallego, A.L. Vazquez de Parga, R. Miranda, Appl. Phys. **A 66**, 1117 (1998).

[4] Z.Q.Qiu, S.D. Bader, Surf. Sci **438**, 319 (1999).

6.9 Epitaxial growth of Cu(111) on MgO(001) using a Pt seed layer

T. Mewes, M. Rickart, A. Mougin, S.O. Demokritov, J. Fassbender, and B. Hillebrands

There is increasing demand for epitaxially grown metallic films on non-conducting, i.e. insolating or semiconducting substrates. One of the important issues is the fabrication of smooth epitaxial Cu films to serve as a growth template for device structures, such as, e.g., giant magnetoresistance (GMR) or tunneling magnetoresistance (TMR) devices. Cu is becoming a standard material in integrated circuits. It has the advantage of a low resistivity, which is important for minimizing heat load on the devices.

As we have shown previously it is possible to grow Cu(001) on hydrogen terminated Si(001) [1]. The rough surface of the resulting Cu film together with the limited accessible temperature range due to silicide formation are the major disadvantages of using hydrogen terminated Si(001) as a substrate. Due to the superior high temperature stability and low chemical activity we have chosen MgO(001) as a substrate. We use a new technique for decarbonation of the MgO-surface. The MgO(001) substrate was oxidized using a gas mixture of highly dissociated 40% argon and 60% oxygen ions with energies of 30 ± 3 eV, yielding a smooth and carbon free surface.

The LEED patterns of a 100 nm Cu film grown at room temperature on MgO(001) are shown in Fig. 1. The Cu [100]-direction is found to be parallel to the [100]-direction of MgO. The LEED spots are narrow compared to those of Cu(001) prepared on hydrogen terminated Si(001) [1] indicating a larger lateral correlation length. However the RHEED patterns (not shown) of these films exhibit spots typical for three dimensional island growth. This is caused by the large lattice mismatch between MgO(001) and fcc Cu(001) of approximately 14% and the poor sticking coefficient [2, 3, 4] leading to the Volmer-Weber growth mode [3].

Fcc Pt has a lattice spacing of 0.3924 nm, which is between those of MgO and fcc Cu. In order to improve the Cu layer growth we tested the applicability of a Pt seed layer. Due to a better accommodation of the lattice misfit one should expect a better growth of Cu.

The deposition of a 5 nm thick Pt film at 725 K on MgO(001) results in LEED patterns (not shown) with a large background and a pseudo 12-fold symmetry. Also the LEED patterns of the following Cu layer exhibit this pseudo 12-fold symmetry, as displayed in Fig. 2. Such a LEED

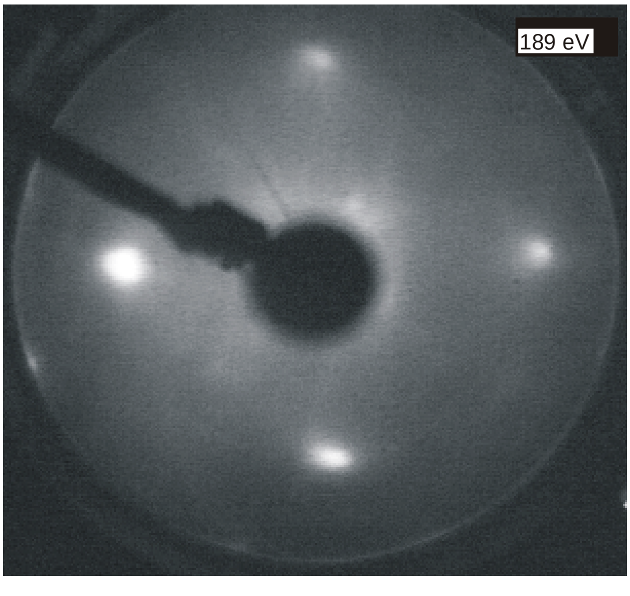

Fig. 1: LEED pattern of a 100 nm thick Cu films, grown on MgO(001). The primary energy is 189 eV.

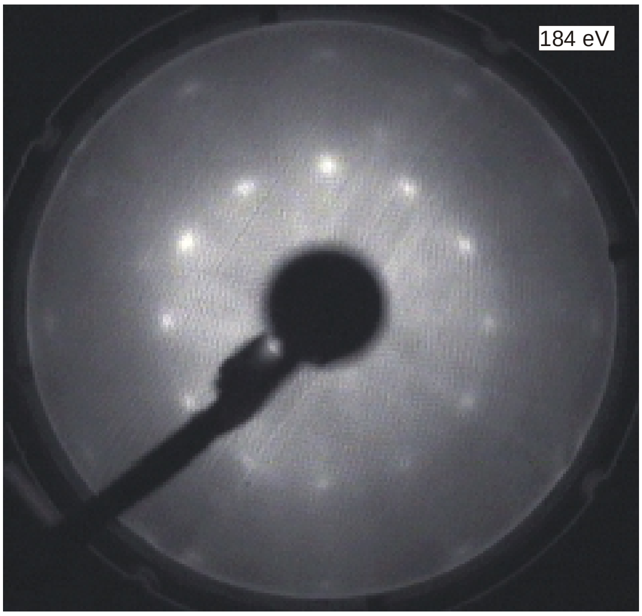

Fig. 2: LEED pattern of a 100 nm thick Cu film, grown on MgO(001)/Pt(5 nm). The primary electron energy is 184 eV.

pattern can be understood assuming a (111)-orientation of the Pt seed layer, which is proven by XRD measurements (see discussion below).

The LEED patterns of an ideal (111)-surface display a three-fold symmetry (see Fig. 3 a)). However due to the four-fold symmetry of the MgO substrate there are four equivalent orientations for a stacking sequence ABCA as illustrated in Fig. 3 a) – d). Four domains with different orientations of the stacking sequences are formed. Averaging across the electron spot area on the surface leads to a superposition of the four possible LEED patterns as displayed in Fig. 3 e). Note that stacking faults will produce the same LEED patterns but with a rotation of 180°. Since the corresponding spots are already present in one of the four orientations described above no additional spots arise. Figure 4 shows a specular $\theta/2\theta$ x-ray diffraction scan of a MgO(001)/Pt/Cu sample. The corresponding diffraction peaks are identified in the Figure. The Pt(111), Pt(222), Cu(111), and Cu(222) peaks are well observed confirming the (111)-orientation of both the Pt and Cu layers. This corroborates a (111)-oriented Pt buffer layer used for the interpretation of the found pseudo 12-fold LEED patterns.

Thus using Pt as a seed layer for the growth of Cu on MgO results in a (111) oriented Cu film with four domains of different orientation, due to the four fold symmetry of the MgO substrate. This leads to a pseudo 12-fold symmetry of the LEED patterns of Cu grown on MgO/Pt. Thegrowth of (001)-oriented smooth Cu films by using an additional Fe seed layer is subject of Chapter 610.

T. Mewes would like to gratefully acknowledge support by the Studienstiftung des deutschen Volkes.

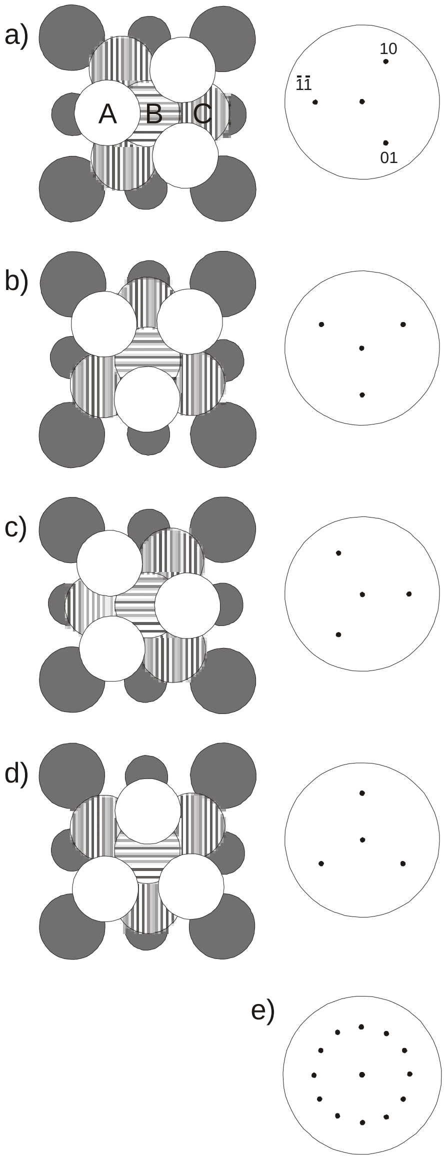

Fig. 3: (a–d) Four equivalent orientations of the ABCA stacking sequence of fcc Pt(111) on the MgO(001) substrate (dark spheres) with the corresponding ideal LEED patterns. e) Superposition of the LEED patterns shown in a) – d) due to averaging over all four orientations.

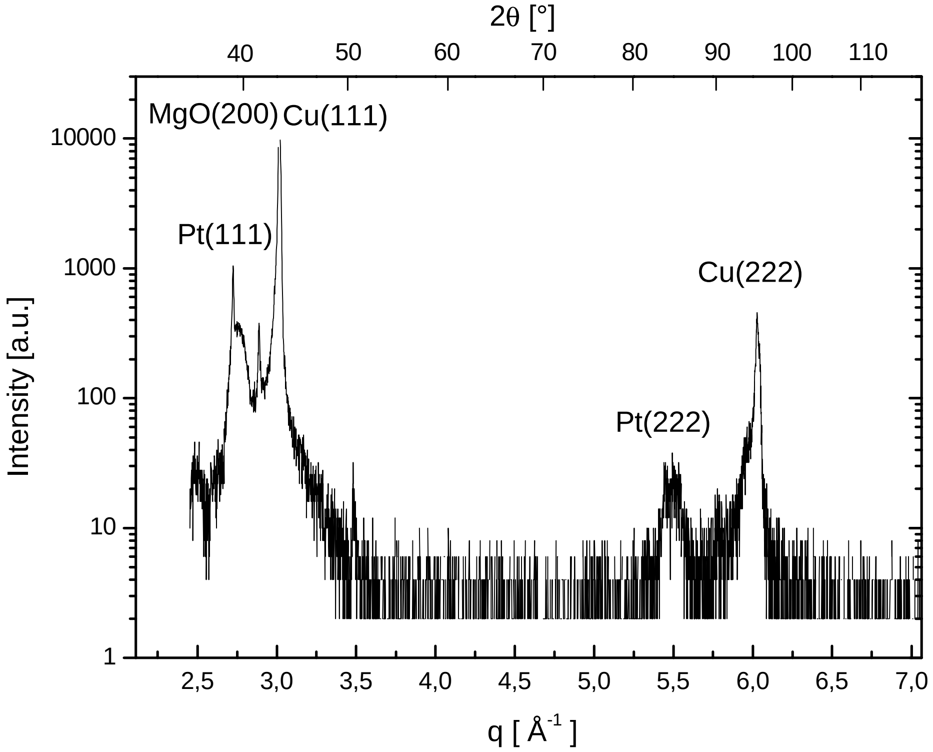

Fig. 4: Specular θ/2θ x-ray diffraction scan of the MgO(001)/Pt/Cu layered system obtained with a primary wavelength of λ = 0.15405 nm.

References

[1] M. Rickart, T. Mewes, B. Roos, S.O. Demokritov, B. Hillebrands, Annual Report, 33 (1998).
[2] M.-C. Wu, W.S. Oh, D.W. Goodman, Surf. Sci. **330**, 61 (1995).
[3] J.B. Zhou, T. Gustafsson, Surf. Sci. **375**, 221 (1997).
[4] N. Lopez, F. Illas, N. Rösch, G. Pacchioni, J. Chem. Phys. **110**, 4873 (1999).

6.10 Improved growth of smooth Cu(001) films on MgO(001)

T. Mewes, M. Rickart, A. Mougin, S.O. Demokritov, J. Fassbender, and B. Hillebrands

Smooth Cu(001) films can be grown on MgO(001) by using the growth recipe described in the preceding Section and adding an additional Fe(001) seed layer between the MgO substrate and the Pt layer. The Fe layer is used to induce the (001) growth orientation of the Pt layer [1]. The subsequent Cu layer will thus also be (001)-oriented. The Fe and Pt layers were deposited at 725K. The following Cu layer was then prepared at room temperature.

The introduction of the Fe layer completely changes the growth mode of Pt compared to the growth of Pt directly on MgO(001) (see Chapter 6.9). This can be clearly seen in the LEED patterns, presented in Fig. 1 a). The LEED patterns obey a four-fold symmetry indicating a growth of the Pt(001) orientation. The [100]-direction of Pt is parallel to the [100]-direction of MgO(001). The LEED patterns are reminiscent of the well known hexagonal ($5\times n$) reconstruction of clean Pt(001) single crystal surfaces [2, 3]. Figure 1 b) shows a STM image of the same sample. The RMS roughness is 0.2 nm and the correlation length is ≈ 10 nm. The inset of Fig. 1 b) shows a 30 nm × 30 nm scan of the same surface. Island rows with a typical dimension of a few nm appear. They can be attributed to the reconstruction observed in the LEED patterns. Due to the surface roughness the reconstruction itself cannot be observed in the STM image.

A specular $\theta/2\theta$ x-ray scan for the whole system MgO(001)/Fe/Pt/Cu clearly demonstrates the (001)-orientation of both the Pt and Cu layers. No indication of (111)-oriented material is found. Accordingly, the LEED patterns of the Cu surface consist of sharp spots, see Fig. 2 a). For comparison in Fig. 2 b) the LEED pattern of a Cu layer deposited directly on MgO is shown. $I(V)$-measurements (not shown) identify these spots as being those of Cu(001). Thus Cu(001) grows with the [100]-direction parallel to the [100]-direction of the MgO-substrate.

To summarize, the orientation of each layer in the layered system is as follows: The [100]-direction of the Fe seed layer is rotated in-plane by 45° with respect to that of MgO. Pt subsequently exhibits a second in-plane rotation of 45° in order to reduce the lattice mismatch between

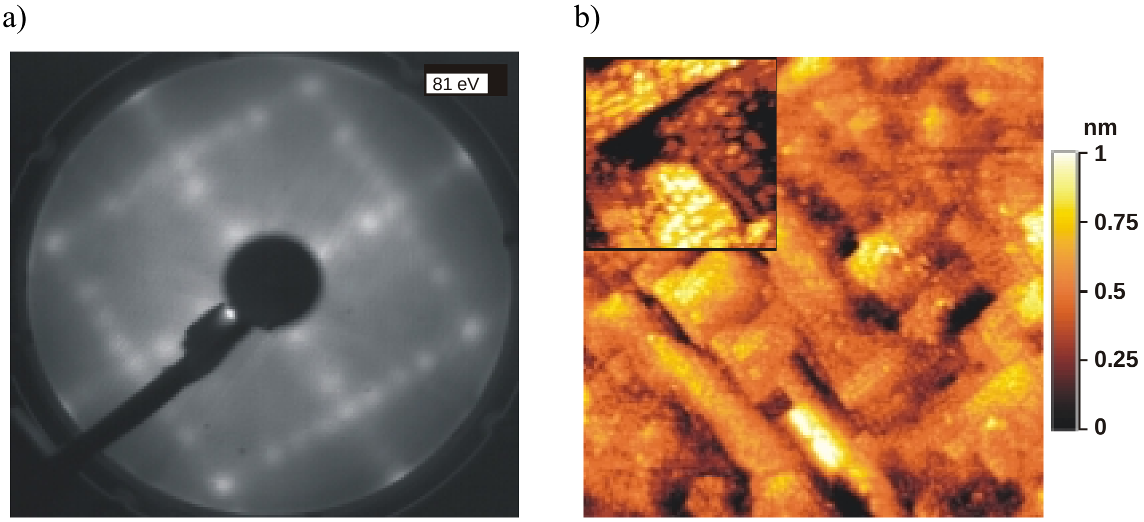

Fig. 1: a) Leed pattern of a MgO(001)/Fe(0.5 nm)/Pt(5 nm) sample at a primary energy of 81 eV. b) STM image of the same sample. The scan area is 0.2 µm × 0.2 µm, and the full height scale is 1 nm. The inset shows a 30 nm × 30 nm scan of the same surface.

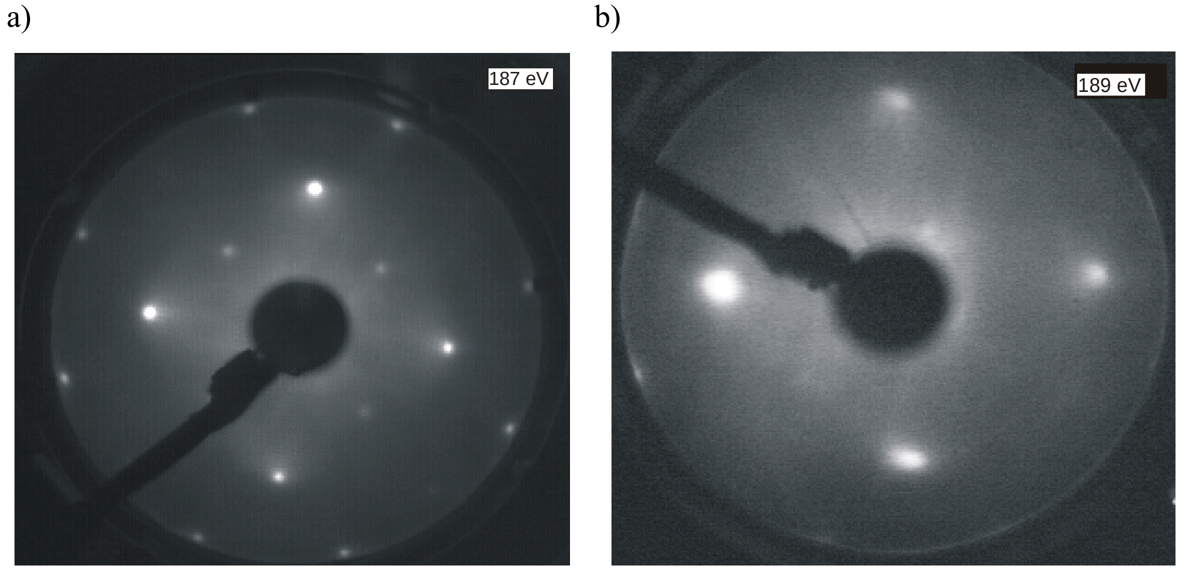

Fig. 2: LEED patterns of a 100 nm thick Cu film grown on a) MgO(001)/Fe/Pt b) directly on MgO(001). The primary energy was 187 eV and 189eV.

Fe and Pt to approximately 3% explaining the observed parallel orientation of the [100]-directions of MgO and Pt. Cu(001) then grows in the same orientation as Pt(001) in agreement with the results obtained for growth on Pt(001) single crystals [4].

In order to investigate the mosaicity of the prepared films x-ray diffraction rocking curve measurements have been performed for the specular Cu(002) diffraction peak. The obtained rocking curves of the MgO(001)/Cu and MgO(001)/Fe/Pt/Cu systems are shown in Fig. 3. Without a seed layer a rather broad peak with a full width at half maximum (FWHM) of 1.8° is observed. In contrast, the FWHM of the rocking curve of MgO(001)/Fe/Pt/Cu is as small as 0.6°. Thus, the

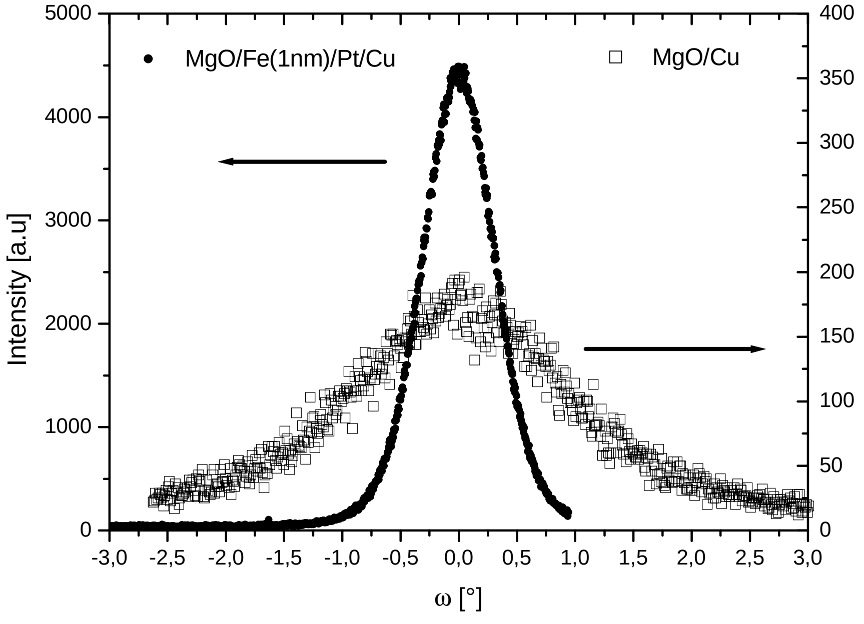

Fig. 3: Comparison between the x-ray diffraction rocking curves for MgO(001)/Cu (open symbols) and MgO(001)/Fe/Pt/Cu (full symbols) of the specular Cu(002) diffraction peak obtained for a primary wavelength of $\lambda = 0.178892$ nm. The full width at half maximum (FWHM) of the systems with (without) Fe/Pt seed layer is 0.6° (1.8°).

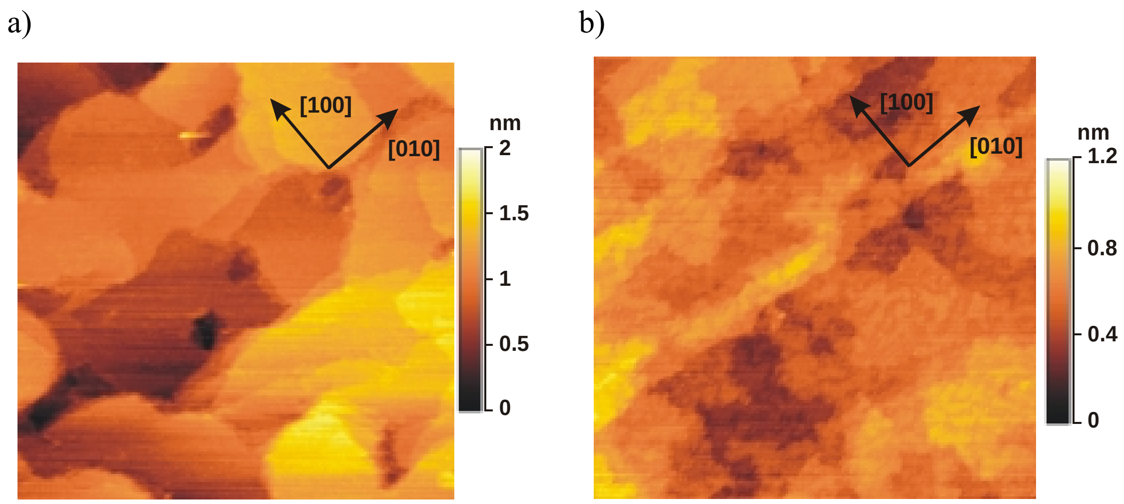

Fig. 4: STM images for the system MgO/Fe/Pt/Cu. a) as prepared, b) after a brief annealing to 920 K. In a) (b)) the full height scale is 2 nm (1.2 nm) and the RMS roughness is 0.3 nm (0.15 nm). The scan area is 0.2µm×0.2µm in both cases.

use of Fe/Pt as a seed layer results in a decrease by a factor of three of the mosaicity of the Cu layer. The thickness of the Fe seed layer (0.5 nm) has been tested to be the optimal one. The rocking curve obtained on a Cu film grown on a Fe/Pt buffer with a Fe seed layer of 1 nm (not shown) displays an increase of the FWHM to 0.8°.

The surface of the MgO(001)/Fe/Pt/Cu layered system was investigated by *in-situ* STM. The corresponding STM images are shown in Fig. 4. Large terraces with an average size of 2500 nm^2 are observed (see Fig. 4 a)). For a scan area of 0.2 µm × 0.2 µm the RMS roughness is 0.3 nm. The correlation length is of the same order as the scan width. For further reduction of the surface roughness the sample was briefly (4 min) annealed in UHV at 920 K. The corresponding STM image is shown in Fig. 4 b). The RMS roughness directly determined from a 0.2 µm × 0.2 µm scan is 0.15 nm, i.e., it is decreased by a factor of ≈ 2.

A Fe/Pt buffer deposited on a carbon free MgO surface thus provides a perfect surface for epitaxial growth of smooth Cu(001) films. Cu films prepared on this seed layer system exhibit a small surface roughness, a large lateral correlation length and a small mosaicity. An additional brief annealing to 920 K reduces the surface roughness further resulting in a very flat Cu(001) surface suitable for epitaxial growth of ultrathin fcc and bcc metallic layers.

T. Mewes would like to gratefully acknowledge support by the Studienstiftung des deutschen Volkes.

References

[1] B.M. Lairson, M.R. Visokay, R. Sinclair, S. Hagstrom, B.M. Clemens, Appl. Phys. Lett. **61**, 1390 (1992).
[2] P. Heillmann, K. Heinz, K. Müller, Surf. Sci. **83**, 487 (1979).
[3] K. Heinz, E. Lang, K. Strauss, K. Müller, Appl. Surf. Sci. **11/12**, 611 (1982).
[4] Y.S.Li, J. Quinn, H. Li, D. Tian, F. Jona, P.M Marcus, Phys. Rev. B **44**, 8261 (1991).

D. Exchange Bias Effect

6.11 Local manipulation and reversal of the exchange bias field by ion irradiation in FeNi/FeMn double layers

A. Mougin, T. Mewes, J. Fassbender, and B. Hillebrands[1]

Defects in exchange bias bilayers play a key role. In order to create artificial defects, He ion irradiation is used. We demonstrate that, depending on the ion dose and on the direction of a field applied during irradiation, the exchange bias field is either enhanced or suppressed [1] and its direction may be even reversed [2].

We chose the well known FeNi/FeMn exchange bias system. A 5 nm thick $Fe_{0.19}Ni_{0.81}$ layer (F) and a 10 nm thick $Fe_{0.5}Mn_{0.5}$ (AF) layer were grown on a thermally oxidized Si substrate with a 35 nm thick Cu buffer layer. The samples are polycrystalline with a strong (111) texture. After the deposition the samples were heated and subsequently cooled in a magnetic field $H_{\mathrm{preparation}}$ =

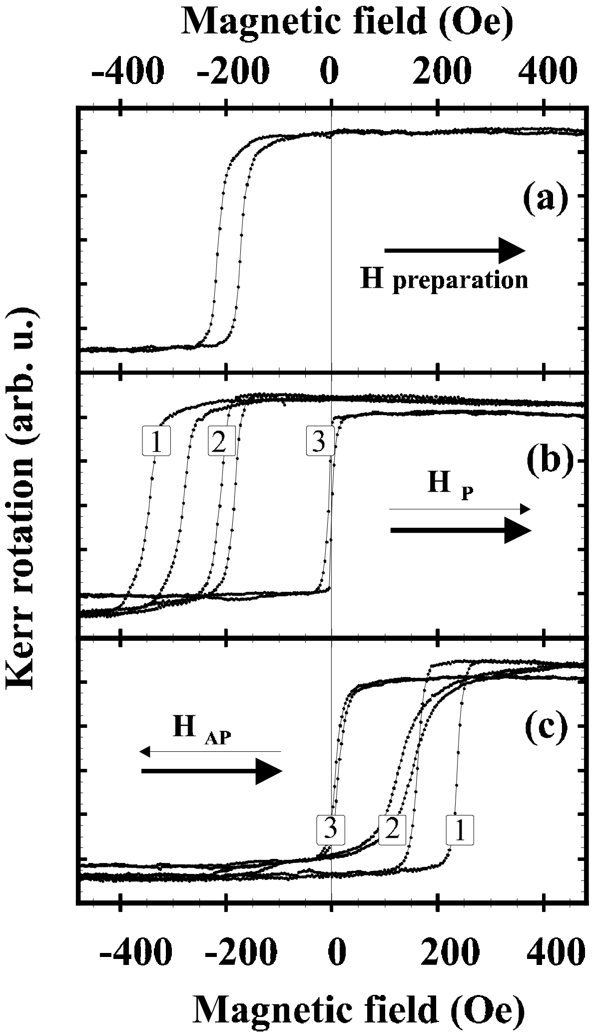

Fig. 1: In a) the hysteresis curve for a FeNi/FeMn exchange bias sample measured at room temperature prior to He irradiation is shown. Hysteresis curves after irradiation in an external field parallel H_P and antiparallel H_{AP} to the preparation field direction H_{prep} are shown in b) and c), respectively. The different numbers correspond to different ion doses: b) (H_P geometry) 1: $0.25\cdot10^{15}$ ions/cm^2, 2: $1.32\cdot10^{15}$ ions/cm^2, 3: $9.5\cdot10^{15}$ ions/cm^2, c) (H_{AP} geometry) 1: $0.25\cdot10^{15}$ ions/cm^2, 2: $0.9\cdot10^{15}$ ions/cm^2, 3: $9.5\cdot10^{15}$ ions/cm^2.

---

[1] In collaboration with M. Jung, D. Engel, A. Ehresmann, and H. Schmoranzer, Fachbereich Physik, Universität Kaiserslautern

500 Oe (indicated by a bold arrow in Fig. 1) below the Néel temperature of FeMn. An initial exchange bias field, $H_{eb,initial}$, of –190 Oe is found (see Fig. 1a). Then, the samples were irradiated with 10 keV He ions, covering the ion dose range $2\cdot10^{13} - 10^{16}$ ions/cm^2. During the ion irradiation process, an external magnetic field was applied in the film plane either parallel (H_P) or antiparallel (H_{AP}) to H_{prep}, as indicated by thin arrows in Fig. 1. When the irradiation has been performed in an external field parallel to H_{prep} (H_P case, Fig. 1b) an ion dose as small as $2.5\cdot10^{14}$ ions/cm^2 (1) leads to an enhanced shift of the hysteresis loop with respect to the initial one (cf. Fig. 1a). Further increase of the ion dose leads to a reduction (2) and finally to a full suppression (3) of the exchange bias field. When the external field is applied antiparallel to H_{prep} (H_{AP} case, Fig. 1c), the hysteresis loops are shifted to the opposite side with respect to H_{prep}. Irrespective of the sign, the overall course of the exchange bias field is similar in both irradiation configurations. The exchange bias field normalized to the field before ion irradiation, $H_{eb}/H_{eb,initial}$, is plotted as a function of ion dose in Fig. 2. Two regimes are identified in the H_P geometry: i) in the low dose regime a pronounced increase by about 75% of H_{eb} is found. ii) for larger doses ($7.5\cdot10^{14}$ ions/cm^2) the evolution is reversed and H_{eb} is reduced. In the H_{AP} geometry, upon irradiation with an ion dose of $2\cdot10^{14}$ ions/cm^2, the initial absolute value of H_{eb} is recovered with the opposite sign. A maximum of the absolute value of the exchange bias field is found for $3.5\cdot10^{14}$ ions/cm^2. A successive increase of the ion dose leads to a similar suppression of the effect as in the H_P geometry.

The impinging ions loose their energy mainly due to inelastic scattering. At the end of their trajectories, nuclear collisions of the ions cause irreversible modifications of the structural properties, which also can induce modifications of the magnetic properties [3]. Here, however, the total thickness of all layers including the cap layer is smaller than the penetration depth of the ions, and the majority of the ions is stopped deep in the substrate.We have developed a model to fit the experimental results. In the following, n_V and n_I denote the normalized densities of defects in the bulk AF layer and at the interface, respectively. If all atoms of the AF volume have been

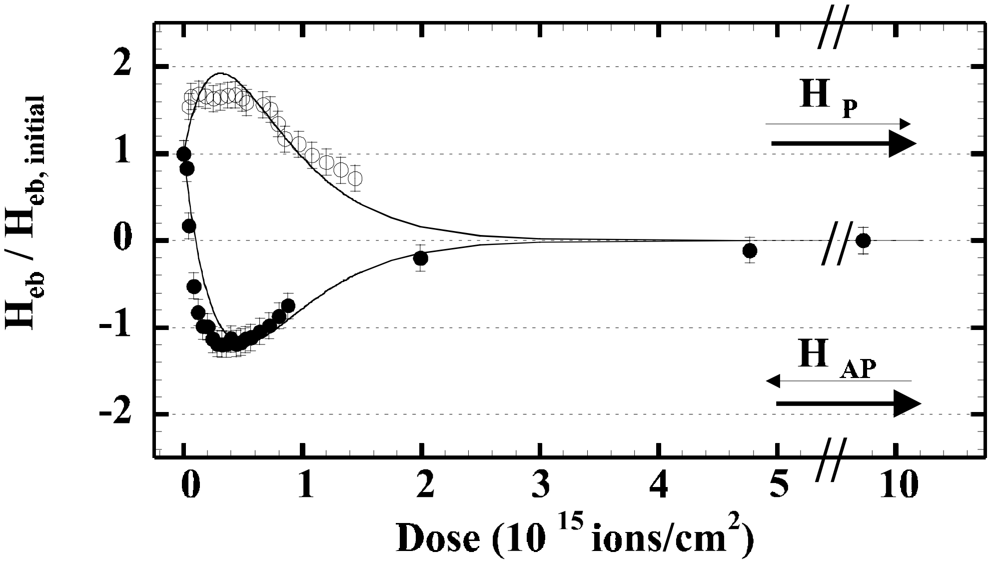

Fig. 2: Normalized exchange bias field, $H_{eb}/H_{eb,initial}$, as a function of ion dose. Open and full symbols are extracted from the hysteresis curves measured for samples irradiated in an external field parallel (H_P) and antiparallel (H_{AP}) to the preparation field, H_{prep}. The solid lines are the result of the model fit described in the text.

displaced, $n_V = 1$. The model is based on the following two assumptions: i) the magnitude of the exchange bias effect is proportional to the number of displaced atoms in the bulk of the AF layer. This is in agreement with current models of the exchange bias effect, which assume domain walls in the AF layer and predict, that H_{eb} is proportional to the number of domain walls. The domain wall number is proportional to the number of defects generating them. ii) Defects created at the interface (normalized defect density n_I) are mostly exchanges of atoms across the interface (interfacial mixing), which reduce the effective exchange coupling across the F/AF interface [1]. We model this effect by an exponential decrease of the exchange coupling as a function of n_I. Then the normalized exchange bias field can be written as:

$$\frac{H_{eb}}{H_{eb,initial}} = \left(1 \pm a n_V(N)\right) \cdot \exp\left(-b n_I(N)\right) \tag{1}$$

with N the number of impinging ions and a (b) is the efficiency of the volume (interface) defects to modify the exchange bias field magnitude. In the first factor the + (–) sign corresponds to irradiation in an applied field parallel (antiparallel) to H_{prep}. We assume that the exchange bias originates from the imbalance between different domains in the AF layer resulting in a net exchange field acting on the F layer, as commonly used. In the H_P geometry the imbalance is reinforced, whereas in the H_{AP} geometry the imbalance is progressively reversed. In the next step the corresponding normalized defect densities have to be determined. n_V is calculated solving a rate equation and in the limit $n_V \ll 1$ we obtain: $n_V \simeq pNt$ with p the probability of displacing an atom per incoming ion and per length unit calculated from TRIM simulations [4], and t is the AF layer thickness. pt is evaluated from a simple integration over the total AF thickness [4]. Since each impinging ion penetrates through the interface, the normalized interface defect density is given by $n_I(N) = \gamma N$ with γ a proportionality factor. Then, the normalized exchange bias field satisfies the equation

$$\frac{H_{eb}}{H_{eb,initial}} = \left(1 \pm aptN\right) \cdot \exp\left(-b_I N\right) \tag{2}$$

with $b_I = \gamma b$. Only two free parameters (a, b_I) are needed in a fit procedure to reproduce the two sets of data points simultaneously in the H_P and in the H_{AP} geometry. The solid lines in Fig. 2 correspond to this model with $a = 2.7$ and $b_I = 2.5$. A good agreement is found between the experimental data and the model. Results obtained after a second annealing process of the irradiated samples support the assumptions [2].

Work supported by the EC-TMR program "DYNASPIN" No. FMRX-CT97-0124.

References

[1] T. Mewes, R. Lopusnik, J. Fassbender, B. Hillebrands, M. Jung, D. Engel, A. Ehresmann, H. Schmoranzer, Appl. Phys. Lett. **76**, 1057 (2000).

[2] A. Mougin, T. Mewes, M. Jung, D. Engel, A. Ehresmann, H. Schmoranzer, J. Fassbender, B. Hillebrands, submitted to Phys. Rev. Lett.

[3] C. Chappert, H. Bernas, J. Ferré, V. Kottler, J.-P. Jamet, Y. Chen, E. Cambril, T. Devolder, F. Rousseaux, V. Mathet, H. Launois, Science **280**, 1919 (1998).

[4] SRIM 2000 code, J.F. Ziegler, J.P. Biersack, U. Littmark, "The Stopping and Range of Ions in Solids", Pergamon, New York, Oxford (1985).

6.12 Thermal behavior of the exchange bias effect in NiFe/FeMn double layers modified by He ion irradiation

S. Poppe, H. Nembach, A. Mougin, T. Mewes, J. Fassbender, and B. Hillebrands[1]

Recently, we have reported that both the exchange bias field and the coercive field in FeNi/FeMn bilayers can be reduced or enhanced by He ion irradiation in a controlled manner by adjusting the dose and the energy of the He ions, see preceding Section [1]. In this report the temperature dependence of both the bias field and the coercive field are examined.

The samples were prepared in a UHV-system with a base pressure of $5\cdot10^{-10}$ mbar. A 5 nm thick ferromagnetic (F) $Fe_{0.19}Ni_{0.81}$ layer and a 10 nm thick antiferromagnetic (AF) $Fe_{0.5}Mn_{0.5}$ layer were grown onto thermally oxidized Si substrates with a 35 nm Cu buffer layer. Finally, a 2 nm Cr layer was deposited to protect the samples from oxidation. The samples were grown at room temperature and show a strong (111) texture. After deposition, the samples were heated and subsequently cooled in an 500 Oe magnetic field below the Néel temperature to initiate the exchange bias effect.

The magnetic properties were initially investigated *ex situ* by longitudinal magneto-optical Kerr-effect (MOKE) magnetometry at room temperature. The exchange bias field and the coercive field were found to be homogeneous across each sample. The initial exchange bias field, $H_{\mathrm{eb,initial}}$, is as high as –190 Oe. This exchange bias field corresponds to an interface exchange energy of 0.08 erg/cm^2. The respective coercive field, $H_{\mathrm{c,initial}}$, is 22 Oe, which is considerably higher than typical values for single FeNi films (2 – 3 Oe). An analysis of the hysteresis curves

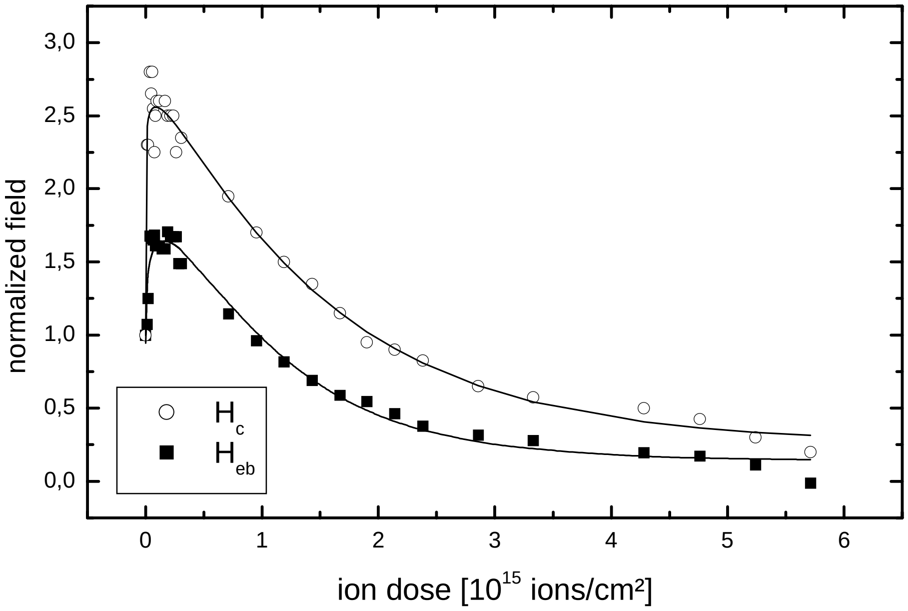

Fig. 1: Variation of the bias field ratio $H_{\mathrm{eb}}/H_{\mathrm{eb,initial}}$ (closed squares), and the coercive field ratio $H_{\mathrm{c}}/H_{\mathrm{c,initial}}$ (open circles) with the ion dose.

---

[1] In collaboration with M. Jung, D. Engel, A. Ehresmann, and H. Schmoranzer, Fachbereich Physik, Universität Kaiserslautern.

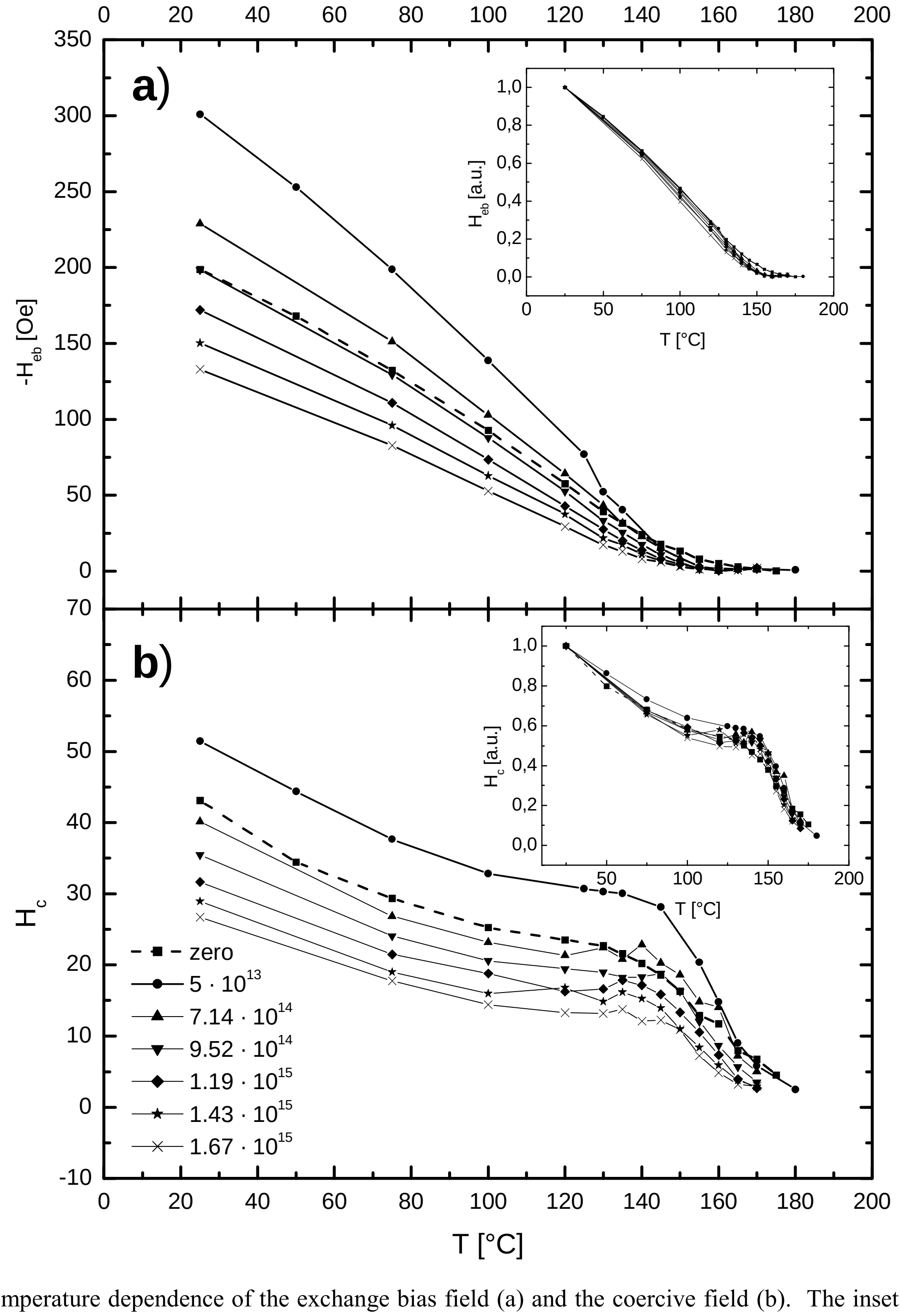

Fig. 2: Temperature dependence of the exchange bias field (a) and the coercive field (b). The insets show the same values normalized to the respective value at room temperature.

as a function of the in-plane angle of the applied field shows an unidirectional anisotropy, as expected for this system due to the exchange bias effect.

To perform the ion irradiation the samples were inserted into an ion optical bench. He ions were produced in a Penning type source and accelerated by 10 kV. Different doses on the samples were realized by adjusting the beam current (5 – 60 nA), and by varying the irradiation time (3 – 120 s). These values for current, voltage and time allows us to cover the ion dose range from

10^{13} ions/cm^2 to $6{\cdot}10^{15}$ ions/cm^2. The effect of different ion doses was studied on a single sample by irradiating different areas of the sample with different parameter sets.

Next hysteresis loops were measured with a cycle time of 40 s on the different irradiated areas by scanning the MOKE laser beam laterally across the sample through the centers of the irradiated areas. The normalized exchange bias field ratio, $H_{\mathrm{eb}}/H_{\mathrm{eb,initial}}$, and the coercive field ratio, $H_{\mathrm{c}}/H_{\mathrm{c,initial}}$, are plotted in Fig. 1 as a function of the ion dose. Two different regimes are identified: i) A pronounced increase of H_{eb} and H_{c} is found in the dose regime between 10^{13} and $0.3{\cdot}10^{15}$ ions/cm^2. The maximum values are $H_{\mathrm{eb,max}} = -315$ Oe and $H_{\mathrm{c,max}} = 56$ Oe. ii) For doses above $0.3{\cdot}10^{15}$ ions/cm^2 the evolution is reversed and H_{eb} is reduced. The shift of the hysteresis loop decreases continuously with increasing ion dose. Finally, at an ion dose of $5.5{\cdot}10^{15}$ ions/cm^2, the exchange bias effect is fully suppressed and the coercive field is reduced to a quarter of its initial value. Both the bias field H_{eb} and the coercive field H_{c} follow the same qualitative relationship. For a detailed discussion see [2].

To further examine the correlation between bias and coercivity magnetometry measurements were performed in the temperature range 25 – 180 °C. The temperature was stabilized by a closed loop controller. The loops for irradiation in the dose range from 10^{13} to 10^{14} ions/cm^2 showed no noticeable difference. Therefore, as representative values for this range, the results for $5{\cdot}10^{13}$ ions/cm^2 are shown. Figure 2a shows the values of H_{eb} as a function of temperature. The inset shows the same data normalized to the respective values at room temperature. All curves show the same, almost linear decrease with increasing temperature. The deviation from a Brillouin function type relationship, as might be expected at first hand, can be understood on the basis of the grain size distribution [3, 4]. By increasing the temperature smaller grains become instable first and do not contribute to the bias effect any more. The blocking temperature for all ion doses including the zero dose value is $T_{\mathrm{B}} = 155$ °C which is significantly lower than the bulk Néel temperature of $T_{\mathrm{N}} = 220$ °C for FeMn. However, the coercive field H_{c} exhibits a plateau around the blocking temperature (Fig. 2b). This can be understood by a weakened AF spin configuration at temperatures near the Néel temperature. The AF spin configuration does not stay fixed on reversal of the F layer. This causes an uniaxial anisotropy instead of an unidirectional one. This phenomenon is comparable to the coercivity enhancement experienced at the onset of exchange bias with increasing AF layer thickness [5].

Work supported by the EC-TMR program "DYNASPIN" No. FMRX-CT97-0124.

References

[1] T. Mewes, R. Lopusnik, J. Fassbender, B. Hillebrands, M. Jung, D. Engel, A. Ehresmann, H. Schmoranzer, Appl. Phys. Lett. **76**, 1057 (2000).

[2] A. Mougin, T. Mewes, J. Fassbender, B. Hillebrands, M. Jung, D. Engel, A. Ehresmann, H. Schmoranzer, IEEE Trans. Magn., in press.

[3] P.J. van der Zaag, Y. Ijiri, J.A. Borchers, L.F. Feiner, R.M. Wolf, J.M. Gaines, R.W. Erwin, M.A. Verheijen, Phys. Rev. Lett. **84**, 6102 (2000).

[4] M.D. Stiles, R.D. McMichael, Phys. Rev. B **60**, 12950 (1999).

[5] R. Jungblut, R. Coehoorn, M.T. Johnson, Ch. Sauer, P.J. van der Zaag, A.R. Ball, Th.G. Rijks, J. aan de Stegge, A. Reinders, J. Magn. Magn. Mat. **148**, 300 (1995).

6.13 Magnetic nanopatterning of the FeNi/FeMn exchange bias bilayers by ion irradiation

A. Mougin, S. Poppe, J. Fassbender, and B. Hillebrands[1]

Ion irradiation is an excellent tool to modify magnetic properties on the sub-micrometer scale, without modification of the sample topography. We utilize this effect to magnetically pattern exchange bias double layers using resist masks patterned by e-beam lithography. Ion irradiation through the masks leads to a lateral modification of the magnetization reversal behavior and allows one to study the magnetization reversal as a function of the exchange bias field strength on a single sample. Results are presented on the macroscopic and microscopic magnetization reversal using the magneto-optic Kerr effect and magnetic force microscopy, respectively.

For the preparation of the FeNi/FeMn exchange bias bilayers see our report in Chapter 6.11. The magnetic properties were investigated *ex situ* by longitudinal magneto-optical Kerr-effect (MOKE) magnetometry at room temperature. The exchange bias field, H_{eb}, and the coercive field, H_{c}, were found to be homogeneous across each sample. An initial exchange bias field, $H_{\mathrm{eb,initial}}$, of –150 Oe is found and the coercive field is 35 Oe, which is considerably enhanced over the respective single FeNi film value.

After magnetic characterization, the samples were covered with a 700 nm thick PMMA layer. In a next step, arrays of squares were patterned by electron beam lithography in the resist layer using a JEOL 5DII e-beam writer. The development of the PMMA resist allows thus a local irradiation through the opened square windows. Then, the samples were inserted into an ion optical bench and irradiated through the mask with He ions, produced in a Penning type source and accelerated by 10 kV. The 700 nm thick PMMA layer fully protects the magnetic samples from 10 keV He ions outside the square resist openings [10]. Next, the resist was removed using an oxygen plasma.

The magnetic behavior of the samples was first investigated macroscopically by longitudinal Kerr effect magnetometry at room temperature. Figure 1a shows the hysteresis curve from a 5 µm × 5 µm square array with a 5 µm spacing, i.e., the fractional coverage of the irradiated areas is 1/4. The ion dose ($6 \cdot 10^{15}$ ions/cm^2) was chosen such as to suppress the exchange bias field in the irradiated areas [8, 9]. As expected, the macroscopic hysteresis curve consists of two contributions: the irradiated areas of the sample display a nearly unbiased behavior $H_{\mathrm{eb}} = -25$ Oe with low coercivity (regime b), whereas the unpatterned area of the sample exhibits a loop of high coercivity, shifted by –150 Oe (regime a). It is noted that the exchange bias field in this region is the same as in the unprocessed bilayer.

In the following, we investigate the evolution of the magnetization distribution during magnetization reversal along the hysteresis loop as indicated in Fig. 1a. A Digital Instrument magnetic force microscope, equipped with a phase detection system, was used to image the magnetic domain structure as well as the morphology of the irradiated films. Figure 1b-1 shows a 25 µm × 25 µm atomic force microscopy image of the sample after irradiation and removal of the patterned resist. The morphology is almost not damaged by the irradiation. In some areas small portions of residual PMMA are observed. The magnetic force microscopy images are shown in Fig. 1b. Images (1b-2) to (1b-6) show the domain evolution with decreasing applied

---

[1] In collaboration with G. Faini, Laboratoire de Microstructure et de Microélectronique, Bagneux (France); U. Ebels, Institut de Physique et Chimie des Matériaux de Strasbourg (France); M. Jung, D. Engel, A. Ehresmann, and H. Schmoranzer, Universität Kaiserslautern

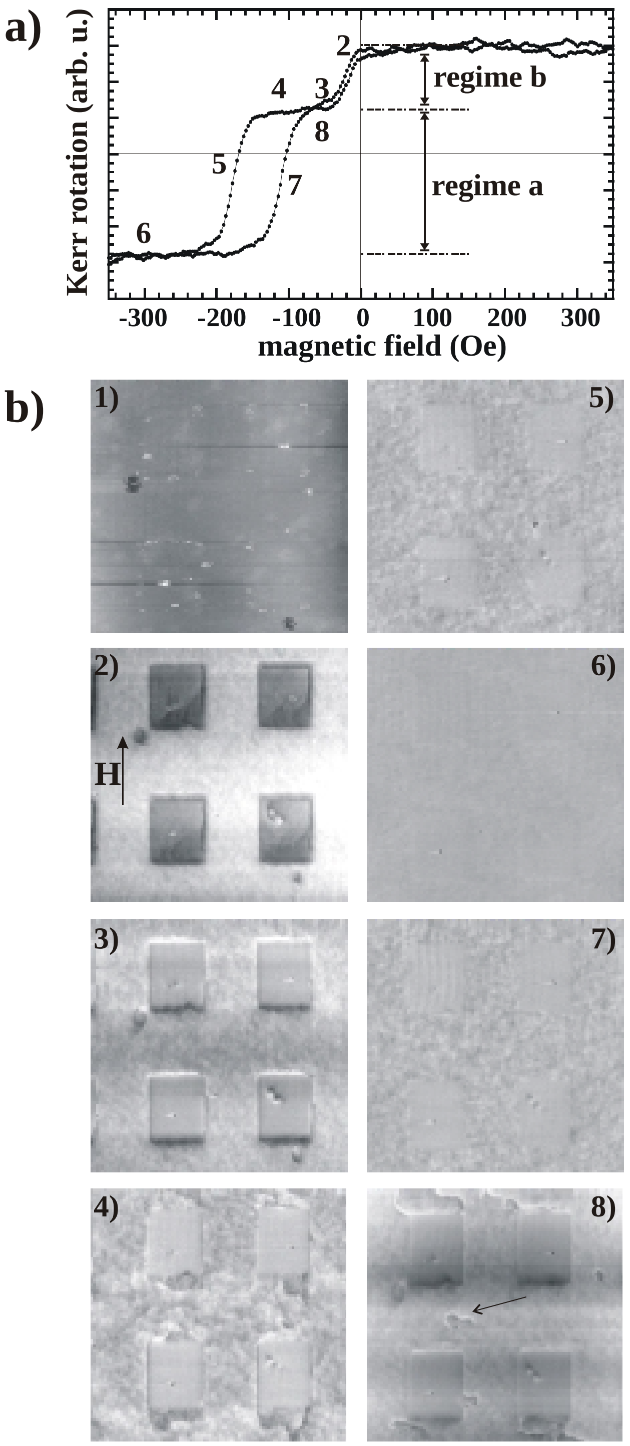

Fig. 1: a) Hysteresis curve from a FeNi/FeMn exchange bias sample, irradiated through a 5 µm × 5 µm square array with 5 µm spacing. The contribution of the as prepared sample is indicated (regime a). The irradiated areas are almost unbiased as shown in regime b. b) 25 µm × 25 µm atomic force microscopy image of the sample, after irradiation and removal of the PMMA mask (1). Corresponding magnetic force microscopy images illustrating the hysteresis loop along the bias direction. The direction of the applied field is indicated by an arrow in image (2). Decreasing the field, (2): H = –15 Oe, (3): H = –55 Oe, (4): H = –110 Oe, (5) H = –180 Oe, (6): H = –300 Oe and increasing the field, (7) H = –100 Oe, (8) H = –55 Oe.

field from remanence to negative saturation. Images (1b-7) to (1b-8) were taken next with increasing field.

Due to the polycrystalline nature of the NiFe layer, the reversal of the irradiated and non-irradiated regions takes place involving an incoherent rotation process. With an applied field of –15 Oe (Fig. 1b-2), one can see that the magnetization reversal of the 5 µm × 5 µm irradiated squares has already started. This is consistent with the interpretation of the hysteresis loop,

Fig. 1a, where the reversal of regime (b) is attributed to the irradiated region. At a field value of –55 Oe (Fig. 1b-3), the squares are in the reversed single domain state and thus aligned antiparallel to the non-reversed biased region (regime a). This is concluded from the strong contrast at the top (bright) and bottom (dark) border between the irradiated and non-irradiated regions. At this field value, a weak magnetic contrast is also visible in the non-irradiated regions (Fig. 1b-3) indicating the magnetic fluctuations due to the polycrystalline structure. The misorientation of the polycrystalline grains induces a random orientation of the local anisotropy which will add to the local fluctuations in the exchange bias field. At a field value of –110 Oe, these fluctuations increase to an almost multi-domain like structure of irregular shape (Fig. 1b-4). In addition, large, almost reversed regions as well as domain walls appear (Fig. 1b-4), which are located at the borders of the irradiated squares (regime b). These regions reverse in a slightly lower field, since the direct intralayer exchange coupling between the irradiated and non-irradiated regions promotes the reversal process. Furthermore, the dipolar fields arising from the head-to-head alignment of the magnetization in regions (a) and (b) add to the applied field. By further increasing the field strength (Fig. 1b-5), the ripple contrast remains but is weaker. In total, the reversal of the grains in the non-irradiated regions occurs rapidly, in accordance with the reversal shown in the square hysteresis loop of Fig. 1a, regime (a). Upon further decreasing the applied field, the domain structure converts to a quasi-single domain state, with the magnetization completely reversed in its direction with respect to the initial bias direction (Fig. 1b-6). Upon increasing the applied field again (Fig. 1b-7), the ripple like structure is observed again in the non-irradiated biased regions. The reversal back to the initial state, where the non-irradiated regions are almost in their initial configuration, is completed at a field of -55 Oe, see Fig. 1b-8. It is noted, that those regions, which underwent reversal first upon decreasing the field, remain now pinned and that 360° domain walls appear, as indicated by the arrow in Fig. 1b-8. Such walls were not observed upon decreasing the field and result from the successive reversal of grains. Also interesting to note is the fact that a number of these walls terminate at the irradiated regions. This can be explained by the fact that the magnetization orientation inside the core of the 360° domain wall is parallel to the magnetization inside the irradiated, unbiased regions. This lowers the energy at the extremities of the 360° wall. While the domain structure is slightly different, depending on whether the applied field is decreasing or increasing, the reversal process seems similar. We do not observe any clear asymmetry of domain nucleation in our patterned samples, as previously reported [11]. However, our observations are in agreement with models which claim that the increase of coercivity in AF/F bilayers requires that the magnetization reversal in the ferromagnetic layer proceeds by either non uniform spin rotation or by domain wall nucleation, strongly pinned during the reversal by the coupling with the domain walls in the AF layer [1,11-13].

In conclusion, we demonstrate that magnetic nanopatterning of exchange bias coupled double layers is possible using ion irradiation. We report on the first results concerning the magnetization reversal in the irradiated and non irradiated regions. From the fundamental point of view, it appears now clearly that the understanding of exchange bias requires to take into account the reversal of the ferromagnetic layer [11-13]. The reversal of exchange biased areas themselves as well as the coupling mechanisms with the irradiated areas are currently subject of further investigations.

Work supported by the EC-TMR program "DYNASPIN" No. FMRX-CT97-0124.

References

[1] J. Nogues, I. K. Schuller, J. Magn. Magn. Mater. **192**, 203 (1999).

[2] W.H. Meiklejohn, C.P. Bean, Phys. Rev. **102**, 1413 (1956), and **105**, 904 (1957).

[3] C. Tsan, J. Appl. Phys. **55**, 2226 (1984).

[4] B. Dieny, V.S. Speriosu, S.S.P. Parkin, B.A. Gurney, D.R. Wilhoit, D. Mauri, Phys. Rev. B 43, 1297 (1991).

[5] C. Chappert, H. Bernas, J. Ferré, V. Kottler, J.P. Jamet, Y. Chen, E. Cambril, T. Devolder, F. Rousseaux, V. Mathet, H. Launois, Science **280**, 1919 (1998).

[6] T. Devolder, C. Chappert, Y. Chen, E. Cambril, H. Bernas, J.P. Jamet, J. Ferré, Appl. Phys. Lett. **74**, 3383 (1999).

[7] D. Ravelosona, C. Chappert, V. Mathet, H. Bernas, Appl. Phys. Lett. **76**, 236 (2000).

[8] T. Mewes, R. Lopusnik, J. Fassbender, B. Hillebrands, M. Jung, D. Engel, A. Ehresmann, H. Schmoranzer, Appl. Phys. Lett. **76**, 1057 (2000).

[9] A. Mougin, T. Mewes, R. Lopusnik, M. Jung, D. Engel, A. Ehresmann, H. Schmoranzer, J. Fassbender, B. Hillebrands, IEEE Trans. Magn. in press; A. Mougin, T. Mewes, M. Jung, D. Engel, A. Ehresmann, H. Schmoranzer, J. Fassbender, B. Hillebrands, submitted to Phys. Rev. Lett.

[10] SRIM 2000 code, J.F. Ziegler, J.P. Biersack, U. Littmark, *The Stopping and Range of Ions in Solids*, Pergamon, New York, Oxford (1985).

[11] V. Nikitenko, V. Gornakov, A. Shapiro, R. Shull, K. Liu, S. Zhou, C. Chien, Phys. Rev. Lett. **84**, 765 (2000).

[12] J. Yu, A. Kent, S. Parkin, J. Appl. Phys. **87**, 5049 (2000).

[13] C. Leighton, J. Nogues, B. Jönsson-Akerman, I. Schuller, Phys. Rev. Lett. **84**, 3466 (2000).

E. Elastic Properties

6.14 Elastic properties of thick c-BN films

T. Wittkowski, J. Jorzick, K. Jung, and B. Hillebrands[1]

Boron nitride in its cubic modification (c-BN) has become a material of wide scientific interest. Although the elastic tensor of the single crystal material was determined experimentally a few years ago [1], the elastic constants of c-BN films are still little known. Thin c-BN films on typical substrates such as Si, TiN or steel represent systems of type "fast film – slow substrate" with respect to their sound velocities. In this case the only shear-vertical mode in the discrete surface mode spectrum is the Rayleigh mode. The dispersion of this mode does in general not contain enough information to determine several independent elastic constants. In practice the problem is even more involved because normally a soft h-BN layer between the substrate and the c-BN film is present. In this study these difficulties are surmounted by investigating a transparent c-BN film of approximately 1.8 μm thickness with Brillouin light scattering spectroscopy (BLS), because in addition to the surface mode a bulk mode was detected.

With Fourier transform infrared (FTIR) spectroscopy it was shown that the film predominantly consists of the cubic phase of BN. By means of XRD the c-BN crystallite size was determined to be approximately 5 nm in diameter with no preferred orientation. A crystalline sp^2-bonded BN phase was not detected. The mass density is reliably estimated to be $\rho = 3.3$ g/cm^3 which is 95% of the single crystal density value. With photo-spectrometry the refractive index was shown to coincide with the single crystal index $n = 2.13$.

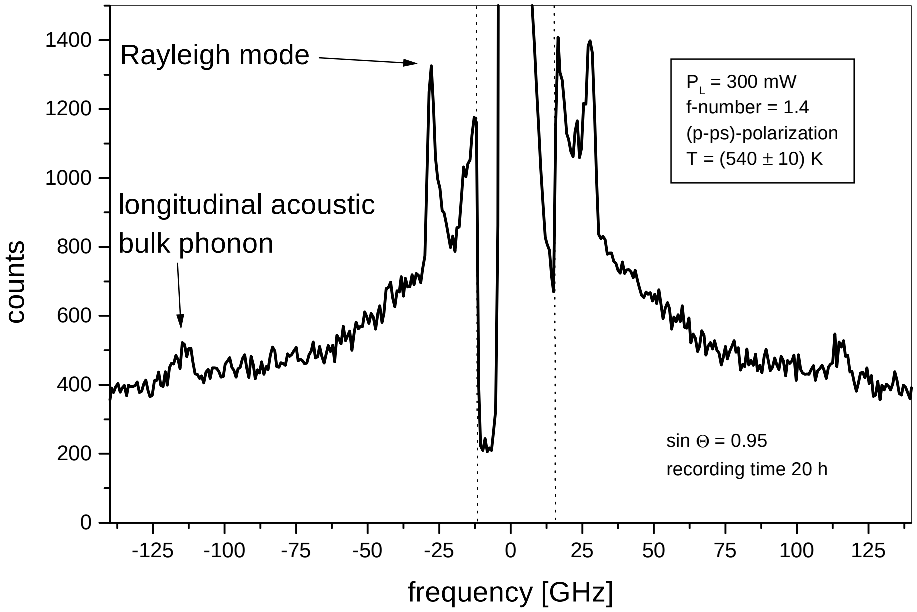

Fig. 1: Brillouin light scattering spectrum of a 1.8 μm thick c-BN film. The dotted lines indicate the range in which the elastically scattered light is suppressed by a shutter system.

---

[1] In collaboration with K. Bewilogua and M. Keunecke, Fraunhofer-Institut für Schicht- und Oberflächentechnik, Braunschweig, Germany.

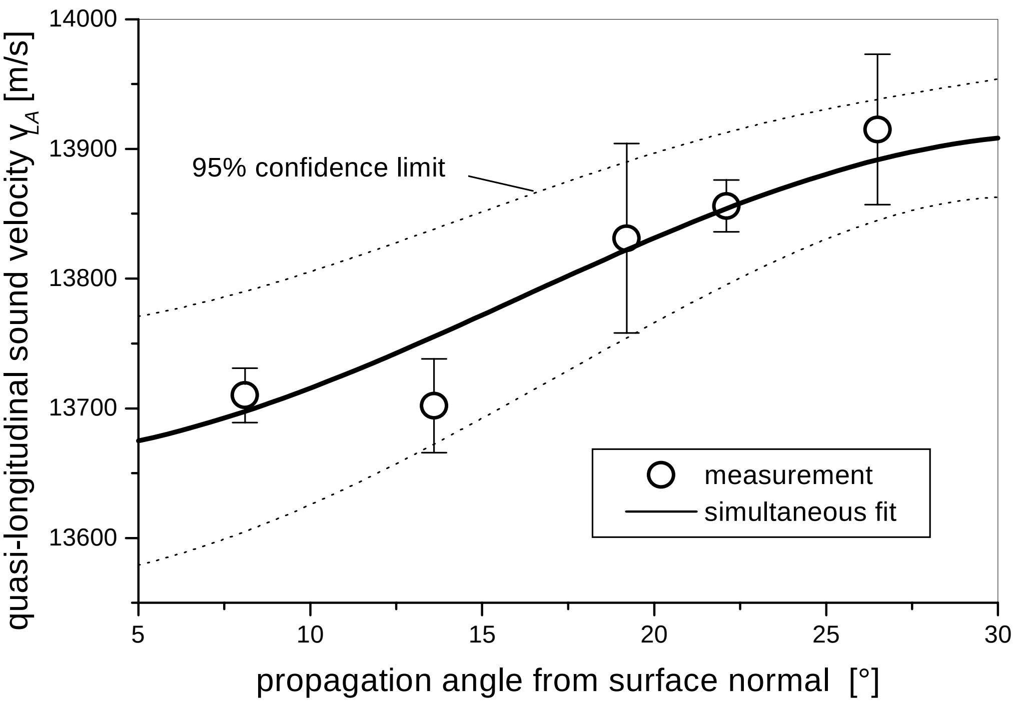

Fig. 2: Sound velocity of the quasi-longitudinal acoustic phonon as a function of the propagation angle. The angular dependence of the sound velocity is evidence for an elastic anisotropy. The full curve shows the best fit result of a simultaneous fit of the Rayleigh velocity (not shown) and the quasi-longitudinal sound velocity with the elastic constants c_{11}, c_{33} and c_{44} as free parameters. In the investigated angular range the variation of the quasi-longitudinal velocity is dominated by the constants c_{33} and c_{44}. For the surface mode the dominating constants are c_{44} and c_{11}. The fitting procedure takes the individual error bars of the measurement into account. The obtained χ^2-sum, divided by the number of degrees of freedom is smaller than 1, indicating a moderately good fit. The fitting results are listed in Tab. 1.

BLS measurements were performed in backscattering geometry with the incident light polarized in the sagittal plane. The angle of incidence and reflection was varied from $\Theta = 17°$ to $\Theta = 72°$. During the measurement the sample was held at a temperature $T = 540$ K to increase the scattering intensity. Figure 1 shows a Brillouin spectrum at a large angle of incidence. Clearly visible are two signal peaks of which the one at lower frequency is identified to be the Rayleigh peak. Its frequency depends on the angle of incidence, $\nu_R = (2v_R/\lambda)\cdot\sin\Theta$, where v_R is the phase velocity of the Rayleigh wave and $\lambda = 514.5$ nm. The high frequency signal originates from the longitudinal acoustic bulk phonon of the film at the frequency $\nu_{LA} = (2n/\lambda)\cdot v_{LA}$. The velocity of the Rayleigh mode and an average velocity of the longitudinal bulk wave are determined directly from the experiment. The two independent elastic constants, which describe an elastically isotropic material, are $c_{11} = (626\pm4)$ GPa and $c_{12} = (187\pm23)$ GPa. The Poisson's ratio results to $\nu = 0.23\pm0.02$. This is a first-time direct measurement of two independent elastic waves in a c-BN film.

Figure 2 shows the angular dependence of the phase velocity of the quasi-longitudinal bulk wave. Since the velocity is not constant, this is evidence for an elastic anisotropy of the film material. In order to describe the elastic behavior properly, a refined model which assumes the film material to be isotropic in the film plane, but allows anisotropy in the perpendicular direction, is used. This is the symmetry of the hexagonal crystal classes which requires four independent elastic constants, namely c_{11}, c_{13}, c_{33} and c_{44}, to evaluate the velocities of the Rayleigh

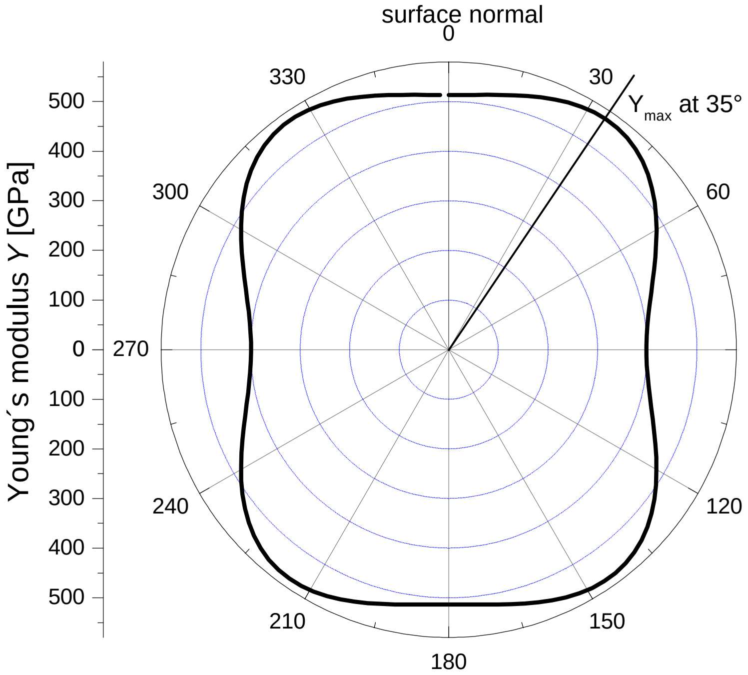

Fig. 3: Polar plot of the intersection of the surface of the Young's modulus with any meridian plane. Perpendicular and parallel to the surface the modulus is 513 GPa and 398 GPa, respectively. The Young's modulus possesses the maximum value of 562 GPa at an angle of 35° from the surface normal. This fact might be important for technical applications.

wave and the quasi-longitudinal wave. In a simultaneous fit of the Rayleigh velocity and the angular dependent quasi-longitudinal velocity, the elastic constants c_{11}, c_{33} and c_{44} are determined precisely. The value of c_{13}, which is assumed be be constant here, influences both velocities to a rather low extend, hence it is fixed at the value which was determined from the isotropic model, $c_{13} = 187$ GPa. All fitting results are summarized in Tab. 1 together with the single crystal data.

It is now possible to analyze the material elastic properties in detail. Here, a brief summary is given: The bulk modulus is $K = (300\pm24)$ GPa, which is 3/4 of the single crystal modulus. The elastic anisotropy, defined by the ratio of the extensional stiffness constants c_{11}/c_{33}, amounts to approximately 4/5. The Young's modulus is direction dependent and possesses a maximum value of $Y = 562$ GPa at an angle of 35° away from the surface normal (see Fig. 3). The deviation of the film elastic constants from the averaged single crystal constants is expected to be due to compliant sp^2-bonded grain boundaries. Preliminary results of AFM and XRD investigations indicate that the anisotropy is likely to be caused by grain boundaries on the 10–100 nm length scale as is described by the growth model of *Messier* et al. [3], rather than by sub-grain boundaries, which separate single crystallites on a 1–10 nm length scale.

Work supported by the Deutsche Forschungsgemeinschaft.

		c_{11}	c_{12}	c_{13}	c_{33}	c_{44}	K	Reference
single crystal	theor.	837	182	-	-	493	400	[2]
single crystal	exp.	820	190	-	-	480	400	[1]
VRH-mean		941	130	-	-	-	400	
film	exp.	494 ± 32	187 ± 23	187 ± 23	616 ± 1	255 ± 4	300 ± 24	present study

Tab. 1: Elastic constants of c-BN in units of GPa. The Voigt-Reuss-Hill (VRH) mean values for an isotropic aggregate of cubic crystallites are calculated using the single crystal values given in [1]. The film constant c_{12} is obtained within the isotropic model. In order to fit c_{11}, c_{33} and c_{44} in the hexagonal model, $c_{12} = c_{13}$ is held constant.

References

[1] M. Grimsditch, E.S. Zouboulis, J. Appl. Phys. **76**, 832 (1994).
[2] K. Kim, W.R.L. Lambrecht, B. Segall, Phys. Rev. B **53**, 16310 (1996).
[3] R. Messier, A.P. Giri, R.A. Roy, J. Vac. Sci. Technol. A **2**, 500 (1984).

F. Instrumental

6.15 Improved time resolution in time-resolved magneto-optic Kerr effect measurements

M. Bauer, R. Lopusnik, J. Fassbender, and B. Hillebrands

Progress in developing ultra fast magnetic sensors for magnetic random access memory (MRAM) and hard disk heads, as well as in improvements of media for high data rates demands a detailed knowledge of the magnetization reversal process on a time scale far below one nanosecond. The time resolution in the experiments is often limited by timing jitter. Many different jitter sources contribute to the overall jitter. In order to improve the time resolution of the whole setup a careful evaluation of the jitter sources is necessary. In time-resolved magneto-optic Kerr effect experiments a timing jitter below one picosecond and a signal bandwidth up to 200 GHz can be achieved using an optical delay together with a photoconductive switch as a current pulse source [1].

Often, for the generation of time delay and current pulses a solution using solely electronic components is favored in many practical situations because of its rich flexibility and speed. A timing jitter of 25 ps rms [2], 40 ps rms [3], 50 ps rms [4] and 100 ps rms [5] is reported in these experiments leading to a -3dB signal bandwidth of 5.3 GHz, 3.3 GHz, 2.7 GHz and 1.3 GHz, respectively ($f_{-3dB} = 0.133 / \sigma_{jitter}$). A careful analysis reveals that the delay generator as the dominant origin for jitter.

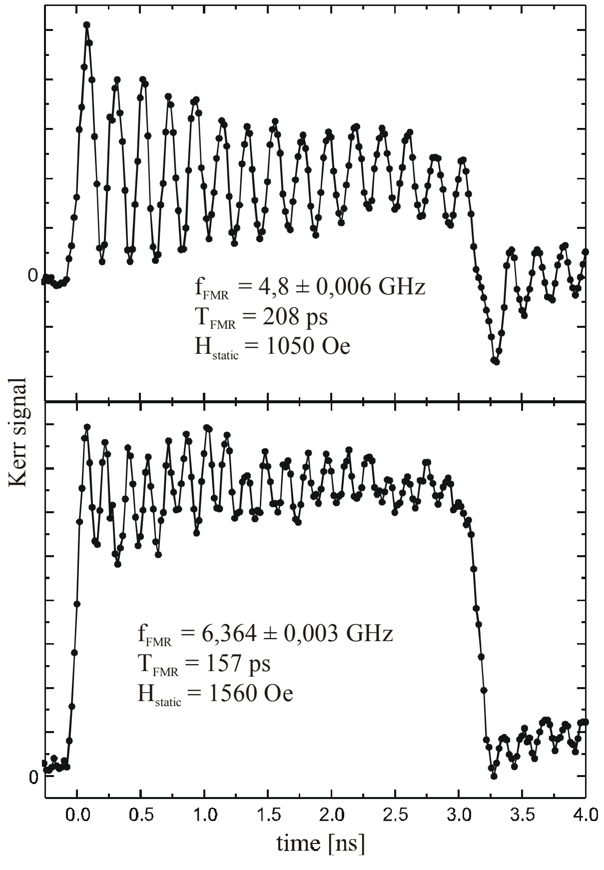

Fig. 1: Improvement in signal bandwidth. A garnet sample is saturated in-plane with a static magnetic field H_{static} as specified in the figure. Perpendicular to H_{static} a magnetic field pulse (rise time 55 ps, duration 3 ns, fall time 130 ps, amplitude 1 Oe) is excited by a 50 µm wide strip line. The resulting magnetization response on top of the strip line is measured by means of time-resolved magneto-optic Kerr effect magnetometry. The frequency f_{FMR} and the period T_{FMR} of the signal are determined from a Fourier transformation of the signal during the pulse excitation. Two different scenarios are shown. In the top graph, the pulse rise time is far below $T_{FMR} / 2$ leading to a fully developed precession amplitude with a frequency of 4.8 GHz. In the bottom graph, the pulse rise time is of the order of $T_{FMR} / 2$. Only a reduced precession amplitude with a frequency of 6.364 GHz is measured.

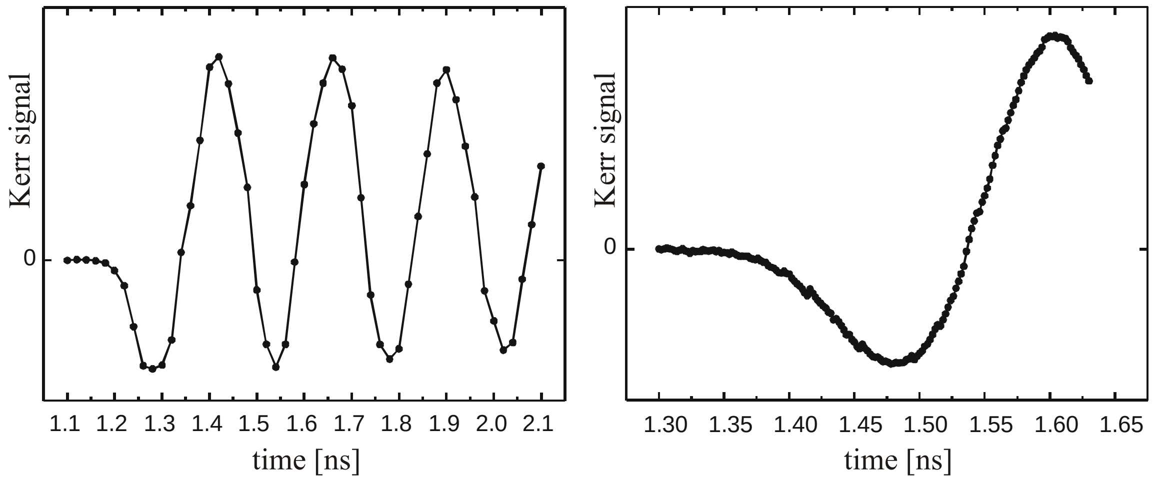

Fig. 2: Improvement in time delay granularity. An oscillating magnetization signal of frequency 4.15 GHz is measured by time-resolved magneto-optic Kerr effect with the TIMO setup. The data shown on the left hand side are obtained with the conventional delay generator with the smallest usable time delay step size of 20 ps. On the right hand side the same signal is recorded with a time delay step size of 2 ps utilizing an improved additional electronic circuit. With this technique sufficient oversampling capabilities are now available. The small absolute shift in time delay of the signal is due to the technical procedure.

In our time resolved magneto-optic magnetometer (TIMO) setup [6] an infrared picosecond pulsed diode laser with a pulse width at FWHM of 17.6 ps is used. This corresponds to a jitter contribution of 7.5 ps rms ($\sigma_{\text{laser}} = 0.425 \cdot T_{\text{laser}}$). Additional jitter sources are the laser trigger output (4 ps rms), the pulse generator (3 ps rms) and the delay timing unit (< 10 ps rms). The unique feature of our setup is the delay timing unit with its extremely low jitter [7]. The performance of the whole setup including all jitter sources is a jitter of < 15 ps rms, which results in a -3dB signal bandwidth of 9 GHz. Figures 1 and 2 show the improvements in signal bandwidth and time delay granularity. Time dependent signals far above 5 GHz can be measured with our setup.

Work supported by Siemens AG, the German Ministry of Research and Technology (BMBF), and the EC-TMR program "DYNASPIN" No. FMRX-CT97-0124.

References

[1] M.R. Freeman, M.J. Brady, J.F. Smyth, *Extremely high frequency pulse magnetic resonance by picosecond magneto-optic sampling*, Appl. Phys. Lett. **60**, 2555 (1992).
[2] C.H. Back, J. Heidmann, J. McCord, *Time Resolved Kerr Microscopy: Magnetization Dynamics in Thin Film Write Heads*, IEEE Tans. Magn. **35**, 637 (1999).
[3] T.J. Silva, T.M. Crawford, *Methods for Determination of Response Times of Magnetic Head Materials*, IEEE Trans. Magn. **35**, 671 (1999).
[4] M.R. Freeman, J.F. Smyth, *Picosecond time-resolved magnetization dynamics of thin-film heads*, J. Appl. Phys. **79**, 5898 (1996).
[5] C.H. Back, A. Taratorin, J. Heidmann, *Nonlinear timing shift in high frequency magnetic recording determined with time resolved Kerr microscopy*, J. Appl. Phys. **86**, 3377 (1999).
[6] M. Bauer, R. Lopusnik, J. Fassbender, B. Hillebrands, S*uppression of magnetic field induced magnetization precession by pulse tailoring*, Appl. Phys. Lett. **76**, 2758 (2000).
[7] M. Bauer, Ph.D. Thesis, Universität Kaiserslautern (2001), in preparation.

G. Transfer of Technology

6.16 Plasma beam deposition of hard amorphous carbon films

C. Osthöver, K. Jung, and B. Hillebrands

The goal of this research project was the development of hard carbon layers for technical applications. The activities have been mainly concentrated on two modifications of the material. One aim was the reduction of the stress of highly tetrahedral hydrogenated amorphous carbon (ta-C:H) films in order to produce thicker coatings of this superhard material. The second aim was the deposition of medium hard amorphous carbon films on temperature sensitive polymers. This material, which should be scratch resistant with respect to steel and flexible enough not to delaminate if the substrate is strongly bent, is well suited for various medical purposes because of its biocompatibility and its tendency to slow down the settlement of bacteria.

The experimental work has been performed at the Institute of Thin Film Technology ("Institut für Dünnschichttechnologie") a center for technology transfer of the University of Kaiserslautern. The institute was established to develop and to optimize hard coatings for special applications in small and medium sized factories. Besides the amorphous carbon films deposited by a plasma beam technique several different ceramic materials as WC, TiN, TiAlN, SiC or CrN can be grown by magnetron sputtering in combination with ion plating.

Highly tetrahedral hydrogenated amorphous carbon is grown by plasma beam deposition at low background pressure with acetylene as the working gas. The $C_2H_2^+$-ions must have well defined kinetic energies of about 200 eV, i.e. 92 eV per C-atom [1]. The ta-C:H films, which contain 25% hydrogen and reach a Vickers hardness of 60 GPa, exhibit usually a high internal stress. With a filtered catholic vacuum arc, ta-C films without hydrogen can be grown [2]. It has already been shown that the stress of ta-C can be reduced by implanting boron atoms. Whereas 80% of the carbon atoms are in the sp^3 configuration the boron atoms are predominantly sp^2 bonded [3].

The present studies were devoted to the problem whether the introduction of a doping material would also reduce the stress in the case of ta-C:H. The experiments have been performed with a plasma beam source of CCR GmbH. The undoped ta-C:H films show a stress of about 10 GPa which prevented the growth of films with more than 300 nm thickness. By introducing a few percent of nitrogen to the process gas the internal stress could be reduced to about 5.5 GPa. Thus it was possible to produce coatings with a thickness of up to 800 nm.

In order to introduce a non-gaseous material into the films higher experimental efforts were necessary. To this purpose the plasma beam source has been equipped with an integrated sputter source. Using a B_4C target, boron could be introduced into the plasma. A boron content between 2 and 3 % reduces the internal stress down to about 2 GPa. With this method 1.4 µm thick films were grown with a hardness of 40 GPa. Thus it is now possible to reduce the internal stress by a factor of 5 while maintaining the super-hardness of the material. The following parameters have been used for the deposition:

rf-power in the plasma discharge: 400 W
rf-power at the sputter target: 1200 W
C_2H_2 gas flux: 15 sccm
pressure in the vacuum chamber: $5 \cdot 10^{-4}$ mbar
distance source to substrate: 8 cm
deposition rate: 70 nm/min

ion energy: 170 eV
ion current: 0.4 mA/cm^2

The deposition of hard carbon films in the diamond-like and in the ta-C:H modification with a typical ion flux density of 1 mA/cm^2 is combined with a power transport of about 0.2 W per cm^2 to the surface of the substrate. To estimate the temperature rise a thermocouple has been placed directly in the plasma beam. It showed a temperature of 220°C in the thermal equilibrium. This temperature is much too high for coating typical polymeric implantates, which stay for a limited period of time in the human body, for example in the form of catheters. These implantates require a maximum coating temperature of below 40°C. To achieve this, not only the ion flux but also the ion energy had to be reduced substantially.

Former research activities to deposit amorphous carbon films from plasma excited acetylene gas at kinetic energies below 30 eV led to soft soot-like films which could be wiped off by a piece of paper [4]. In these former experiments the films have been deposited in a CVD reactor chamber with gas pressures of more than $0.6\cdot10^{-3}$ mbar. In this case the delay time of the acetylene gas in the chamber was rather long and the collision rate is relatively large. Therefore the electronically and/or vibrationally activated molecules, ions and radicals coagulate to higher hydrocarbons and slow down. In consequence the energy per carbon atom and the velocity of the molecules was rather small. The hydrocarbons can no longer form a dense network.

In modern plasma sources characterized by a very effective rf excitation of the plasma, the gas pressure can be chosen very low and the delay time of the gas molecules in the source is short. Therefore predominantly $C_2H_2^+$ or C_2H^+ ions leave the plasma source. In the newly developed deposition process the ion energy and the ion flux are reduced by a factor of ten with respect to the conditions typical for the production of diamond-like carbon films. Thus the energy flux density is reduced by two orders of magnitude. The temperature of the substrate is practically not increased during the deposition process.

Despite the fact that the impinging ions have only a kinetic energy of 20 eV the deposited films are rather hard and scratch resistant with respect to steel. The films exhibit a Vickers hardness of H = 10 GPa and an elasticity of E = 60 GPa. The ratio E/H of 6 is in agreement with the constraint model of Angus [5]. That means the carbon films are thermodynamically stable. The films are well suited for medical products because of their biocompatibility. Their dense surface structure retards the settlement of bacteria.

Work supported by the Stiftung für Innovation of the state of Rheinland-Pfalz.

References

[1] M. Weiler, S. Sattel, T. Giessen, K. Jung, H. Ehrhardt. V.S. Veerasami, J. Robertson, *Preparation and properties of highly tetrahedral hydrogenated amorphous carbon*, Phys. Rev. B **53**, 1594 (1996).

[2] M. Chhowalla, J. Robertson, C.W. Chen, S.R.P. Silva, G.A.J. Amaratunga, W.L. Milne, *Influence of ion energy and substrate temperature on the optical and electronic properties of tetrahedral amorphous carbon (ta-C) films*, J. Appl. Phys. **81**, 139 (1997).

[3] M. Chhowalla, Y. Yin, G.A.J. Amaratunga, D.R. McKenzie, Th. Frauenheim, *Highly tetrahedral amorphous carbon films*, Appl. Phys. Lett. **69**, 2344 (1996).

[4] R. Kleber, M. Weiler, A. Krüger, S. Sattel, G. Kunz, K. Jung, H. Ehrhardt, *Influence of ion energy and flux composition on the properties of plasma-deposited amorphous carbon and amorphous hydrogenated carbon films*, Diam. Rel. Mat. **2**, 246 (1993).

[5] J.C. Angus, P. Koidl, S. Domitz,"Carbon Thin Films" in *Plama Deposited Thin Film* (Ed.: J. Mort und F. Jansen), CRC press, Cleveland (1986).

6.17 a-C and TiNM$_x$: New Applications in Medicine

Heinz Busch and Udo Grabowy[1]

Today in industrial countries heart disease is responsible for about 30% of all death cases. The origin is the stricture of coronary arteries (arteriosclerosis). The state of the art technique to open the clogged areas is the percutanous transluminal coronary angioplasty (PTCA). Frequently, in 30-50% of all cases, the stenosis reoccurs (restenosis). Out of those patients, who have undergone PTCA, 50% also receive a miniature metal scaffold (stent) inserted in the artery. However, in about 10-60% of these cases, a so-called in-stent recidive stenosis appears.

Radioactive coatings for suppression of restinosis

In some studies [1] it was shown that radioactivity is the best method to reduce the restenosis rate (see Figs. 1 and 2) [2, 3].

The authors developed a new technique to prepare common Nitinol-Stents with a thin layer (TiNP) coating, where phosphorous (P) is the radioactive isotope, which is activated in a nuclear plant after coating. A PVD process was used for the coating [4].

The development of the layer system is now completed. The amount of phosphorous (P) is variable between 0-15 atomic percent. The hardness is comparable to TiN with 2300-2800 HV. The stress was largely decreased down to 0.5 GPa. For this reason, the layer system has excellent properties – it is wear and friction resistant and flexible. These are basic requirements for the use of stents, because a stent must be expandable and flexible. In the body the stent will be moved (micro- motions) several million times.

Fig 1: Swine artery (cut) six months after dilatation and stenting (stent without radioactivity). One can see that the vessel lumen is reduced due to cell reaction to the foreign body (restenosis) [7].

---

[1] Work performed at the Institut für Dünnschichttechnologie (IDST),Transferstelle der Universität Kaiserslautern am Technologiezentrum Oberflächen (TZO), Rheinbreitbach, Germany.

Fig. 2: Swine artery (cut) six months after dilatation and stenting with a β-active stent [6]. One can see no cell proliferation and that the vessel is open. The lumen is not reduced, no restenosis can be observed [7].

The next steps to be licensed as a CE-certified device under the german Medizinproduktegesetz (laws for medical products) are: a) Haemocompatibility tests, b) micro-motion in a human body-like environment, c) neutron activation of a coated stent in a nuclear plant and measurement of the distribution of dose rate with so called radio-chromic films [5].

Improvement of surgical tools by coating

A new field for the use of amorphous diamond like carbon layers is in emergency surgery after accidents in cooperation with the Berufsgenossenschaftliches Unfallkrankenhaus Hamburg Bergedorf, Prof. D. Wolter, and the University of Hamburg Harburg.

During the use of drills to make channels in bones for the subsequent placement of screws, the contact area is sometimes strongly heated up. Thereby the adjacent cells in the bone are destroyed and become necrotic.

This fact promotes, among the other problems, the immigration of germs as well as early loosening of the implant. A coating for improving the cutting process and suppression of the heating effect would be of great clinical and social interest [8]. By the use of a wear resistant amorphous carbon layer, with has a substantial smaller friction coefficient than steel, a first step was made to reduce the heating effect.

First tests with amorphous carbon coated drills at swine- and calve bones show encouraging results. Presently a device to determine the exact temperature in bones during the drilling procedure is under construction.

Metallic implants (see Fig. 3)

The biocompatibility of metallic implants like fixator systems [9] is still a current problem. Implants, consisting of pure titanium or titanium alloy, are increasingly in use because of their better biocompatibility compared to stainless steel. It is well known that high alloy steel releases heavy-metal-ions which have a negative influence on the immune system.

For the stabilization of complicated bone fractures fixator systems are partly used. With this

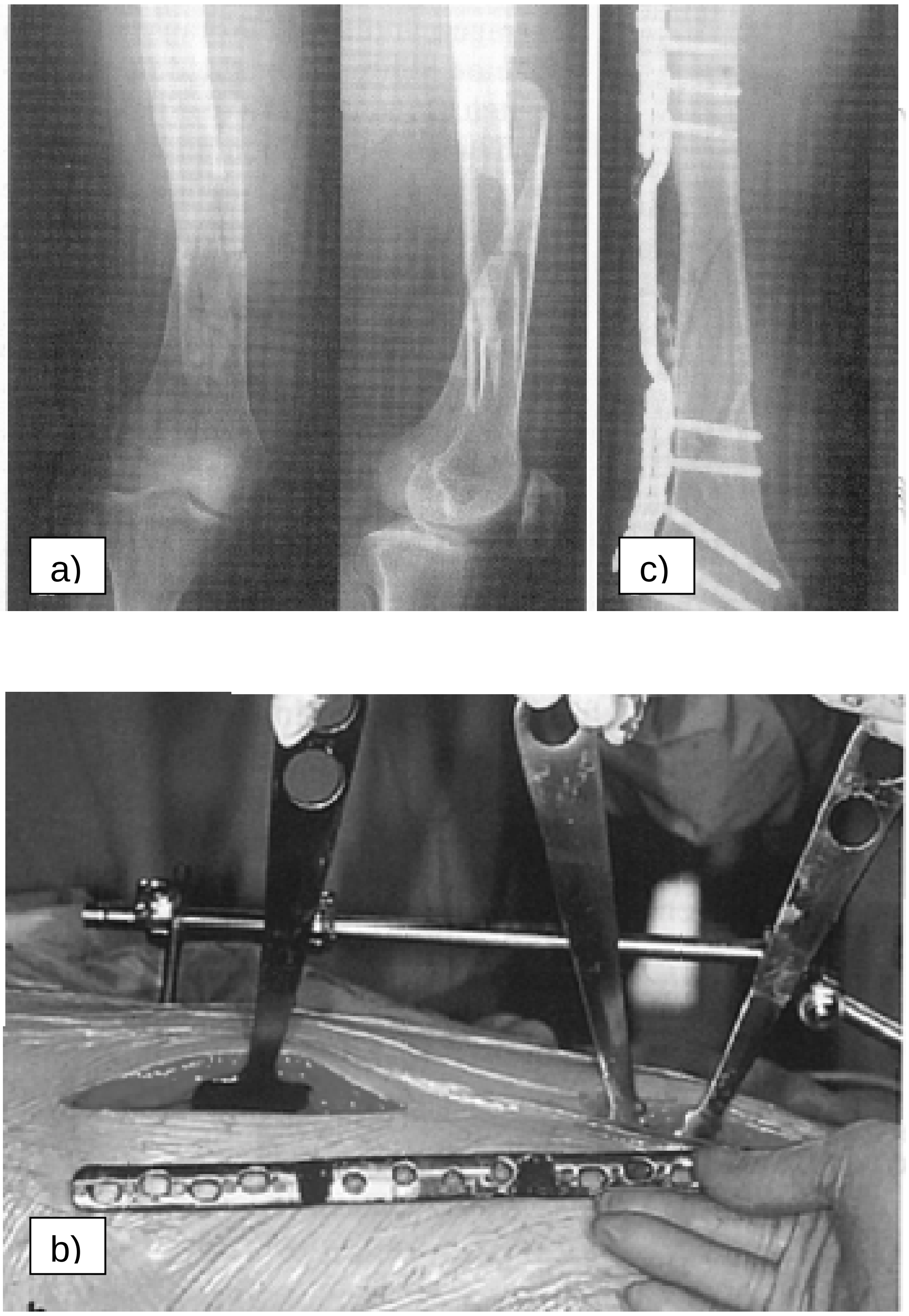

Fig. 3 [9]: a: Status after valgization operation due to a inborn hip diplasia, fracture and refracture of the right upper thigh (femur). b: Intra-operative application of an upper thigh fixator system. c: Post-operative X-ray image. One can see the fixator system and the screws.

method the implants pose a permanent interface between environment, tissue and bone. The immigration of bacteria via the surface of the implant is one of the biggest problems in the healing process. More than 50% of all patients suffer from inflammations.

At the beginning of 2001 implants will be coated with amorphous carbon to determine the influence of the rate of inflammations.

References

[1] P.K. Coussement, K.A. Robinson, Vascular Radiotherapy Monitor **3**, 25 (2000).
[2] K.A. Robinson, Vascular Radiotherapy Monitor **3**, 9 (2000).
[3] C. Hehrlein et al., Circulation **93**, 641 (1996).
[4] H. Busch, U. Grabowy, Annual Report 1999, Chapter 6.23, AG Magnetismus, Univ. Kaiserslautern (1999).
[5] W.V. Prestwich, T.J. Kennett, F.W. Kus, Med. Phys. **22**, 313 (1995).
[6] P. Fehsenfeld. et al., Semin Intervent Cardiol **3**, 157 (1998).
[7] R. Waksman, P.W. Serruys, Handbook of Vascular Brachytherapie, Second Edition (2000).
[8] D. Wolter, BG Unfallkrankenhaus Hamburg Bergedorf, private communication.
[9] D. Wolter, U. Schümann, K. Seide, Trauma Berufskrankheit **1**, 307 (1999).

Chapter 7: Publications

7.1 Published

1. *Brillouin light scattering from quantized spin waves in micron-size magnetic wires*
   J. Jorzick, S.O. Demokritov, C. Mathieu, B. Hillebrands, B. Bartenlian, C. Chappert, F. Rousseaux, A.N. Slavin
   Phys. Rev. B **60**, 15194 (1999).
2. *Brillouin light scattering from layered magnetic structures*
   B. Hillebrands
   in: *Light Scattering in Solids VII*, M. Cardona, G. Güntherodt (Eds.), Topics in Applied Physics **75**, Springer Verlag, Heidelberg, p. 174 (1999).
3. *Spin wave quantization and dynamic coupling in micron-size circular magnetic dots*
   J. Jorzick, S.O. Demokritov, B. Hillebrands, B. Bartenlian, C. Chappert, D. Decanini, F. Rousseaux, E. Cambril
   Appl. Phys. Lett. **75**, 3859 (1999).
4. *Magnetization reversal in ultrashort magnetic field pulses*
   M. Bauer, R. Lopusnik, J. Fassbender, B. Hillebrands
   J. Magn. Magn. Mat. **218**, 165 (2000).
5. *Characterization of elastic properties of hard carbon and boron nitride films using the Brillouin light scattering technique*
   T. Wittkowski, V. Wiehn, J. Jorzick, K. Jung, B. Hillebrands
   Thin Solid Films **368**, 216 (2000).
6. *Magnetization dynamics and concepts for fast magnetic switching*
   B. Hillebrands, J. Fassbender, S.O. Demokritov
   Magnetoelektronik, VDI-Technologiezentrum (ISBN 3-931384-31-4).
7. *Linear and nonlinear diffraction of dipolar spin waves in yttrium iron garnet films observed by space- and time-resolved Brillouin light scattering*
   O. Büttner, M. Bauer, S.O. Demokritov, B. Hillebrands, Yu.S. Kivshar, V. Grimalsky, Yu. Rapoport, A.N. Slavin
   Phys. Rev. B **61**, 11576 (2000).
8. *Space- and time-resolved Brillouin light scattering from nonlinear spinwave packets*
   O. Büttner, M. Bauer, A. Rueff, S.O. Demokritov, B. Hillebrands, A.N. Slavin, M.P. Kostylev, B.A. Kalinikos
   Ultrasonics **38**, 443 (2000).
9. *Suppression of magnetic field induced magnetization precession by pulse tailoring*
   M. Bauer, R. Lopusnik, J. Fassbender, B. Hillebrands
   Appl. Phys. Lett. **76**, 2758 (2000).
10. *Switching behavior of Stoner-like magnetic thin film elements*
    M. Bauer, J. Fassbender, B. Hillebrands
    J. Appl. Phys. **87**, 6274 (2000).

11. *Growth and magnetic properties of Fe films on vicinal to (001) substrates*
A.R. Frank, J. Jorzick, M. Rickart, M. Bauer, J. Fassbender, S.O. Demokritov,
B. Hillebrands, M. Scheib, A. Keen, A. Petukhov, A. Kirilyuk, Th. Rasing
J. Appl. Phys. **87**, 6092 (2000).

12. *Spatial and spatio-temporal self-focusing of spin waves in garnet films observed by space- and time-resolved Brillouin light scattering*
O. Büttner, M. Bauer, S.O. Demokritov, B. Hillebrands, Yu.S. Kivshar, V. Grimalsky,
Yu. Rapoport, M.P. Kostylev, B.A. Kalinikos, A.N. Slavin
J. Appl. Phys. **87**, 5088 (2000).

13. *Quantized spin wave modes in micron size magnetic discs*
J. Jorzick, S.O. Demokritov, B. Hillebrands, B. Bartenlian, C. Chappert, D. Decanini,
F. Rousseaux, E. Cambril
J. Appl. Phys. **87**, 5082 (2000).

14. *Oscillatory exchange bias effect in FeNi/Cu/FeMn and FeNi/Cr/FeMn trilayer systems*
T. Mewes, B.F.P. Roos, S.O. Demokritov, B. Hillebrands
J. Appl. Phys. **87**, 5064 (2000).

15. *Magnetisierungsdynamik in magnetischen Strukturen*
B. Hillebrands
Beitrag zur Ferienschule "Femtosekunden und Nano-eV: Dynamik kondensierter Materie", IFF, Forschungszentrum Jülich (2000).

16. *Suppression of exchange bias by ion irradiation*
T. Mewes, R. Lopusnik, J. Fassbender, B. Hillebrands, M. Jung, D. Engel, A. Ehresmann,
H. Schmoranzer
Appl. Phys. Lett. **76**, 1057 (2000).

17. *Switching behavior of a Stoner particle beyond the relaxation time limit*
M. Bauer, J. Fassbender, B. Hillebrands, R.L. Stamps
Phys. Rev. B **61**, 3410 (2000).

18. *Structure and magnetic properties of exchange-biased polycrystalline Fe/MnPd bilayers*
Y.J. Tang, B.F.P. Roos, T. Mewes, A.R. Frank, M. Rickart, M. Bauer,
S.O. Demokritov, B. Hillebrands, X. Zhou, B.Q. Liang, X. Chen, and W.S. Zhan
Phys. Rev. B **62**, 8654 (2000).

19. *Preparation of barriers in magnetic tunel junctions using atomic source oxidation*
W. Maass, B. Roos, S.O. Demokritov, B. Hillebrands, M. Weiler
Chip **3**, 51 (2000) (Semiconductior Industry Sourcebook, Unaxis).

20. *Exchange bias effect and anisotropy analysis of FM/AF bilayers*
Y.J. Tang, B.F.P. Roos, T. Mewes, M. Bauer, S.O. Demokritov, B. Hillebrands,
W.S. Zhan
Mat. Sci. & Eng B **76**, 59 (2000).

7.2 In press

1. *Time domain MOKE detection of spin wave modes and precession control of magnetization*
   M. Bauer, R. Lopusnik, H. Dötsch, B. A. Kalinikos, C. E. Patton, J. Fassbender, B. Hillebrands
   J. Magn. Magn. Mat. in press.
2. *Modification of the exchange bias effect by He ion irradiation*
   A. Mougin, T. Mewes, R. Lopusnik, M. Jung, D. Engel, A. Ehresmann, H. Schmoranzer, J. Fassbender, B. Hillebrands
   IEEE Trans. Magn., in press.
3. *Successful suppression of magnetization precession after short field pulses*
   M. Bauer, R. Lopusnik, J. Fassbender, B. Hillebrands, H. Dötsch
   IEEE Trans. Magn. in press.
4. *Brillouin light scattering from surface phonons in hexagonal and cubic boron nitride films*
   T. Wittkowski, P. Cortina, J. Jorzick, K. Jung, B. Hillebrands
   Diam. Rel. Mat., in press.
5. *Brillouin light scattering studies of confined spin waves: linear and nonlinear confinement*
   S.O. Demokritov, B. Hillebrands, A.N. Slavin
   Phys. Rep., in press.

7.3 Submitted

1. *Magnetic nanopattering of FeNi/FeMn exchange bias bilayers by ion irradiation*
   A. Mougin, S. Poppe, J. Fassbender, B. Hillebrands, G. Faini, U. Ebels, M. Jung, D. Engel, A. Ehresmann, H. Schmoranzer
   submitted to J. Appl. Phys.
2. *Dipolar interaction in arrays of micron-size rectangular magnetic elements*
   J. Jorzick, C. Krämer, S.O. Demokritov, B. Hillebrands, E. Sondergard, M. Bailleul, C. Fermon, U. Memmert, A. N. Müller, U. Hartmann, E.Y. Tsymbal
   submitted to Phys. Rev. B.
3. *Spin dynamics in magnetic films patterned into dots and wires*
   J. Jorzick, S.O. Demokritov, B. Hillebrands, B. Bartenlian, C. Chappert, F. Rousseaux, A.N. Slavin
   Submitted to Proceedings of the 2nd Int. Symp. on Frontiers in Magnetism.
4. *Preparation of magnetic tunnel junctions by ionized atom beams*
   B.F.P. Roos, S.O. Demokritov, B. Hillebrands
   Submitted to J. Apl. Phys.

5. *Local manipulation and reversal of the exchange bias field by ion irradion in FeNi/FeMn double layers*
   A. Mougin, T. Mewes, M. Jung, D. Engel, A. Ehresmann, H. Schmoranzer,
   J. Fassbender, B. Hillebrands
   Submitted to Phys. Rev. Lett.
6. *Comparative study of the epitaxial growth of Cu on MgO(001) and on hydrogen terminated Si(001)*
   T. Mewes, M. Rickart, A. Mougin, S.O. Demokritov, J. Fassbender, B. Hillebands,
   M. Scheib
   submitted to Surf. Sci.

Chapter 8: Conferences, Workshops, Schools and Seminars

(shown in chronological order with the speaker named)

8.1 Conferences

8.1.1 Invited talks

S.O. Demokritov
Nichtlineare Spinwellenpropagation in magnetischen Schichten
DPG Frühjahrstagung, Regensburg, Germany, 27.-31.03.2000 (Hauptvortrag)

S.O. Demokritov
Spindynamics in laterally confined magnetic structures
International Symposium "Physical Properties of Structural Thin Metallic Films", Berlin, Germany, 12.-14.04.2000

B. Hillebrands
Magnetisierungsdynamik und Konzepte für schnelles magnetisches Schalten
Statusseminar "Magnetoelektronik" des Bundesministeriums für Bildung und Forschung, Dresden, Germany, 14.–16.06.2000

B. Hillebrands
Spin wave solitons and bullets studied by space and time resolved Brillouin light scattering spectrosocopy
International Conference on Magnetism, Recife, Brazil, 06.-11.08.2000

B. Hillebrands
Time and space resolved Brillouin light scattering measurements on the propagation and diffraction of nonlinear magnetostatic spin waves in Yttrium iron garnet films
8th International Conference on Ferrites, Kyoto, Japan, 8.-21.09.2000

8.1.2 Contributed talks and posters

6 contributions: 44th Annual Conference on Magnetism and Magnetic Materials, San Jose, USA, 09.–25.11.1999

1 contribution: WE-Heraeus-Seminar, Bad Honnef, 05.–07.01.2000

1 contribution: Gordon Conference, Ventura, U.S.A.,13.–18.02.2000

3 contributions: Intermag 2000, Toronto, Kanada, 09.–1304.2000

12 contributions: DPG-Frühjahrstagung Regensburg, Germany, 27.–31.03.2000

2 contributions: Symposium on Spin Electronics, Halle, Germany, 03.–06.07.00

2 contributions: 16th International Colloquium on Magnetic Films and Surfaces, Natal, Brazil, 13.–18.08. 2000

8.2 Workshops

8.2.1 Invited lectures

B. Hillebrands
Charakterisierung der elastischen Eigenschaften von harten und superharten Schichten mit der Brillouin-Lichtstreutechnik
D-A-CH 2000 Abschlusstreffen, Neuhofen/Ybbs, Österreich, 05.–09.03.2000

B. Hillebrands
Fast switching behaviour of magnetic dots
EU-COST-P3 WG4-Meeting Heraklion, Crete, Greece, 04.–06.05.2000

S.O. Demokritov
Static and dynamic properties of lateral magnetic structures
ESF Nanomag Workshop on Magnetic properties of artificial and solf-organized nanostructures, Uppsala, Sweden, 14.-16.09.2000

M. Rickart
Magnetic anisotropies of epitaxial Fe films on vicinal Ag(001) and Au(001) with different miscut orientations
ESF Nanomag Workshop on Magnetic properties of artificial and solf-organized nanostructures, Uppsala, Schweden, 14.–16.09.2000

B. Hillebrands
Die Brillouin-Lichtstreuspektroskopie als vielseitiges Untersuchungsinstrument zum Studium magnetischer und elastischer Eigenschaften
DEGA Workshop, Bad Honnef, 04.–06.10.2000

J. Fassbender
Local manipulation and reversal of the exchange bias field by ion irradiation in FeNi/FeMn double layers
Exchange bias in heterolayer systems, Workshop of the SFB 491, Duisburg, 27.10.2000

8.2.2 Contributed talks and posters

R. Lopusnik
Investigation of magnetization dynamics with sub-ns time resolution
Magnetic Workshop at the Institute of Electrical Engineering, Slovak Academy of Sciences, Bratislava, Slovakia, 26.-27.06.2000

R. Lopusnik
Time domain MOKE detection of spin wave modes and precession control for magnetization switching in ferrite films
ESF Nanomag Workshop on Magnetic properties of artificial and solf-organized nanostructures, Uppsala, Schweden, 14.–16.09.2000

J. Jorzick
Spin waves in arrays of interacting permalloy dots
ESF Nanomag Workshop on Magnetic properties of artificial and solf-organized nanostructures, Uppsala, Schweden, 14.–16.09.2000

J. Jorzick
Brillouin-Lichtstreuung an magnetischen Drähten und Inseln
DEGA Workshop, Bad Honnef, 04.–06.10.2000

T. Wittkowski
Elastische Eigenschaften von Hartstoffschichten
DEGA Workshop, Bad Honnef , 04.–06.10.2000

T. Wittkowski
Elastic properties of thick c-BN films
c-BN Expertentreffen, Saarbrücken, 04.–06.10.2000

8.3 Schools

8.3.1 Invited lectures

B. Hillebrands
Magnetisierungsdynamik in magnetischen Strukturen
Ferienschule "Femtosekunden und Nano-eV: Dynamik kondensierter Materie",
IFF, Forschungszentrum Jülich, Germany, 21.03.2000

S.O. Demokritov
Brillouin light scattering from spin waves in nanostructured materials
TMR Euroconference School "From nanoscopic to mesoscopic magnetic systems", Spetses, Greece, 27.8.-1.9. 2000

8.3.2 Contributed talks and posters

A. Mougin
Manipulation and reversal of the exchange bias effect by ion irradiation (talk)
TMR Euroconference School "From nanoscopic to mesoscopic magnetic systems", Spetes, Greece, 27.8.-1.9. 2000

8.4 Invited colloquia and seminars

B. Hillebrands
Spin dynamics in confined magnetic structures
Seminar, National Institute of Standards and Technology, Boulder, U.S.A., 12.11.1999

B. Hillebrands
Spin dynamics in confined magnetic structures
Colloquium, IBM Almaden Research Center, San Jose, U.S.A., 19.11.1999

B. Hillebrands
Spin dynamics in confined magnetic structures
Colloquium, Center for Magnetic Recording Research, University of California San Diego, U.S.A., 23.11.1999

J. Jorzick
Magnetic properties of micron-size magnetic wires and rectangular dots
Seminar, CEA, Saclay, France, 22.11.1999

J. Jorzick
Spin waves in restricted geometries
Seminar, University of Perugia, Italy, 06.–11.12.1999

T. Wittkowski
Brillouin-Lichtstreuung zur Bestimmung der elastischen Eigenschaften von Hartstoffschichten
Materialwissenschaftliches Kolloquium, Univ. Kaiserslautern, 27.01.2000

B. Hillebrands
Spindynamik in magnetischen Schichten
Physikalisches Kolloquium, Universität Bielefeld, 11.02.2000

B. Hillebrands
Spin dynamics in patterned magnetic films
Kolloquium of the Department of Physics, Katholieke Universiteit Nijmegen, Netherlands, 21.03.2000

A. Mougin
Tayloring the exchange bias effect by ion irradiation
Seminar, Université de Nancy, France, 03.04.2000

A. Mougin
RFe2(110): growth, morphology and magnetic properties
Seminar, Université de Strasbourg, France, 04.04.2000

A. Mougin
Tayloring the exchange bias effect by ion irradiation
Seminar, Université Paris-Sud, Orsay, France, 06.04.2000

A. Mougin
RFe2(110): growth, morphology and magnetic properties
Seminar, Laboratoire de Minéralogie, Paris VI-VV, Paris, France, 07.04.2000

B. Hillebrands
Spin dynamics in patterned magnetic films
Colloquium of the Department of Physics, University of Edmonton, Canada, 07.04.2000

M. Bauer
Precession control for magnetization switching in ferrite films
Seminar, National Institute of Standards and Technology, Boulder, U.S.A., 18.04.2000

M. Bauer
Precession control for magnetization switching in ferrite films
Seminar, IBM Almaden Research Center, San Jose, U.S.A., 20.04.2000

S.O. Demokritov
Spin waves in magnetic dots and wires
Seminar Department of Materials, University of Oxford, U.K., 26.04.2000

B. Hillebrands
Spindynamik in magnetischen Strukturen
Physikalisches Kolloquium der Friedrich-Schiller-Universität Jena, 15.05.2000

S.O. Demokritov
Spinwellenquantisierung in lateralen magnetischen Schichten
Physikalisches Seminar Universität Regensburg, 28.07.2000

J. Jorzick
Spinwellen in lateral begrenzten magnetischen Systemem
Seminar, group of Prof. P. Grünberg, FZ Jülich, 08.–09.09.2000

B. Hillebrands
Spin dynamics and fast magnetic switching in confined magnetic structures
Colloquium, Toyota Technical Institute, Japan, 22.09.2000

B. Hillebrands
Ultrafast magnetic switching
Colloquium of the Department of Physics, Charles University Prague, Czech Republic, 10.10.2000

B. Hillebrands
Schnelle Magnetisierungsdynamik in kleinen magnetischen Inseln
Festkörperphysik-Colloquium und Kolloquium des SFB 290, Freie Universität Berlin, 20.10.2000

S.O. Demokritov
Static and dynamic magnetic properties of laterally patterned magnetic structures
Colloquium, Université Paris-Sud, Laboratoire de Physique des Solides, 30.10.2000

S.O. Demokritov
Static and dynamic magnetic properties of laterally patterned magnetic structures
Seminar, group of Prof. P. Moch, Université Paris-Nord, 31.10.2000

8.5 Contributions to other meetings

T. Wittkowski
1) *Elastische Eigenschaften von hexagonalen und kubischen Bornitridschichten*
2) *Brillouin-Lichtstreuung an Oberflächenphononen: Untersuchung amorpher Kolenstoffschichten*
D-A-CH 2000 Abschlusstreffen, Neuhofen/Ybbs, Österreich, 05.–09.03.2000

A. Mougin
Modifications of the exchange bias effect induced by ion irradiation
DYNASPIN Midterm Review, Halle, Germany, 03.02.2000

A. Mougin
Manipulation and reversal of the exchange bias effect by ion irradiation
DYNASPIN meeting, York, United Kingdom, 17.07.2000

Chapter 9: Awards

H. Busch and U. Grabowy:
Sonderpreis der Ernst-Kalkhof-Stiftung im Wettbewerb "Pioniergeist 2000"

T. Mewes:
Preis der Kreissparkassenstiftung

H. Nembach:
Artur-Fischer-Preis 2000 der Dr. Artur-Fischer-Stiftung zur Förderung von qualifizierten wissenschaftlichen Leistungen